

NIST Technical Note 2084

Collapse Risk of Steel Special Moment Frames per FEMA P695

Matthew S. Speicher
Jazalyn Dukes
Kevin K.F. Wong

This publication is available free of charge from:
<https://doi.org/10.6028/NIST.TN.2084>

NIST
**National Institute of
Standards and Technology**
U.S. Department of Commerce

NIST Technical Note 2084

Collapse Risk of Steel Special Moment Frames per FEMA P695

Matthew S. Speicher
Jazalyn Dukes
Kevin K.F. Wong
*Earthquake Engineering Group
Materials and Structural Systems Division
Engineering Laboratory*

This publication is available free of charge from:
<https://doi.org/10.6028/NIST.TN.2084>

February 2020



U.S. Department of Commerce
Wilbur L. Ross, Jr., Secretary

National Institute of Standards and Technology
Walter Copan, NIST Director and Undersecretary of Commerce for Standards and Technology

Certain commercial entities, equipment, or materials may be identified in this document in order to describe an experimental procedure or concept adequately. Such identification is not intended to imply recommendation or endorsement by the National Institute of Standards and Technology, nor is it intended to imply that the entities, materials, or equipment are necessarily the best available for the purpose.

NIST policy is to use the International System of Units (metric units) in all its publications. In this report, however, information is presented in U.S. Customary Units (inch-pound), because those are the units used in the standards being evaluated and is the preferred system of units in the U.S. earthquake engineering industry.

**National Institute of Standards and Technology Technical Note 2084
Natl. Inst. Stand. Technol. Tech. Note 2084, 97 pages (February 2020)
CODEN: NTNOEF**

**This publication is available free of charge from:
<https://doi.org/10.6028/NIST.TN.2084>**

Abstract

The American Society of Civil Engineers (ASCE) performance-based seismic design standard, ASCE 41, contains methodologies used by practicing engineers to assess existing buildings and to design new buildings. In 2015, the National Institute of Standards and Technology completed a study of the relationship between the methodologies used in ASCE 41 and those used in traditional prescriptive design standards; e.g., ASCE 7 and American Institute of Steel Construction (AISC) specification 341. The study showed inconsistencies between the two approaches, with some potentially unwarranted conservatism in ASCE 41. To further investigate the relationship between performance-based and prescriptive methodologies, this report presents the results of a collapse assessment of six steel special moment frames. The goal is to verify that the buildings have a no greater than 10 % probability of collapse given a risk-targeted maximum considered earthquake, which is the design intent of ASCE 7. The influence of modeling assumptions, such as using default ASCE 41 backbone curves versus experimentally-derived backbone curves, is discussed. Furthermore, the impacts of other choices in the analyses such as damping, composite slab action, and P-delta column modeling are explored. The results are used to scrutinize the performance indicated by the ASCE 41 assessment. In general, the performance indicated by the ASCE 41 assessment is shown to be conservative relative to the collapse performance indicated by using the methodologies within the Federal Emergency Management Agency (FEMA) publication P695. Based on the findings in this report, the authors recommend that the approach used in ASCE 41 assessments be reviewed to reduce overly-conservative results.

Key words

earthquake engineering, performance-based design, seismic assessment, building codes

Table of Contents

1. Introduction	1
2. Background and Motivation.....	1
3. Methodology.....	3
3.1. Building Designs	3
3.2. Nonlinear Models	7
3.3. Incremental Dynamic Analysis Methodology.....	9
3.4. FEMA P695 Assessment Calculations.....	10
4. Results.....	11
4.1. Incremental Dynamic Analysis	11
4.2. FEMA P695 Assessment.....	13
5. Discussion	14
6. Select Sensitivity Studies.....	16
6.1. Simplified Models	18
6.2. Varied Predictive Equations.....	20
6.3. Predictive Equations vs Experimentally Calibrated.....	21
6.4. Composite-Slab Action	22
6.5. Damping	24
6.6. P-Delta Column.....	24
6.7. Discussion of Sensitivity Results	26
7. Conclusions.....	28
References.....	30
Appendix A Three-Dimensional Analysis vs. Two-Dimensional Analysis.....	33
A.1 Modeling of the 4-story ELF Frame in 2D	33
A.2 Modeling of the Leaning Column	34
Appendix B Comparison of Perform-3D vs OpenSees Models.....	46
B.1 Differences in Modeling Assumptions.....	46
B.2 Subassembly Behavior	47
B.3 Comparison of Responses Using the 8-story RSA Frame	49
Appendix C Nonlinear Hinge Modeling.....	56
C.1 General Modeling Approach.....	56
C.2 Model Validation.....	59
Appendix D Implementation of Ibarra-Medina-Krawinkler Model.....	67
D.1 Implementation of IMK Model into General Software Packages.....	68

D.2 Implementation of IMK Model into OpenSees Using the Bilin Uniaxial Material . 70
D.3 Stiffness Calculation for Members with Reduced Beam Sections..... 74
Appendix E Supplemental Calculations for FEMA P695 77
Appendix F Ground Motion Suite Characteristics 84

List of Tables

Table 1. Summary of predicted component performance by the nonlinear procedures for the collapse (CP) structural performance level (SPL) at the basic safety earthquake (BSE)-2 earthquake hazard level (EHL) for each archetype building (adapted from [13]).....	2
Table 2. Total building weight and vibration period information for the OpenSees models..	9
Table 3. Summary of collapse performance evaluation for the suite of baseline SMFs.....	14
Table 4. Summary of performance predicted using the nonlinear procedures in ASCE 41 for the SMF building suite (the performance is for collapse prevention under basic safety earthquake-2 hazard level) [3].	16
Table 5. Parameters investigated in the sensitivity study.	18
Table 6. Predictive vs. calibrated parameters used for variation v3.	22
Table 7. Summary of results for the sensitivity study in terms of collapse margin ratio.....	28
Table 8. Summary of results for the sensitivity study normalized by the baseline results. ..	28
Table 9. Mass calculations for the 2D model of the 4-story ELF moment frame.....	34
Table 10. Properties of the gravity columns in the 3D model.....	35
Table 11. Properties of the leaning column in the 2D model.....	35
Table 12. Periods of vibration for the 2D and 3D models.	35
Table 13. Nonlinear RBS hinge properties for bay 2 of the 8-story RSA-designed frame: strength and rotation.	60
Table 14. Nonlinear RBS properties for bay 2 of the 8-story RSA-designed frame: stiffness.	60
Table 15. Nonlinear column properties for lower hinge of each story in pier 2 of the 8-story RSA-designed frame: strength and rotation.....	62
Table 16. Nonlinear column properties for lower hinge of each story in pier 2 of the 8-story RSA-designed frame: stiffness.	63
Table 17. Nonlinear panel zone properties for each story in pier 2 of the 8-story RSA-designed frame.	65
Table 18. Pushover analysis response quantities.	81
Table 19. Mode shape and Mass at each floor of 4-ELF design.....	82
Table 20. Spectral shape factor, <i>SSF</i> , for archetypes designed using SDC D_{max} (abbreviated from Table 7-1b of FEMA P695).	83
Table 21. FEMA P695 far field ground motion set.....	84
Table 22. Scale factors to anchor median spectral value to MCE spectrum at $C_u T_a$	85

List of Figures

Figure 1. General building layout showing the location of the special moment frame (SMF) and special concentrically braced frame (SCBF).....	4
Figure 2. Typical building floor plan showing the structural framing layout.....	5
Figure 3. The six SMF designs investigated in this report.....	6
Figure 4. OpenSees modeling details for the special moment frames.....	7
Figure 5. Illustration of the parameters used to define hinge backbone curves.....	8
Figure 6. Incremental dynamic analysis curves for the (a) 4-story ELF, (b) 4-story RSA, (c) 8-story ELF, (d) 8-story RSA, (e) 16-story ELF, and (f) 16-story RSA-designed frames.....	12
Figure 7. Fitted fragility curves for the (a) 4-story ELF, (b) 4-story RSA, (c) 8-story ELF, (d) 8-story RSA, (e) 16-story ELF, and (f) 16-story RSA-designed frames.....	13
Figure 8. Backbone curve properties used for baseline hinge models.....	17
Figure 9. Illustration of RBS and column hinge behavior for variation v1.....	18
Figure 10. Panel zone modeling approaches for variation v1: (a) using the <i>Steel01</i> material model and (b) using the <i>Hysteretic</i> material.....	19
Figure 11. Comparison of fragility curves for the (a) 4-story ELF, (b) 4-story RSA, (c) 8-story ELF, and (d) 8-story RSA-designed frames using elastic plastic hinges (variation v1).....	20
Figure 12. Example illustration of RBS hinge behavior for variation v2.....	20
Figure 13. Comparison of fragility curves for the (a) 4-story ELF, (b) 4-story RSA, (c) 8-story ELF, and (d) 8-story RSA-designed frames using + / - COV from the predictive equations (variation v2).....	21
Figure 14. Example illustration of experimentally-calibrated model.....	22
Figure 15. Comparison of fragility curves for an alternative 4-story RSA-designed building using the predictive equations and calibrated to specific experimental data (variation v3).....	22
Figure 16. Example illustration of RBS hinge behavior for variation v4 – considering composite slab action.....	23
Figure 17. Comparison of fragility curves for the (a) 8-story ELF and (b) 8-story RSA-designed frames accounting for composite slab action (variation v4).....	23
Figure 18. Comparison of fragility curves for the (a) 8-story ELF and (d) 8-story RSA-designed frames accounting varying modal damping levels (variation v5).....	24
Figure 19. Leaning column modeling approaches for variation v6: (a) baseline model using a continuous member, (b) v6a using pinned connections, and (c) v6b using plastic hinges.....	25
Figure 20. Comparison of fragility curves for the (a) 4-story ELF, (b) 4-story RSA, (c) 8-story ELF, (d) 8-story RSA, (e) 16-story ELF, and (f) 16-story RSA-designed frames using different modeling approaches for the leaning column (variation v6).....	26
Figure 21. 2D model of the 4-story ELF moment frame.....	33
Figure 22. Leaning column of the 2D model.....	34
The end result of the applied gravity loads is shown in Figure 23.....	35
Figure 24. Gravity loads applied on the 2D model (where k = kip).....	36
Figure 25. Responses due to 1994 Northridge EQ at Mulholland Drive station, comp 009.....	37
Figure 26. Responses due to 1999 Kocaeli, Turkey EQ at Duzce station, comp 180.....	37
Figure 27. Responses due to 1999 Kocaeli, Turkey EQ at Duzce station, comp 270.....	38

Figure 28.	Responses due to 1995 Kobe, Japan EQ at Shin-Osaka station, comp 000.	38
Figure 29.	Responses due to 1992 Landers EQ at Yermo fire station, comp 360.	39
Figure 30.	Responses due to 1994 Northridge EQ at Canyon Country station, comp 000... ..	39
Figure 31.	Responses due to 1995 Kobe, Japan EQ at Nishi-Akashi station, comp 090.....	40
Figure 32.	Responses due to 1971 San Fernando EQ at Hollywood station, comp 090.....	40
Figure 33.	Responses due to 1990 Manjil, Iran EQ at Abbar station, longitudinal comp. ...	41
Figure 34.	Responses due to 1999 Hector Mine EQ at Hector station, comp 000.	41
Figure 35.	Responses due to 1987 Superstition Hills EQ at Poe Road station, comp 270. ..	42
Figure 36.	Responses due to 1979 Imperial Valley EQ at El Centro #11, comp 230.....	42
Figure 37.	Responses due to 1987 Superstition Hills EQ at El Centro station, comp 000. ..	43
Figure 38.	Responses due to 1979 Imperial Valley EQ at Delta station, comp 352.....	43
Figure 39.	Responses due to 1999 Duzce, Turkey EQ at Bolu station, comp 000.	44
Figure 40.	Responses due to 1989 Loma Prieta EQ at Gilroy Array #3, comp 090.....	44
Figure 41.	Responses due to 1989 Loma Prieta EQ at Capitola station, comp 090.	45
Figure 42.	Subassembly models used to compare (a) Perform-3D and (b) OpenSees.	47
Figure 43.	Drift contributions for a moment frame subassembly.....	48
Figure 44.	Comparison of the response of subassembly to cyclic loading for OpenSees and Perform-3D (model used in [3]).	48
Figure 45.	Explanation of drift between (a) some point, k, at the capping moment and (b) some point, k+1, just beyond the capping moment.	48
Figure 46.	Comparison of floor displacement responses due to 1995 Kobe earthquake at Nishi-Akashi station, component 090, magnified by a scale factor of 1.3.	50
Figure 47.	Comparison of floor displacement responses due to 1995 Kobe earthquake at Nishi-Akashi station, component 090, magnified by a scale factor of 1.4.	51
Figure 48.	Comparison of floor displacement responses due to 1995 Kobe earthquake at Nishi-Akashi station, component 090, magnified by a scale factor of 1.5.	52
Figure 49.	Comparison of floor displacement responses due to 1994 Northridge earthquake at Mulholland Drive station, component 009, magnified by a scale factor of 1.5.....	53
Figure 50.	Comparison of floor displacement responses due to 1994 Northridge earthquake at Mulholland Drive station, component 009, magnified by a scale factor of 1.6.....	54
Figure 51.	Comparison of floor displacement responses due to 1994 Northridge earthquake at Mulholland Drive station, component 009, magnified by a scale factor of 2.4.....	55
Figure 52.	Generic member backbone curve with basic input parameters.	57
Figure 53.	(a) Analytical model for the beam-to-column connection elements (panel zone, beam hinge, and column hinge) and (b) generic panel zone force-deformation backbone curve.....	59
Figure 54.	RBS hinge backbone curves and select analysis results for the left hinge in bay 2 of the 8-story RSA-designed building (EQ 1, sf = 2.0).	61
Figure 55.	Column hinge backbone curves and select analysis results for lower hinge at each story in pier 2 of the 8-story RSA-designed building (EQ 1, sf = 2.0).....	64
Figure 56.	Panel zone hinge backbone curves and select analysis results for hinge at each story in pier 2 of the 8-story RSA-designed building (EQ 1, sf = 2.0).....	66
Figure 57.	(a) Member subjected to symmetric loading and (b) The corresponding moment vs. rotation relationship at the hinge.	67
Figure 58.	Separation of (a) total rotation into (b) elastic rotation of the member and (c) plastic rotation of the hinge.....	68

Figure 59. Separation of (a) total rotation into (b) elastic rotation of the member and (c) rotation of the plastic hinge for implementation using BILIN in OpenSees. 71

Figure 60. (a) Reduced beam section and (b) approximate computer model. 74

Figure 61. Computation of the initial stiffness for (a) beam with RBS and (b) the corresponding moment diagram and (c) the corresponding m/EI diagram..... 76

Figure 62. Nonlinear static pushover curves for the 4-story (a) ELF and (b) RSA designs. 77

Figure 63. Nonlinear static pushover curves for the 8-story (a) ELF and (b) RSA designs. 78

Figure 64. Nonlinear static pushover curves for the 16-story (a) ELF and (b) RSA designs. 78

Figure 65. Typical nonlinear pushover curve. 79

Figure 66. Nonlinear Pushover curve for 4-story ELF design..... 80

Figure 67. Mode shape of 4-ELF-designed frame. 82

Figure 68. Unscaled ground motion response spectra. 86

Figure 69. Normalized ground motion response spectra. 86

Glossary

(A)CMR – (adjusted) collapse margin ratio

AISC – American Institute of Steel Construction

ASCE – American Society of Civil Engineers

CDF – cumulative distribution function

COV – coefficient of variation

ELF – equivalent lateral force

EPP – elastic perfectly plastic

FEMA – Federal Emergency Management Agency

IDA – incremental dynamic analysis

IMK – Ibarra Medina Krawinkler

MCE_R – (risk-targeted) maximum considered earthquake

NIST – National Institute of Standards and Technology

PBSE – performance-based seismic engineering

RBS – reduced beam section

RSA – response spectra analysis

SCBF – special concentrically braced frame

SEI – Structural Engineering Institute

SMF – special moment frame

SRSS – square-root-of-the-sum-of-the-squares

1. Introduction

Performance-based seismic design gives the structural engineer freedom to develop earthquake-resistant building design solutions that are more efficient and cost-effective than those obtained using the prescriptive building code requirements found in American Society of Civil Engineers (ASCE) / Structural Engineering Institute (SEI) 7 [1]. ASCE/SEI 41 [2] contains performance-based methodologies used by some practicing engineers for both the assessment of existing buildings and the design of new buildings. In 2015, the National Institute of Standards and Technology (NIST) completed a study [3-5] investigating the relationship between ASCE/SEI 41-06 [6] and traditional prescriptive design standards (e.g., ASCE/SEI 7-10 [7] and American Institute of Steel Construction (AISC) 341 [8]) for a variety of framing systems, including steel special moment frames. In general, the study showed inconsistencies between the two approaches, with some unwarranted conservatism thought to be present in ASCE/SEI 41. It was recognized that, to more fully contextualize the results and to see if the intended performance objective of ASCE/SEI 7 is being met, the collapse likelihood of each building subjected to strong earthquake ground motions needs to be determined.

This report presents the results of the collapse assessment of six steel special moment frames investigated in the previous NIST study [3-5]. First, the background and motivation of this work is outlined. Next, the methodology is discussed in terms of model selection and collapse fragility determination. The buildings are modeled in OpenSees [9] using commonly accepted approaches established in the literature. Federal Emergency Management Agency (FEMA) P695 [10] is used as a guide to determine the probability of collapse in a “standardized” manner via the collapse margin ratio. The sensitivity of the results to various modeling approaches and assumptions is explored. The margin against collapse also considers additional sources of uncertainty per FEMA P695. Generally, the results indicate that the ASCE/SEI 7-designed special moment frames meet the intent of the code. This helps contextualize the observations made in Harris and Speicher [3], which show that, in many cases, a building designed with ASCE/SEI 7 does not pass an ASCE/SEI 41 assessment. This supports the conclusion that ASCE/SEI 41 may produce results that are overly-conservative compared to results achieved using ASCE/SEI 7. Reasons for the conservatism are scrutinized and recommendations for change are made.

2. Background and Motivation

In 2009, a NIST report titled “Research Required to Support Full Implementation of Performance-Based Seismic Design” [11] identified the need for more research and refinement of the performance-based seismic engineering (PBSE) methodologies in U.S. model building codes. In 2012, another NIST report titled “Tentative Framework for Development of Advanced Seismic Design Criteria for New Buildings” [12] identified the need for advanced seismic design criteria so that a structural system designed using ASCE/SEI 7 would more accurately meet the intended collapse objective under the design level earthquake. To address these needs, a multi-year project was undertaken to assess the correlation between ASCE/SEI 7 (hereafter ASCE 7) and its PBSE counterpart, ASCE/SEI 41 (hereafter ASCE 41). ASCE 41 was initially created for use in existing building assessment. Therefore, there was some uncertainty as to how an ASCE 41-designed building would perform relative to an ASCE 7-designed building. If both ASCE 7 and ASCE 41 are

consistent, then a building designed using ASCE 7 should pass a building assessed with ASCE 41.

To compare ASCE 7 and ASCE 41, a suite of steel buildings was first designed with the International Building Code (IBC)-referenced standards (i.e., ASCE 7, AISC 341, and AISC 360). For each frame type investigated, the following six designs were created: 4, 8 and 16-stories using both the equivalent lateral force (ELF) and the response spectrum analysis (RSA) design procedures. The designs were then assessed with the four different assessment procedures in ASCE 41 – namely: linear static, linear dynamic, nonlinear static, and nonlinear dynamic. In 2015, the results were documented in a series of reports by Harris and Speicher [3-5] and corresponding journal papers [13-16] in the years after.

Since nonlinear analysis can be considered the most sophisticated assessment approach, the nonlinear analysis results are of particular interest. The nonlinear analysis results are summarized in Table 1 for the set of steel special moment frames. Note, the ASCE 41 assessment is component-based and the components investigated are shown in the table.

Table 1. Summary of predicted component performance by the nonlinear procedures for the collapse (CP) structural performance level (SPL) at the basic safety earthquake (BSE)-2 earthquake hazard level (EHL) for each archetype building (adapted from [13]).

Building Height	Design Procedure	Nonlinear Static			Design Procedure	Nonlinear Dynamic (mean)		
		BC	CM	PZ		BC	CM	PZ
4-story	ELF	Pass	Pass	Pass	ELF	Pass	Pass	Pass
	RSA	Fail	Pass	Pass	RSA	Fail	Pass	Pass
8-story	ELF	Pass	Fail	Pass	ELF	Fail	Fail	Pass
	RSA	Pass	Fail	Pass	RSA	Fail	Fail	Fail
16-story	ELF	Pass	Pass	Pass	ELF	Pass	Pass	Pass
	RSA	Pass	Pass	Pass	RSA	Fail	Fail	Pass

Note: BC = beam-to-column connection, CM = column member, PZ = panel zone

Deficiencies in the design (as identified by ASCE 41) of the NIST building suite (i.e., [3]) include the columns at the base of the frame and beam-column connections. Four out of the six buildings presented in Table 1 do not pass the ASCE 41 nonlinear assessment given the assumptions made in Harris and Speicher [3], which included modeling the nonlinear hinges with the default backbone curves from ASCE 41. Default backbone curves were used because it was presumed an engineer would rely on these during the iterative design process for a new building. The results have led to additional studies critiquing the approach used in Harris and Speicher [3], including the criteria used for ground motions selection and scaling, and the criteria used for modeling behavior and judging acceptance [14-18]. Overall the initial study and the additional studies have suggested that ASCE 41 is conservative in terms of assessment criteria and there should be an effort to reduce the conservatism to more realistically reflect actual performance and thus reduce the cost of a retrofit when a deficient system is evident.

Given this context, the observations highlighted above rely on the assumption that the building designs used by Harris and Speicher [3] meet the intent of ASCE 7, which is a 10 %

or less probability of collapse, given a maximum considered earthquake. Harris and Speicher [3] recommended conducting a collapse assessment for each building to determine whether they meet the intended performance objectives of ASCE 7 (i.e., verify that ASCE 7 is providing appropriate designs or suggest the issues reside with ASCE 41). This recommendation was also made by the peer review team that oversaw Harris and Speicher [3]. Determining the collapse likelihood of the buildings will help contextualize the results of Harris and Speicher [3] and give direction for improvement in ASCE 7 and/or ASCE 41.

Furthermore, vetting the collapse performance of the building in Harris and Speicher [3] will complement other projects, such as Applied Technology Council (ATC) 114 [19], that have recommended improvements to the modeling guidance in ASCE 41. One such recommendation is to use predictive linear regression equations based on the current testing archives to more rigorously calibrate nonlinear hinge modeling behavior. An ongoing project funded by FEMA (ATC 140) is working alongside the ASCE 41 standard committee to try and implement some of these recommendations into the current building code update cycle.

3. Methodology

Six steel special moment framed buildings are assessed in this study using FEMA P695. This section gives details on the methodology implemented to determine each buildings collapse likelihood.

3.1. Building Designs

As already mentioned, the building designs come from a suite of archetypes steel buildings designed by Harris and Speicher [3]. The building framing schematics, including the special moment frame (SMF) and special concentrically braced frame (SCBF), are shown in Figure 1. The typical framing floor plan and the SMF member sizes are shown in Figure 2 and Figure 3, respectively. The buildings have SMFs in the east-west direction and SCBFs in the north-south direction. Both the SMFs and the SCBFs are located at the perimeter of the building. The material used in design are A992 Grade 50 steel for the wide-flange sections and A500 Grade B steel for the hollow structural sections. Further material and design details can be found in Harris and Speicher [3].

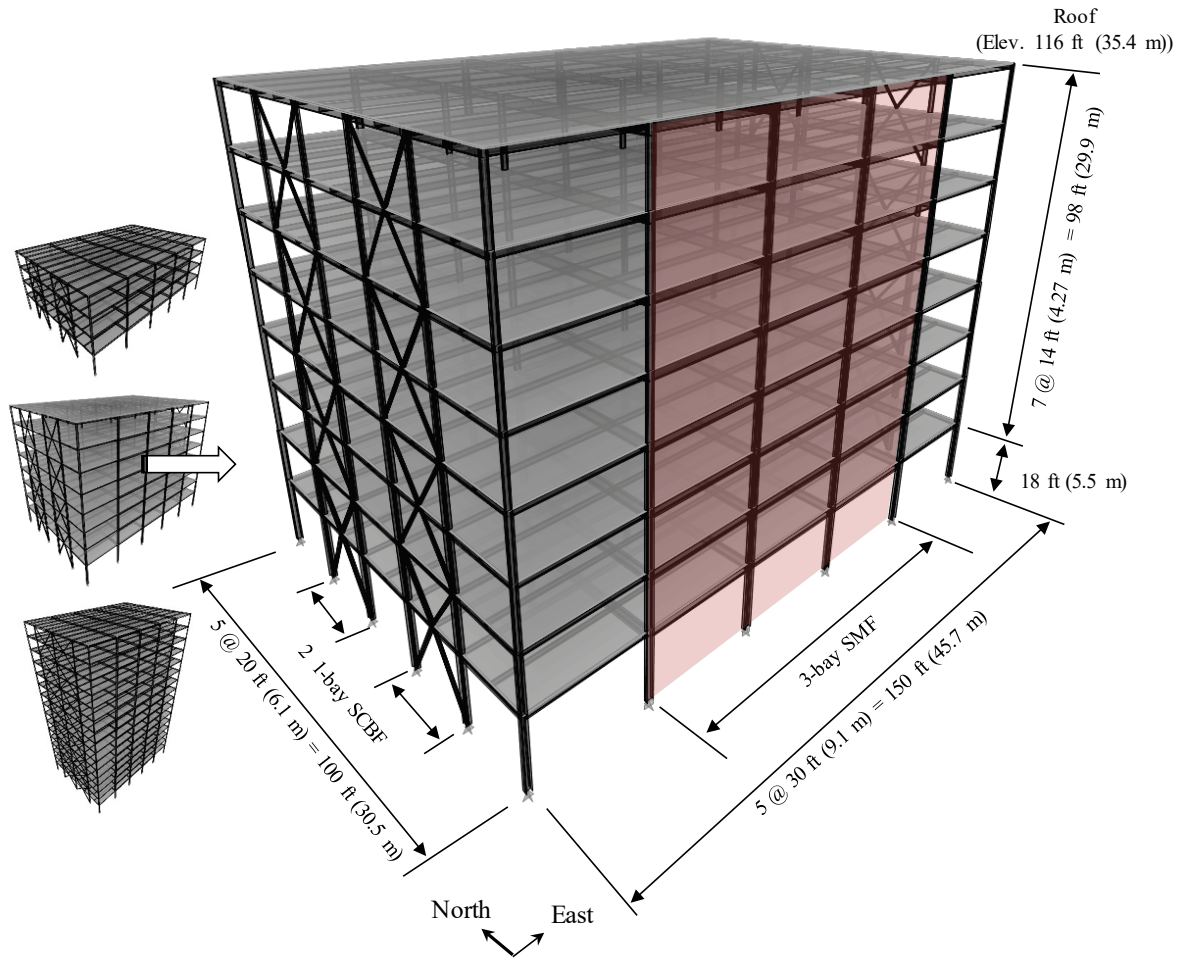


Figure 1. General building layout showing the location of the special moment frame (SMF) and special concentrically braced frame (SCBF).

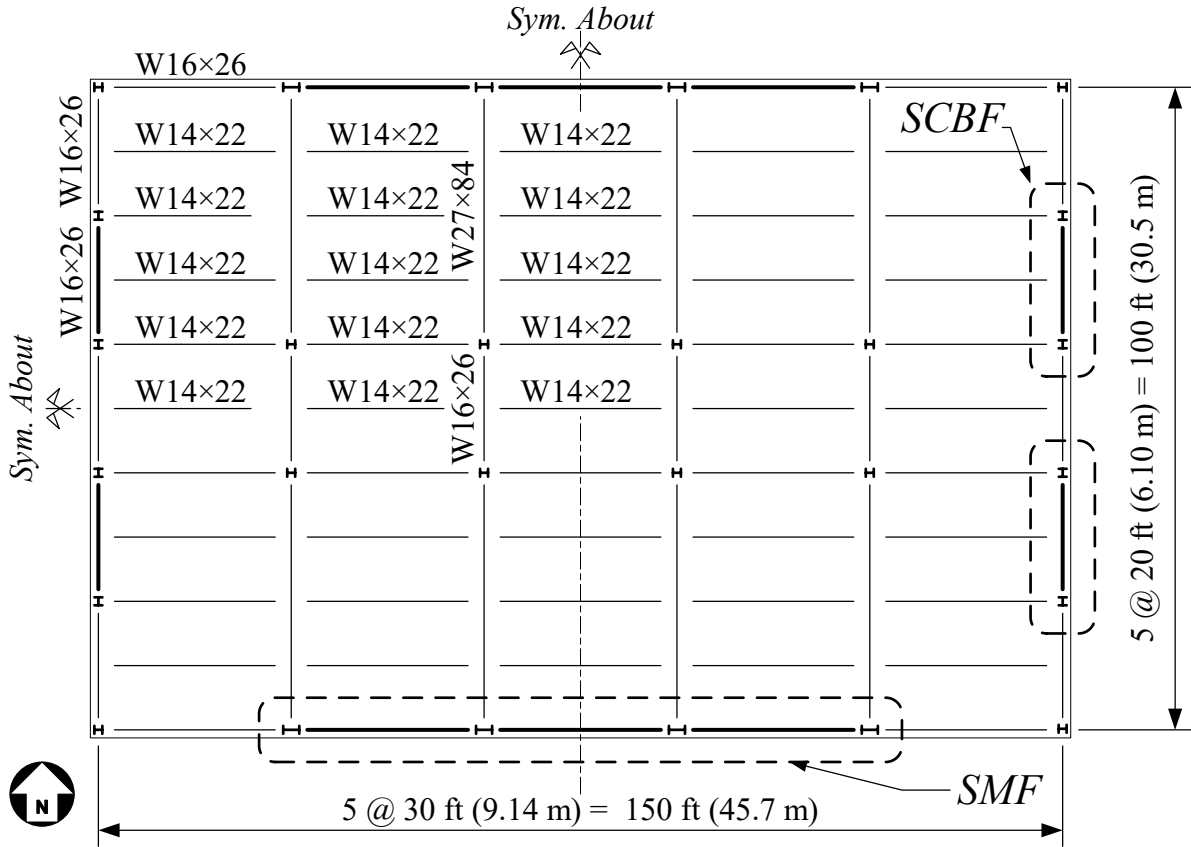


Figure 2. Typical building floor plan showing the structural framing layout.



Figure 3. The six SMF designs investigated in this report.

3.2. Nonlinear Models

A schematic of the modeling approach is shown in Figure 4. Harris and Speicher [3] conducted the ASCE 41 performance assessment using three-dimensional (3D) models in Perform-3D [20]. Because of the large computational cost of running incremental dynamic analysis, two-dimensional (2D) models were created in the Open System for Earthquake Engineering Simulation (OpenSees) [9]. To verify the models are reasonably similar, a performance comparison was conducted as shown in Appendix A. It was found that the 2D and 3D models matched well, which is not surprising given the buildings are symmetric and the buildings have non-intersecting lateral force-resisting systems (see Appendix A for more details).

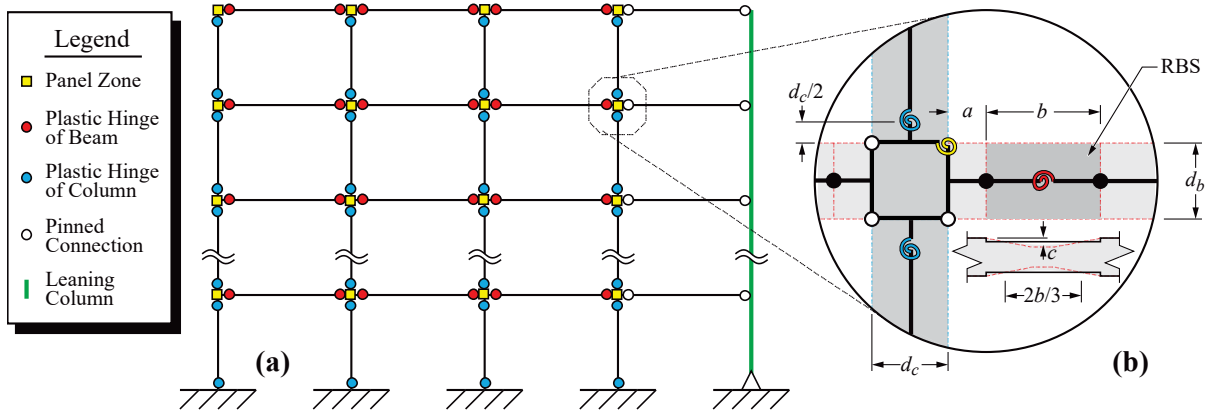


Figure 4. OpenSees modeling details for the special moment frames.

A “baseline” model was created for each frame design. The baseline model has 3 % modal damping for all modes and 0.3 % stiffness proportional damping to damp out spurious higher modes. The damping approach aligns with that used in the Perform-3D models used by Harris and Speicher [3]. The baseline model is considered the default modeling approach in this report and is used to compare with other modeling assumptions such as varied damping and modified nonlinear component backbone curves.

The moment frames have reduced beam section (RBS) connections. The RBS connection stiffness was modeled using a prismatic cross-section over the length of the RBS (length b). The width of the RBS was assumed to be equivalent to the actual RBS width at $b/3$ away from the center of the RBS. The nonlinear behavior was captured by a nonlinear rotational spring placed at the RBS center. The nonlinear spring was assigned a stiffness of 10 times that of the unreduced beam. Since this spring is in series with the elastic beam elements, the elastic beam stiffness was increased to give an overall beam (including the RBS and nonlinear spring) stiffness equal to that without the nonlinear spring (see [21] and Appendix D.1 for further discussion).

OpenSees was used in lieu of Perform-3D to streamline the analysis and postprocessing workflow and enable the use of enhanced degradation models. Appendix B presents a comparison of the models used in Perform-3D and OpenSees. In the OpenSees model,

collapse is shown to occur at higher intensity measures compared to the same frame in the Perform-3D model. The cause of these differences is shown, at least in part, to be from the differences in the nonlinear hinge models. These observations should be kept in mind when comparing the study by Harris and Speicher [3] to the results of a FEMA P695 assessment. Given the inherent uncertainties in nonlinear response history analysis, the general agreement of the responses is, none-the-less, considered reasonable.

A key advantage in OpenSees is that it can capture cyclic and in-cycle degradation using the modified Ibarra Medina Krawinkler (IMK) model with the Bilin material model. The force-deformation parameters for the RBS followed the recommendations made by Lignos and Krawinkler [22], which were derived using multivariate regression analysis of a database of experimental results. These parameters include the plastic rotation capacity, θ_p , the post-capping rotation capacity, θ_{pc} , the yield strength, M_y , the capping strength, M_c , the ultimate rotation, θ_u , the residual strength ratio, κ , and the reference cumulative plastic rotation parameter, Λ . The parameters are shown graphically in Figure 5. A detailed discussion on the OpenSees modeling approach is given in Appendix C and Appendix D.

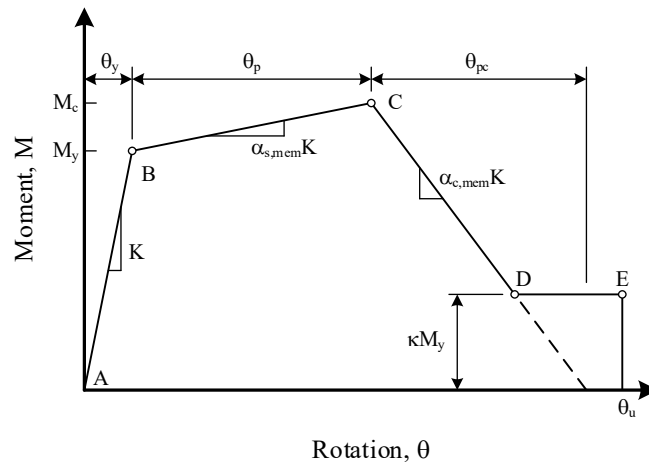


Figure 5. Illustration of the parameters used to define hinge backbone curves.

For the columns, nonlinear springs were added at $d / 2$ away from the face of the beam (see Figure 1Figure 4), where d is the depth of the column. These nonlinear springs followed the same approach (10 times the stiffness) as that discussed for the beams. The force-deformation parameters for the column hinges followed the recommendations produced by NIST [19] using the monotonic backbone (since degradation is captured). The panel zones were modeled explicitly using the approach outlined by Krawinkler [23]. A set of “rigid” elements with pinned connections was placed at the panel zone region with one corner being tied together with a nonlinear rotational spring. The spring parameters were based on fundamental mechanics. Additionally, though the column splice was designed at 4 ft (1.2 m) above the beam-to-column joint, this was ignored in the model.

A single P-delta column was used to capture the large P- Δ and small P- δ effects arising from forces acting on the deformed geometry. The P-delta column was given a moment of inertia equal to the sum of the moment of inertias of the tributary gravity frame columns and the special concentrically braced frame columns. The P-delta column was constrained to the SMF by equal degree of freedom constraints at each floor level. The P-delta column was assumed elastic along the height of the building; no nonlinear moment hinges were added. The implications of this choice are explored later in this report.

As a summary of select dynamic properties of each building, Table 2 provides the weight and vibration periods for the OpenSees models.

Table 2. Total building weight and vibration period information for the OpenSees models.

Building	Weight (kips)	Approximate fundamental period, $C_u T_a$	1 st Order periods		2 nd Order periods	
			T_1	T_2	T_1	T_2
			(s)			
04-ELF	5172	1.04	1.71	0.51	1.76	0.52
04-RSA	5136		2.06	0.58	2.15	0.59
08-ELF	10618	1.76	2.59	0.92	2.69	0.94
08-RSA	10527		3.38	1.19	3.59	1.24
16-ELF	21782	3.02	3.74	1.38	3.89	1.42
16-RSA	21649		4.26	1.60	4.48	1.66

3.3. Incremental Dynamic Analysis Methodology

To estimate each building's collapse fragility, incremental dynamic analysis (IDA) was conducted. IDA involves subjecting a structural model to multiple ground motion records that are scaled over a range of levels to produce a response curve [24]. IDA is the basis of the FEMA P695 process. The suite of ground motions used for the IDA is referred to as the "far-field" set in FEMA P695. This set consists of 22 record pairs from sites that were more than 10 km from the fault rupture. Given the 2D model, each ground motion was applied independently, resulting in 44 earthquake runs at each intensity level increment. The ground motions were first normalized per FEMA P695 using the FEMA 695 Toolkit [25], and then the suite was further scaled (i.e., anchored) such that the median of the suite equals the risk-targeted maximum considered earthquake (MCE_R) at the fundamental period of the building (i.e., in this case, taken as $C_u T_a$ – defined in ASCE 7).

The ground motion intensity measure (IM) used is the median spectral acceleration, S_T , of the suite of ground motions at the fundamental period ($C_u T_a$) of the building. Collapse was defined as reaching 7.5 % interstory drift in any story, which is explained in the next section, or when the analysis failed to converge. The IM s at which the structure collapses for each ground motion is first aggregated across the ground motion suite. The fragility function was then calculated using the method of moments ("Method A" as described by Porter et al [26]), where the formulation is based on scaling all the ground motions until all specimens have

collapsed. Equation 1 shows the calculation of the fragility function, where $P(C | IM = x)$ is the probability of collapse of the structure at intensity measure x :

$$P(C | IM = x) = \Phi\left(\frac{\ln(x/\theta)}{\beta}\right) \quad (1)$$

The normal cumulative distribution function (CDF) is denoted by Φ , the median of the fragility function is denoted by θ , and the standard deviation of $\ln(IM)$ is denoted by β . Equations 2 and 3 show the formulation of the fragility function estimators (designated with the “hat” marking) calculated from n number of earthquakes, which are method of moments estimators of a normal distribution [27].

$$\ln \hat{\theta} = \frac{1}{n} \sum_{i=1}^n \ln(IM_i) \quad (2)$$

$$\hat{\beta} = \sqrt{\frac{1}{n-1} \sum_{i=1}^n \left(\ln(IM_i/\hat{\theta})\right)^2} \quad (3)$$

The analyses were performed using the parallel version of OpenSees, OpenSeesMP [9], on the Extreme Science and Engineering Discovery Environment (XSEDE) platform [28] and on local NIST computers.

3.4. FEMA P695 Assessment Calculations

After the IDA was completed, the fragility curve results were converted into collapse margin ratios, CMR s. The intensity measure S_T is defined as the median spectral acceleration of the record set at period T . The CMR is calculated as follows:

$$CMR = \frac{\hat{S}_{CT}}{S_{MT}} \quad (4)$$

where \hat{S}_{CT} is the median collapse intensity (i.e., the value of S_T that results in 50 % of the ground motions causing collapse) and S_{MT} is the value of the MCE_R spectrum at period T .

Once the CMR is known, an adjusted collapse margin ratio, $ACMR$, is calculated to factor in the effects of spectral shape (i.e., frequency content of the ground motion record set). The $ACMR$ is calculated as follows:

$$ACMR = SSF \times CMR \quad (5)$$

where the spectral shape factor, SSF , is a function of the fundamental period of the building, the period-based ductility factor, μ_T , and the Seismic Design Category. The period-based ductility factor is calculated using pushover results and is used as a surrogate for the period elongation that happens when building components yield.

Finally, the $ACMR$ is compared to the acceptable values, given the desired collapse probability target and total system uncertainty. The total system uncertainty values are

largely based on judgement as outlined in FEMA P695. For a suite of new archetype building designs, the generally accepted collapse probability target is 10 % or less, given a MCE_R . It is recognized that for an individual building design, probability of collapse, given a MCE_R , may reach as high as 20 %, which is still considered acceptable. Therefore, since a limited suite of archetypes are investigated in this report, the targets of $ACMR_{10\%}$ and $ACMR_{20\%}$ are both presented.

4. Results

4.1. Incremental Dynamic Analysis

The results are first presented in the form of IDA curves and associated fragility curves. Figure 6 shows the IDA curves for the suite of buildings. The IDA curves illustrate, for each ground motion, the global progression of damage as intensities are increased. After approximately 7.5 % interstory drift, a small increase in intensity generally results in a large increase in interstory drift. Also, after approximately 7.5 % interstory drift the frequency of solution algorithm convergence issues increased. Therefore, the choice of collapse being defined as 7.5 % interstory drift was deemed both appropriate and convenient.

Figure 7 shows the fragility curves for the suite of buildings. From these curves, the probability of collapse at the MCE_R can be estimated, though the effect of spectral shape and additional sources of uncertainty have not yet been accounted for. For reference, the MCE_R spectral accelerations at C_uT_a , S_{MT} , for the 4-, 8-, and 16-story buildings are 0.87 g, 0.51 g, and 0.30 g, respectively.

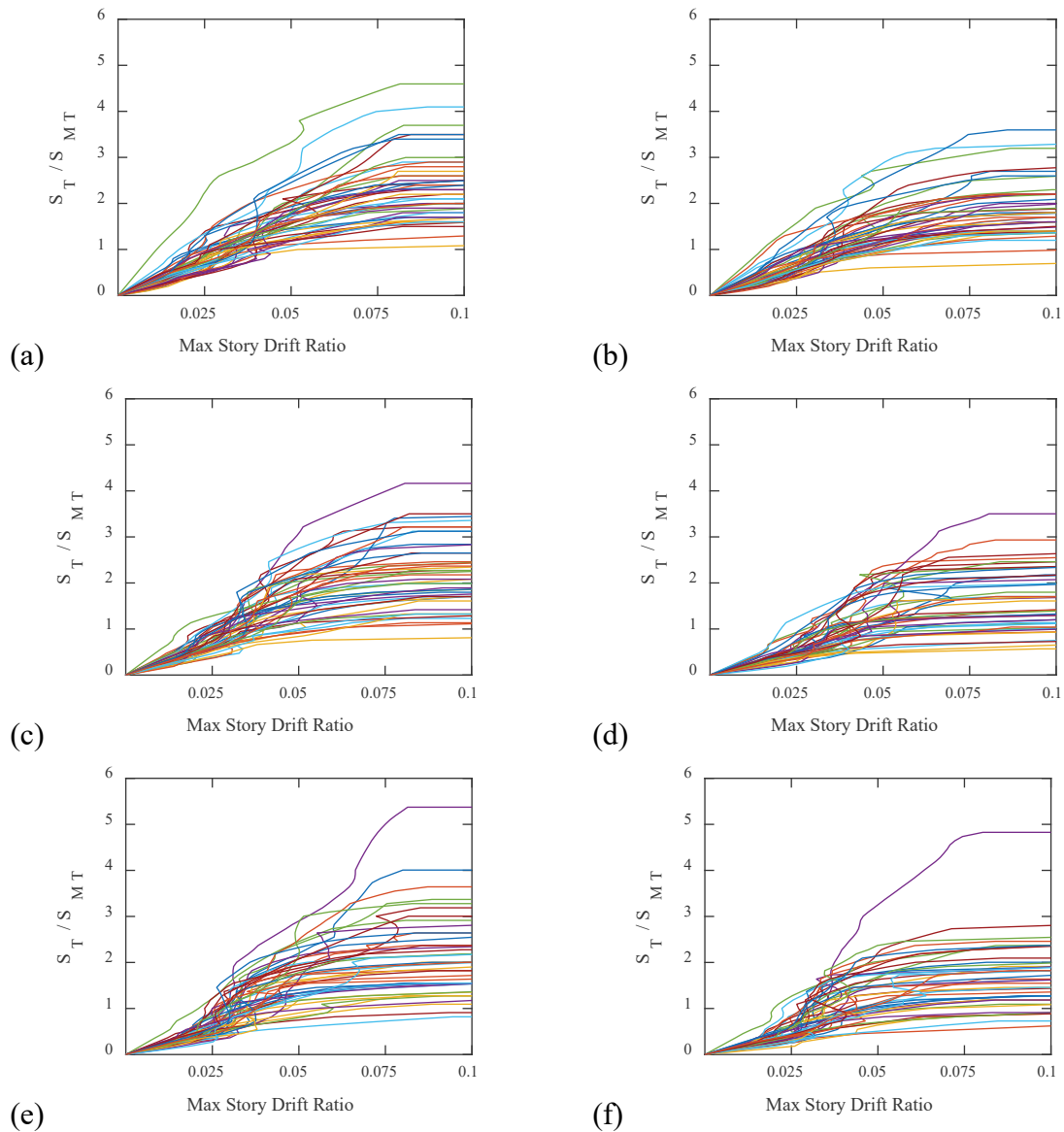


Figure 6. Incremental dynamic analysis curves for the (a) 4-story ELF, (b) 4-story RSA, (c) 8-story ELF, (d) 8-story RSA, (e) 16-story ELF, and (f) 16-story RSA-designed frames.

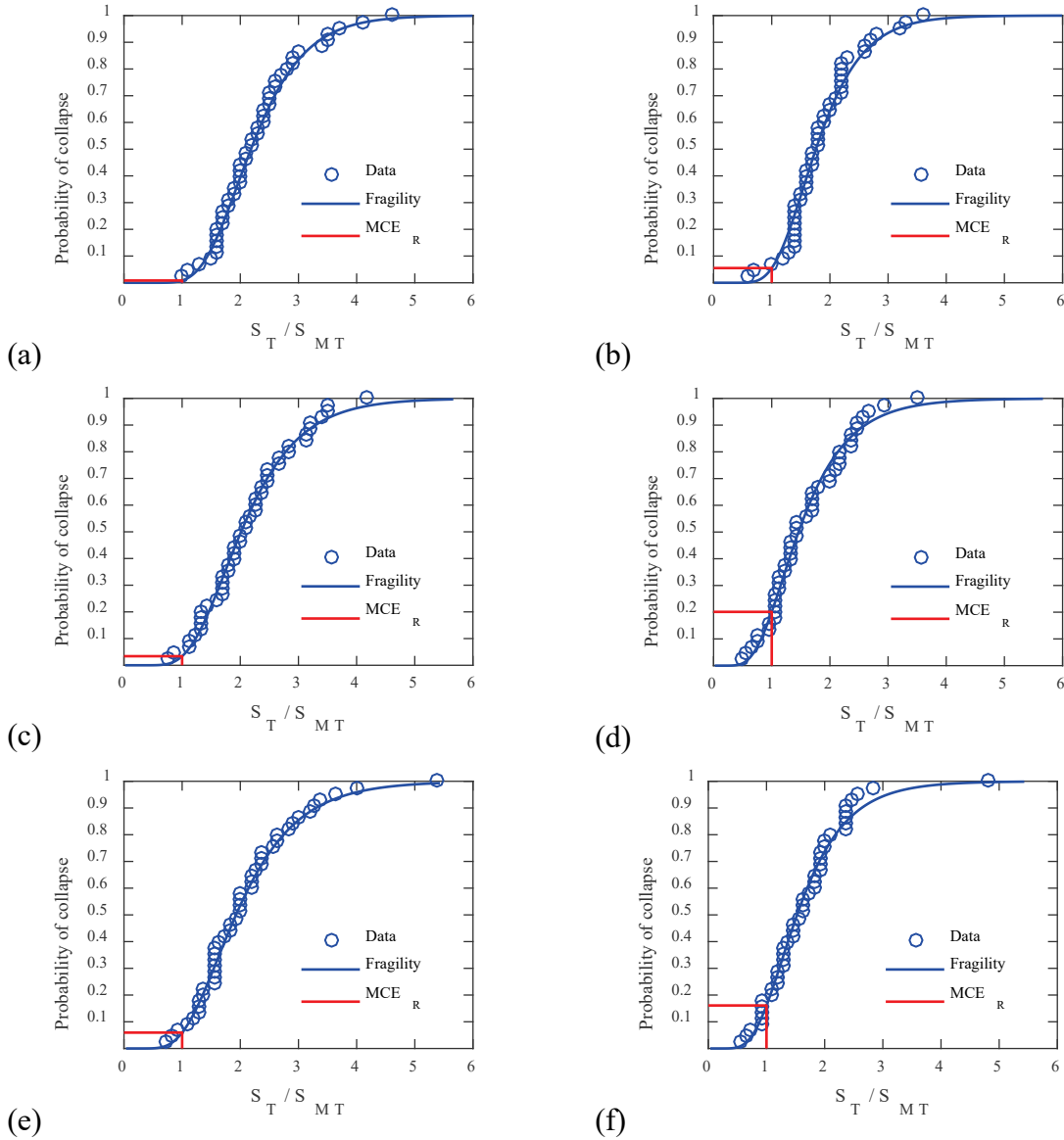


Figure 7. Fitted fragility curves for the (a) 4-story ELF, (b) 4-story RSA, (c) 8-story ELF, (d) 8-story RSA, (e) 16-story ELF, and (f) 16-story RSA-designed frames.

4.2. FEMA P695 Assessment

With the fragility curves determined, the final steps in the FEMA P695 collapse assessment can be completed. Table 3 shows the results of the collapse assessment after accounting for spectral shape and additional sources of uncertainty as outlined in FEMA P695. The collapse margin ratio, *CMR*, is calculated from the *IM* that results in 50 % of the ground motions causing collapse and the *IM* at the MCE_R , S_{MT} . The calculations for the spectral shape factor, *SSF*, are given in Appendix E. The *SSF* is used to increase the *CMR* to get the adjusted collapse margin ratio, *ACMR*. The *SSF* ranges from approximately 1.3 to 1.5

In regard to uncertainty, the total system collapse uncertainty, β_{TOT} , is calculated using the square-root-of-the-sum-of-the-squares (i.e., SRSS) of the (1) the record-to-record uncertainty, β_{RTR} , (2) the design requirements-related collapse uncertainty, β_{DR} , (3) the test data-related uncertainty, β_{TD} , and (4) the modeling-related uncertainty, β_{MDL} . For β_{RTR} , a fixed value of 0.40 is assumed because FEMA P695 states that this is appropriate for the performance evaluation of systems with significant period elongation. For β_{DR} , it is assumed there is high confidence in the basis of the design requirements and medium in terms in completeness and robustness; therefore, the result is a "good" rating, and a value of 0.2 is assigned. For β_{TD} , it is assumed there is high confidence the test results but a medium level of completeness and robustness of test results. This also gives a "good" rating, and a value of 0.2 is assigned. Lastly, for β_{MDL} , it is assumed that the accuracy and robustness of the models is high, but the representation of collapse characteristics is medium. This again gives a "good" rating, and a value of 0.2 is assigned. Now combining all the uncertainties using the SRSS, the total collapse uncertainty is found to be 0.53. Using this total uncertainty enables the determination of an acceptable value of adjusted collapse margin ratio from FEMA P695 Table 7-3, which is 1.96 for 10 % probability of collapse and 1.56 for 20 % probability of collapse.

In summary, Table 3 shows the assessment parameters and the associated acceptance check for the FEMA P695 assessment. This table includes the static overstrength factor, Ω , and the period-based ductility factor, μ_T , both of which are necessary in determining the *ACMR*. As noted, all frames pass this assessment. These results are further explored in the next sections.

Table 3. Summary of collapse performance evaluation for the suite of baseline SMFs.

Building	Assessment parameters					Acceptance check (Pass/Fail = P/F)					
	Static Ω	CMR	μ_T	SSF	ACMR	ACMR _{10%}	P/F ratio	P/F	ACMR _{20%}	P/F ratio	P/F
04-ELF	2.78	2.18	5.4	1.48	3.22	1.96	1.64	Pass	1.56	2.06	Pass
04-RSA	2.22	1.76	4.5	1.43	2.51	1.96	1.28	Pass	1.56	1.61	Pass
08-ELF	2.61	2.01	4.1	1.40	2.83	1.96	1.44	Pass	1.56	1.81	Pass
08-RSA	1.85	1.46	3.1	1.35	1.97	1.96	1.01	Pass	1.56	1.27	Pass
16-ELF	1.92	1.93	3.6	1.38	2.65	1.96	1.35	Pass	1.56	1.70	Pass
16-RSA	1.68	1.53	3.7	1.38	2.11	1.96	1.08	Pass	1.56	1.35	Pass

5. Discussion

To evaluate the implications of the collapse results, it is useful to recall the findings in Harris and Speicher [3] as summarized in Table 4. For both the nonlinear static and dynamic procedures, an RBS connection fails the assessment in only one out of six frames. In contrast, for the nonlinear dynamic procedure, the assessment indicates worse performance and an RBS connection fails the criteria in four out of six frames. Additionally, the column and panel zones show failures. The discussion presented here is focused on the RBS connection because the newest version of ASCE 41 (i.e., ASCE 41-17) has updated modeling assessment criteria that address some of the problems seen in the column components.

Recall that the design intent in ASCE 7 is that a building will have a probability of collapse, given an MCE_R , of less than or equal to 10 %. However, as discussed previously, the FEMA

P695 methodology is intended to be for a suite of archetype buildings. If each of these buildings are taken as individuals, FEMA P695 suggests that a code-complying building may be acceptable if the probability of collapse, given an MCE_R , reaches as high as 20 %. Additionally, the primary purpose of the FEMA P695 methodology is to provide a way to quantify the seismic performance factors of a new (or existing) lateral force resisting system (i.e., the response modification coefficient, R , the overstrength factor, Ω , and the deflection amplification factor, C_d). Using the methodology to assess the collapse potential is dependent on any limitations that may be unforeseen when using it for something other than its original purpose.

The IDA and the resulting fragility curves shown in Figure 6 and Figure 7 suggest that all buildings are adequate in terms of collapse probability except for the 8-story RSA frame, which has a collapse probability of approximately 19 % at the MCE_R . Note, this number *does not* factor in the influence of ground motion spectral shape nor the additional sources of uncertainty addressed in FEMA P695 – these calculation results are discussed next. Though this frame does not meet the 10 % goal of a code-designed building as determined by the methodology described herein, it does fall below the 20 % limit mentioned above.

Now, if the ground motion spectral shape is considered, each frame's reserve against collapse is increased based on the level of period-based ductility calculated from a nonlinear pushover analysis. If the additional sources of uncertainty are also included as outlined in FEMA P695, the standard deviation, β , of the lognormally-distributed CDF (i.e., the fragility curve) is increased to account for this additional uncertainty – the higher the uncertainty the higher the required reserve against collapse. As shown in Table 3, all six frames have $ACMR$ values greater than the required values for 10 % probability of collapse ($ACMR_{10\%}$). In other words, all buildings have a probability of collapse less than or equal 10 %, given an MCE_R . The RSA-designed frames generally have less margin of collapse than the ELF-designed frames.

With these findings in mind, it appears ASCE 41 is overly-conservative at identifying performance issues in this set of frames. This is, of course, subject to the assumptions and limitations of the analysis done herein. One issue that needs further investigation is the conservative nature of the Perform-3D model which used some default modeling parameters from ASCE 41. This model has a backbone curve with a steep descending branch beyond the capping point, which results in a sharp drop in stiffness for a subassembly. As is shown in Appendix B.2, the nonlinear response can be sensitive to this slope. ASCE 41 does not give clear guidance on the post-capping slope, and in this case the approach used in [3] may be conservative and result in unfavorable performance, especially for the nonlinear dynamic procedure (as opposed to the nonlinear static procedure). Other reasons for potential conservatism in ASCE 41 are explored in the previously mentioned companion study looking at other steel framing systems [14-16]. Identified reasons include (1) the method used for selecting and scaling ground motions and (2) ASCE 41 modeling parameters derived from fully-reversed cyclic loading protocols, which may not be a true representation of component behavior at MCE_R or greater level earthquakes [18]. Regardless, the results presented in this report provides further context to the results seen in Harris and Speicher [3].

Table 4. Summary of performance predicted using the nonlinear procedures in ASCE 41 for the SMF building suite (the performance is for collapse prevention under basic safety earthquake-2 hazard level) [3].

Building	Nonlinear Static Procedure			Nonlinear Dynamic Procedure		
	RBS connection	Column	Panel Zone	RBS connection	Column	Panel Zone
04-ELF	Pass	Pass	Pass	Pass	Pass	Pass
04-RSA	Fail	Pass	Pass	Fail	Pass	Pass
08-ELF	Pass	Fail	Pass	Fail	Fail	Pass
08-RSA	Pass	Fail	Pass	Fail	Fail	Fail
16-ELF	Pass	Pass	Pass	Pass	Pass	Pass
16-RSA	Pass	Pass	Pass	Fail	Fail	Pass

In contrast to the Perform-3D model, the OpenSees model uses a more complicated, and potentially less conservative, approach. The difference in backbone curves can be seen in the subassembly discussion presented in the Appendix B. In the OpenSees model, both in-cycle and cyclic degradation are accounted for. Therefore, a monotonic backbone curve is used. This results in more energy being dissipated in the hysteresis and a more gradual strength loss beyond the capping point (point of maximum strength). Further investigation into the sensitivity of the modeling parameters and analysis approaches may be beneficial to fully vet these results, some of which are explored in the next section.

6. Select Sensitivity Studies

To understand the impact of some of the modeling assumptions made in this study, the effect of varying several parameters is investigated as summarized in Table 5. A baseline model is established using a general nonlinear hinge backbone curve as shown in Figure 8. A backbone curve can be derived from specific experimental results that are relevant to the action being modeled, by using predictive equations derived from a database of such experimental results, or by other methods. The backbone curve for the baseline model is derived using the predictive equations.

First, the impact of the nonlinear backbone curve properties is explored in variations 1 through 4. The baseline model uses the predictive equations reported in Lignos and Krawinkler [22] for the RBS connection hinges and the predictive equations reported in NIST [19] for the column hinges and panel zone hinges. Lignos and Krawinkler [22] developed a database of steel wide flange beams to aid in validating and calibrating their deterioration modeling parameters of steel components. The data from the database is also used to associate the deterioration parameters to geometric and material properties of the model. The empirical equations of the deterioration parameters that Lignos and Krawinkler [22] developed for RBS connections are shown in Appendix C.

For variation 1, the nonlinear hinge models are replaced with a “simple” elastic-perfectly plastic (EPP) model. This EPP model does not capture strain hardening nor deterioration. This variation can be considered a comparison against “simple” inelastic component behavior. For variation 2a and 2b, the rotation parameters from the predictive equations are reduced and increased by the coefficient of variation (COV), respectively. A COV of 0.30 was used as reported by Lignos and Krawinkler [22] and NIST [19]. For variation 3, the

parameters for the modified IMK model are determined from an individual experimental test that closely matched one of the frame designs. Since a bigger section property was used for the beams, this variation was compared not against the baseline model but with a model with the same section size but with parameters using the predictive equations. For variation 4, the effect of the composite slab is considered by using recommended predictive equations given in NIST [19].

Additionally, the sensitivity of the analysis results to the level of viscous damping is considered in variation 5 and the effect of P-delta column modeling assumptions is considered in variation 6.

The following subsections discuss the variations in more detail and the resulting effects on the performance outcome.

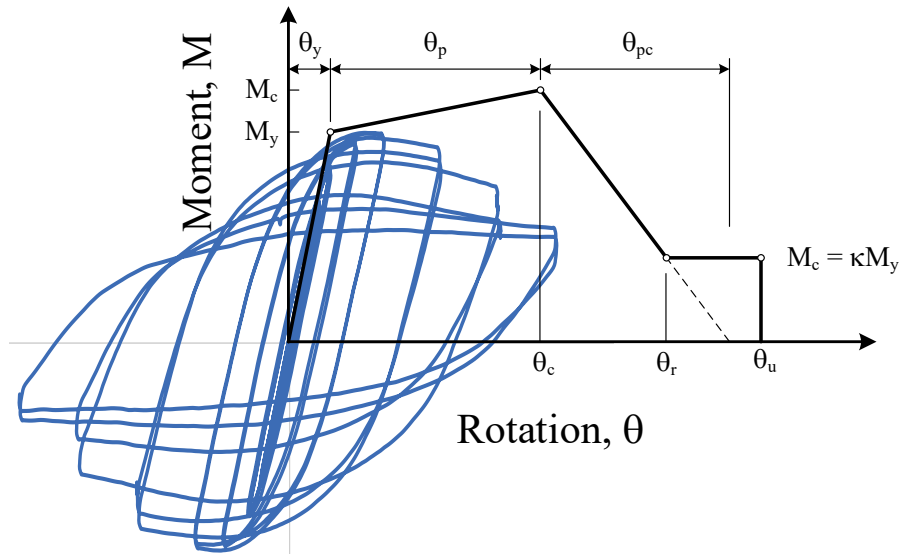


Figure 8. Backbone curve properties used for baseline hinge models.

Table 5. Parameters investigated in the sensitivity study.

Parameter / Assumption	Baseline	Variation			
RBS nonlinear hinge behavior	predictive equations	(v1) elastic perfectly plastic	(v2) +/- COV of predictive equations	(v3) calibrated to an individual experiment	(v4) considering composite-slab action
Panel zone hinge behavior	<i>Hysteretic</i> material with $\alpha \neq 0$ see Appendix C	(v1a) <i>Steel01</i> material	(v1b) <i>Hysteretic</i> material with $\alpha \approx 0$		
Modal damping	3 %	(v5)			
		a	b	c	
		2 %	1 %	0.01 %	
P-Delta column treatment	ΣEI , continuous with no hinges	(v6)			
		a	b		
		columns pinned at ends (zero rotational stiffness and strength)	columns given EP hinges at ends (sum the M_p s of non-SMF columns)		

6.1. Simplified Models

The first variation, v1, is done using a simplified EPP hinge behavior as illustrated in Figure 9. Each RBS hinge and column hinge are defined with the same yield moment, M_y , as the baseline model. For the panel zone, two sub-variations are considered: (v1a) using the *Steel01* material model in OpenSees and (v1b) using the *Hysteretic* material model in OpenSees as illustrated in Figure 10. Unlike the *baseline* model, the hardening value, α , for variation v1b is set equal to 10^{-8} (i.e., approximately zero).

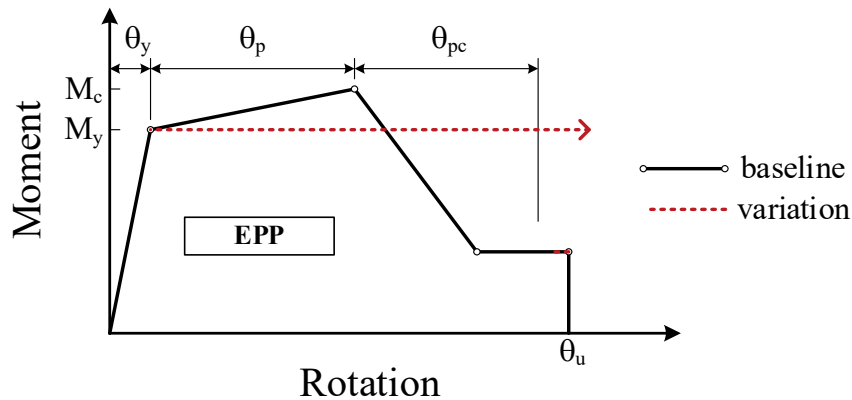


Figure 9. Illustration of RBS and column hinge behavior for variation v1.

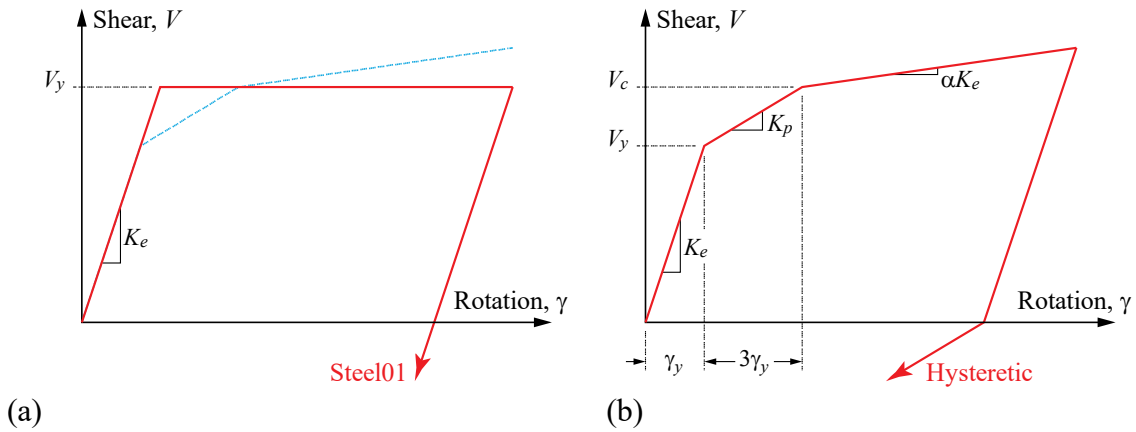


Figure 10. Panel zone modeling approaches for variation v1: (a) using the *Steel01* material model and (b) using the *Hysteretic* material.

The resulting fragility curves are shown in Figure 11. Notice the difference between the baseline model and models with EPP hinges is relatively small, on the order of approximately 15 % or less. For the 4-story ELF-design the baseline, v1a, and v1b S_T / S_{MT} at 50 % probability of collapse is 2.18, 1.94, and 2.04, respectively. For the 8-story ELF-design the baseline, v1a, and v1b S_T / S_{MT} at 50 % probability of collapse is 2.01, 1.69, and 1.81, respectively. All the results are tabulated at the end of this section. The difference seen between v1a and v1b suggests the panel zone model has influence on the fragility curve but does not change the outcome related to meeting the acceptable collapse margin for the ELF-designs.

In contrast, for the 8-story RSA-design, the baseline, v1a, and v1b S_T / S_{MT} at 50 % probability of collapse is 1.46, 1.28, and 1.32, respectively. When these numbers are adjusted by the spectral shape factor to get the adjusted collapsed margin ratio (recall the SSF equals 1.35 for this case), both variations using the EPP hinge do not have large enough margins against collapse to pass the assessment, therefore this assumption *does* change the outcome for this structure. Though not checked, this is likely the case for the 16-story RSA-designed frame as well, since it too narrowly passes the FEMA P695 assessment.

Note, the model with the EPP hinges is conservative (relative to the baseline) for these sets of runs, which is counter-intuitive considering no strength degradation is captured. It is hypothesized that the zero post-yield stiffness of the EPP model has more influence on the response than the in-cycle degradation of the baseline model. It may be the case that the structural response is largely determined before the hinge rotation of θ_p is reached. If this is the case, the EPP has less energy under the force-deformation curve. Therefore, it supports the fragility curve results presented.

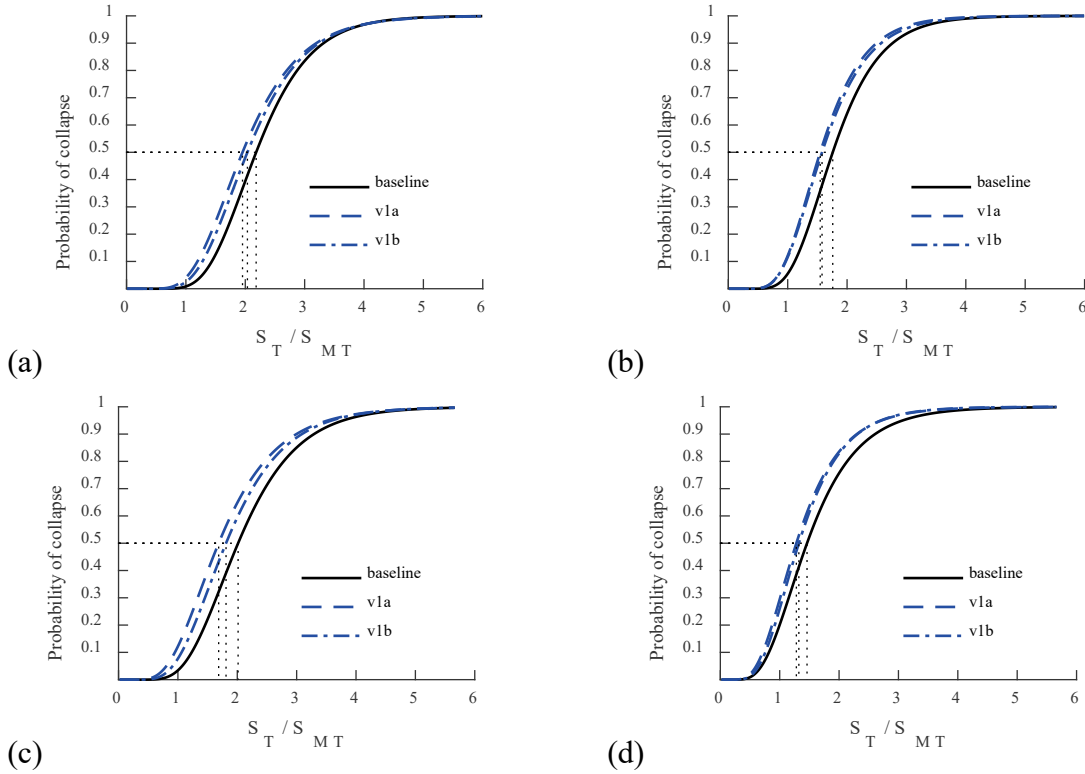


Figure 11. Comparison of fragility curves for the (a) 4-story ELF, (b) 4-story RSA, (c) 8-story ELF, and (d) 8-story RSA-designed frames using elastic plastic hinges (variation v1).

6.2. Varied Predictive Equations

The second variation, v2, is done using varied RBS hinge properties only. Recall the predictive equations are the baseline and then the deformation parameters (θ_p and θ_{pc}) and the deterioration parameter (Λ) are varied by $+/-$ the coefficient of variation (COV) as illustrated in Figure 12. Variation v2a is considered the plus (+) COV case and v2b is the minus (-) COV case. The COV for the RBS hinges is assumed to be 0.30 as reported in NIST [19]. The resulting fragility curves are shown in Figure 13.

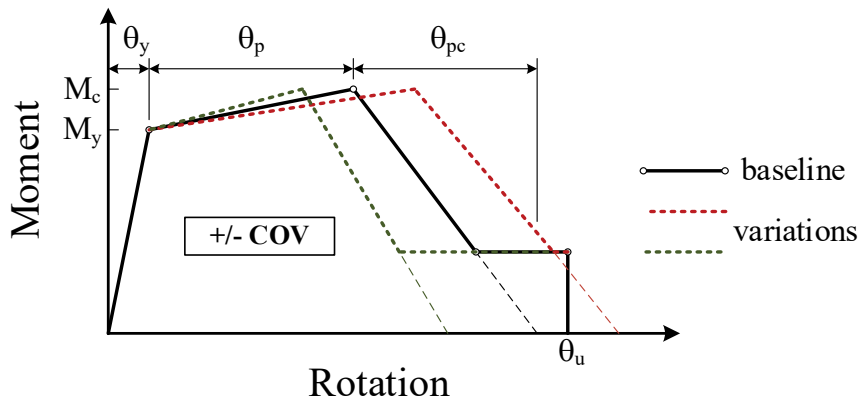


Figure 12. Example illustration of RBS hinge behavior for variation v2.

For the model with a 30 % reduction on the deformation backbone parameters, the fragility curves generally move slightly to the left of the baseline model, though the slope also slightly changes. For the model with a 30 % increase on the deformation backbone parameters, there is very little change in the fragility curves. This suggests that the column hinges may be controlling the collapse behavior of the frames and making modest changes to the RBS hinges has minimal impact on the overall fragility curve and resulting collapse margin ratio.

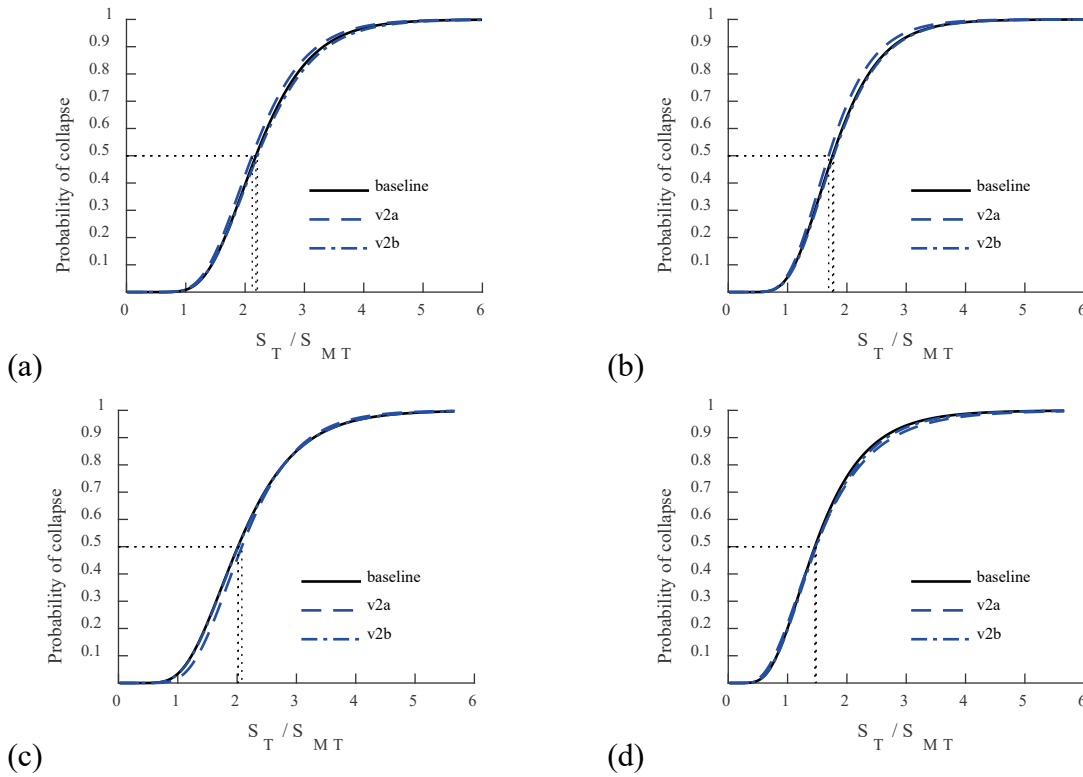


Figure 13. Comparison of fragility curves for the (a) 4-story ELF, (b) 4-story RSA, (c) 8-story ELF, and (d) 8-story RSA-designed frames using + / - COV from the predictive equations (variation v2).

6.3. Predictive Equations vs Experimentally Calibrated

The third variation, v3, studies the difference between parameters determined using the predictive equations and parameters calibrated to an experimental test. To study this effect, the 4-story RSA model is used, which has an RBS similar to one of the RBS connections tested in the steel database: Specimen CW-2 tested by Uang et al. [29]. The model is modified by changing the W24×55 section used for the 4-RSA design to a W24×62 section in the steel database [30]. The “predictive” model uses the Lignos equations to define the deterioration parameters, and the “calibrated” model uses the basic deterioration model parameters after calibration of the moment-rotation diagram of the individual components as determined by Lignos [31]. The parameters for each model are given in Table 6. Figure 14 illustrates the parameters graphically and conceptually demonstrates the difference between the predictive backbone (solid black line) and the individually calibrated backbone (dashed red line).

The resulting fragility curves are shown in Figure 15; the difference in the curves is negligible. This is logical given the reasonably similar modeling parameters between the two models and the results observed for variation v2.

Table 6. Predictive vs. calibrated parameters used for variation v3.

Model	θ_p	θ_{pc}	Λ
Predictive	0.026	0.184	1.019
Calibrated	0.019	0.170	0.800

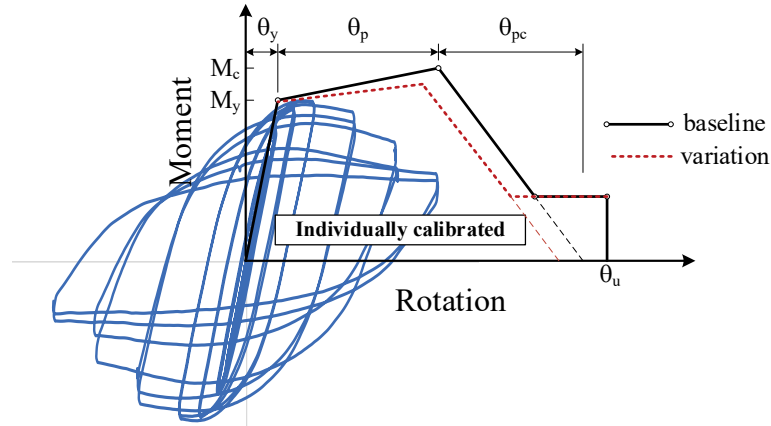


Figure 14. Example illustration of experimentally-calibrated model.

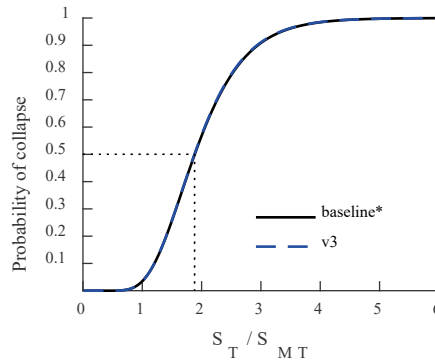


Figure 15. Comparison of fragility curves for an alternative 4-story RSA-designed building using the predictive equations and calibrated to specific experimental data (variation v3).

6.4. Composite-Slab Action

The fourth variation, v4, is done using the RBS hinges only and using the predictive equations that account for composite-slab action as outlined by NIST [19]. The composite slab effectively increases θ_p and θ_{pc} in the positive moment direction but does not affect the negative moment (it is typical to ignore any tensile capacity of the composite slab). Figure

16 shows an illustrative example of the effects of the composite slab on the RBS hinge backbone curve. For this analysis, θ_u is kept the same as the baseline model.

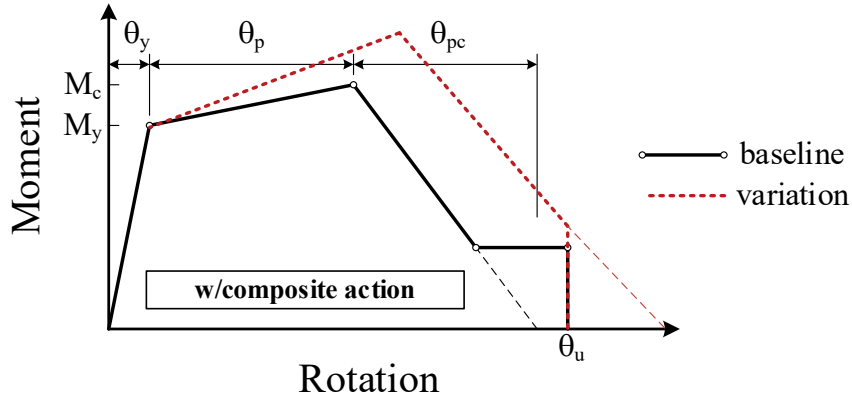


Figure 16. Example illustration of RBS hinge behavior for variation v4 – considering composite slab action.

The resulting fragility curves for the 8-story frames are shown in Figure 17. Accounting for the composite-slab action shifts the fragility curve S_T / S_{MT} at 50 % probability of collapse values from 2.01 to 2.37 and 1.46 to 1.67 in the ELF and RSA-designed frames, respectively. The increased post-yield stiffness caused by the composite-slab action improves the collapse performance. Even though the increased strength of the composite slab results in increased load being transferred to the moment frame columns, no detrimental effects are observed in the analysis results (e.g., formation of a localized story mechanism). This may be due, in part, to the way the P-delta column was modeled; in the baseline model the potential for the non-SMF columns to develop plastic hinges was ignored thus an “elastic spine” along the height of the frame was introduced. The effect of this assumption is explored later in the section. In summary, for these select cases, using the baseline model can be considered conservative in terms of collapse margin ratio.

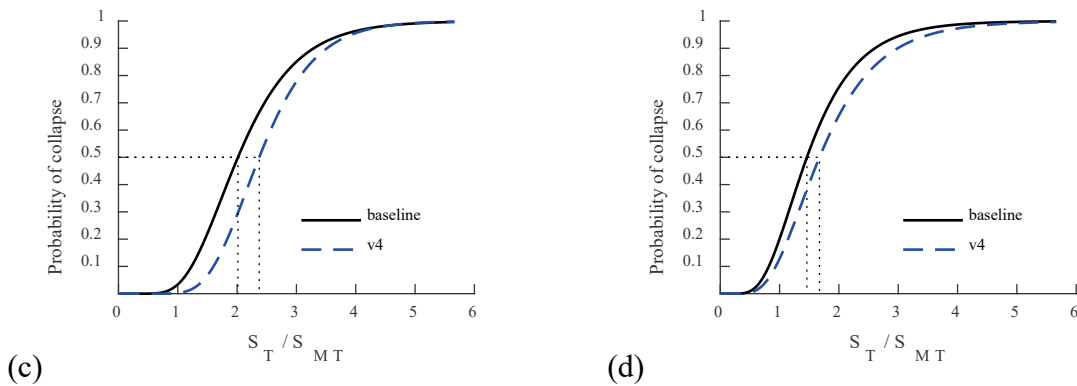


Figure 17. Comparison of fragility curves for the (a) 8-story ELF and (b) 8-story RSA-designed frames accounting for composite slab action (variation v4).

6.5. Damping

The fifth variation, v5, is done using varying levels of damping. Recall that 3 % modal damping is assumed for all modes in structural models used in Harris and Speicher [3] and for the baseline models in this report. Additionally, 0.3 % stiffness proportional damping is added to damp out spurious higher modes as recommended by the Perform 3D User Manual [32].

To test the assumption of 3 % modal damping, extra simulations with the following modal damping values are conducted: (a) 2 %, (b) 1 %, and (c) 0.1 %. Due to the computational cost of running extensive parameter studies, the variations in this section are done for the 8-story frames only, to see if it was worth pursuing further. The resulting fragility curves are shown in Figure 18. The results show that as the damping levels are decreased, the fragility curve shifts to the left. For the 8-story ELF and RSA-designed frames the S_T/S_{MT} at 50 % probability of collapse values shift from 2.01 to 1.90 and 1.46 to 1.26, respectively, when going from 3 % modal damping to 0.1 % modal damping. Naturally the shift from 3 % modal damping to 2 % modal damping is less – the S_T/S_{MT} at 50 % probability of collapse values shift from 2.01 to 1.96 and 1.46 to 1.39 for the 8-story ELF and RSA-designed frames, respectively. From these results, it is concluded that the sensitivity of the collapse fragilities to the modal damping assumption does not change the performance outcome (i.e., the frames still pass the FEMA P695 criteria regardless of the assumed damping). However, it may be pertinent to investigate the effects of different damping models and the effects on different frame types and heights.

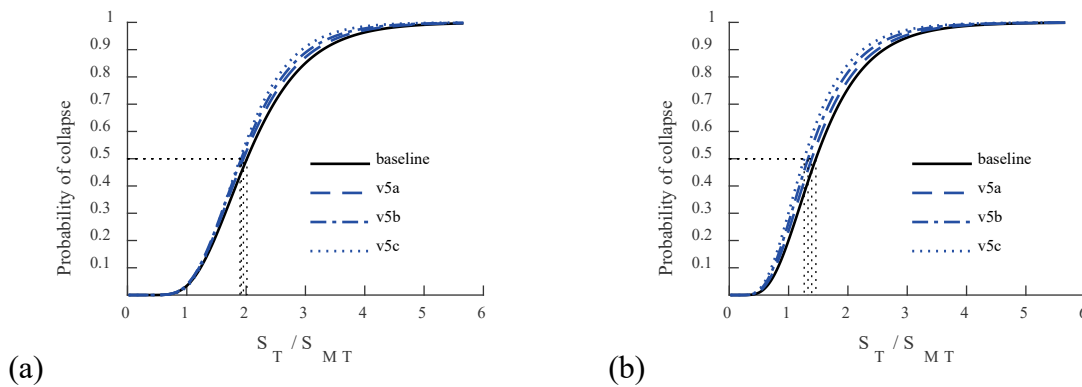


Figure 18. Comparison of fragility curves for the (a) 8-story ELF and (d) 8-story RSA-designed frames accounting varying modal damping levels (variation v5).

6.6. P-Delta Column

The sixth variation, v6, is done to investigate the effects of different P-Delta, or leaning, column modeling approaches. Recall that, since the model is 2D, a leaning column is needed to properly capture second-order geometric effects. Various choices for stiffness and strength for the leaning column can be rationalized. Figure 19 shows the different leaning column modeling approaches investigated in this section.

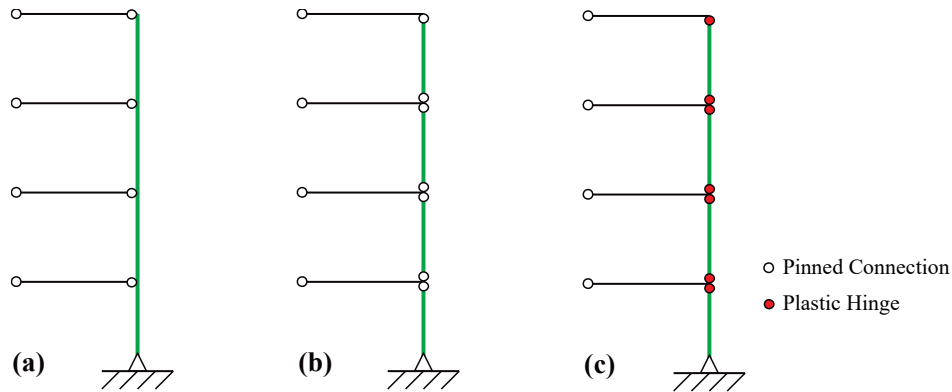


Figure 19. Leaning column modeling approaches for variation v6: (a) baseline model using a continuous member, (b) v6a using pinned connections, and (c) v6b using plastic hinges.

For the baseline model, the leaning column is modeled with a continuous column (no hinges) that has the bending stiffness equal to the sum of all the non-SMF columns at each story. This results in creating an elastic “spine” along the height of the building, promoting an equal distribution of drift demands along the height of the frame and thus discouraging the formation of story mechanisms. This leaning column approach can be considered one extreme. Another extreme is assuming the leaning column is “pinned” at the top and bottom of each story, and thus has zero lateral strength and stiffness; this approach is deemed variation v6a. For v6a, the second-order geometric effects are still captured by the applied gravity loads, but otherwise the leaning column just goes along for the ride. Finally, a more “middle ground” approach is that the leaning column has the stiffness of the non-SMF columns but is also allowed to form plastic hinges based on some logical approximation of the flexural strength; this approach is referred to as variation v6b. For simplicity, the leaning column is given elastic-plastic hinges at each end. The hinges are given a strength equal to the sum of the plastic moments of the non-SMF columns. In reality, the effects of the floor diaphragm make this a more complicated problem, since it is reasonable to anticipate all columns would not yield simultaneously. None-the-less, these effects are not explored herein.

The resulting fragility curves are shown in Figure 20. In general, the assumed modeling approach for the leaning column does not have a significant effect on the collapse fragility. For all frames, modeling the leaning column with a plastic hinge at the top and bottom of each story (v6b) does not appear to affect the results. For the 4-story frames, there is an indistinguishable change in the fragility curve between the variations. For the 8-story and 16-story frames, the S_T / S_{MT} at 50 % probability of collapse values shift slightly to the left for the pinned variation (v6a), but it does not change the assessment outcome. From these results, it is concluded that the sensitivity of the collapse fragilities to the P-delta column modeling assumption is not significant for this set of frames.

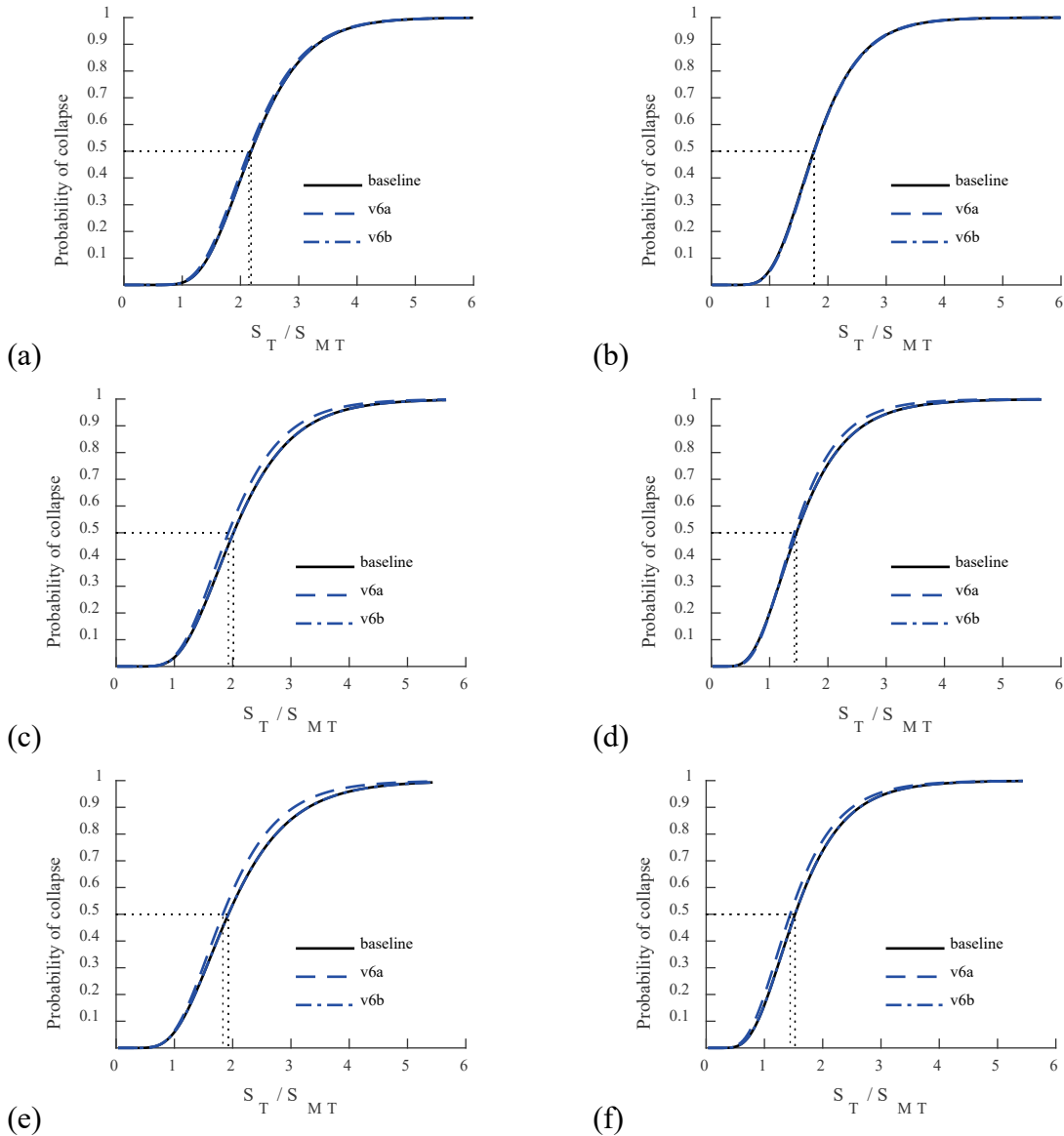


Figure 20. Comparison of fragility curves for the (a) 4-story ELF, (b) 4-story RSA, (c) 8-story ELF, (d) 8-story RSA, (e) 16-story ELF, and (f) 16-story RSA-designed frames using different modeling approaches for the leaning column (variation v6).

6.7. Discussion of Sensitivity Results

The results shown in this section indicate the model is influenced by each of the parameters varied herein, but not by a degree that any one variation changes the outcome of the collapse performance determination. The sensitivity study results are summarized in Table 7 and Table 8. Cells with a dash or “-” denote that no case was ran for this combination. Table 7 gives the results in terms of collapse margin ratios and Table 8 gives the same information but normalized by the baseline results. For reference, the shaded areas in Table 8 indicate a greater than 10 % change from the baseline.

It is found that assuming simplified elastic-plastic behavior in the RBS hinges is conservative (variation v1), which is counterintuitive because the model does not adequately capture degradation. The collapse margin ratio decreases up to 16 % in the cases studied. The elastic-plastic model also does not benefit from the effects of a positive post-yield slope (strain hardening), which tends to improve performance. Regardless, it is hypothesized that the global stability issue becomes the controlling factor in performance at the point where the hinge would realistically see strength degradation.

It is found that when varying the beam hinges by plus or minus the coefficient of variation (COV) (variation v2) the results change 4 % or less. As mentioned previously, this suggests that this level of change to the beam hinges did not greatly change the collapse behavior of the frames represented by the fragility curve and resulting collapse margin ratio.

It is found that changing the RBS hinge properties to match specific experimental results (variation v3) has a 7 % increase on the collapse margin ratio for the 4-story *original* RSA-designed frame. However, recall that the comparison made in variation v3 was made using a *modified* 4-story RSA-designed frame, with slightly increased beam sizes. This resulted in increased *CMR* for both the baseline and the v3 model. After reviewing Figure 15, the results clearly show the fragility curve does not change for this variation.

It is found that the median collapse margins are most sensitive to the composite-slab action (variation v4). For example, the collapse margin ratio for the 8-story ELF-designed frame is 18 % greater than the baseline collapse margin ratio. This result is logical given the extra strength, ductility, and post-yield stiffness of each beam hinge. In comparison to variation v2, in which smaller changes to the ductility of the beam hinges were made, the changes made in this variation had greater impact on the fragility curve. By not accounting for the composite slab, the collapse margin ratio result is found to be conservative in the baseline models.

It is found that reducing the assumed damping (variation v5) from that used in the baseline model can have up to a 13 % decrease on the collapse margin ratio for the buildings studied in this variation. The trend observed meets expectations. For buildings that are near the pass / fail boundary, assuming a smaller damping ratio can change the outcome. However, the majority of the baseline models investigated in this study have adjusted collapse margin ratios sufficiently greater than the acceptable collapse margin ratio. Therefore, increasing the conservatism (i.e., reducing the assumed damping ratio) would not change the overall outcome for most of the frames in this study.

Finally, the effects of P-delta modeling assumptions are tested (variation v6). It is found that the details of the P-delta column do not have a large effect on the collapse margin ratios. Creating a plastic hinge at the top and bottom of the columns did not change the results. This was due to these hinges never yielding – therefore the model was essentially the same as the baseline model. If the stiffness of the P-delta column is ignored (by pinning the column ends), the collapse margin ratios decreased, but only up to 5 % in the cases investigated herein. This indicates the frames were not prone to forming story mechanisms, but rather had a more uniform distribution of demands. The P-delta column modeling approach did not greatly influence the assessment outcome. This behavior should be verified as part of further studies.

In summary, the select sensitivity studies gives insight into the independent effects of several modelling parameters and assumptions. However, it is recognized that this sensitivity study was limited in scope due to the computational expense that is required to run IDA. In such, the effects of changing combinations of parameters were not explored.

Table 7. Summary of results for the sensitivity study in terms or collapse margin ratio.

Building	$CMR = S_T / S_{MT}$ at 50 % probability of collapse											
	Baseline	v1		v2		v3	v4	v5			v6	
		a	b	a	b			a	b	c	a	b
04-ELF	2.18	1.95	2.04	2.12	2.21	-	-	-	-	-	2.14	2.18
04-RSA	1.76	1.55	1.58	1.69	1.78	1.88	-	-	-	-	1.77	1.77
08-ELF	2.01	1.69	1.81	2.08	2.02	-	2.37	1.95	1.92	1.90	1.93	2.01
08-RSA	1.46	1.28	1.32	1.47	1.48	-	1.67	1.39	1.33	1.26	1.42	1.46
16-ELF	1.93	-	-	-	-	-	-	-	-	-	1.83	1.93
16-RSA	1.53	-	-	-	-	-	-	-	-	-	1.44	1.53

Table 8. Summary of results for the sensitivity study normalized by the baseline results.

Building	$CMR / CMR_{(Baseline)}$											
	Baseline	v1		v2		v3	v4	v5			v6	
		a	b	a	b			a	b	c	a	b
04-ELF	1.00	0.89	0.93	0.97	1.01	-	-	-	-	-	0.98	1.00
04-RSA	1.00	0.88	0.90	0.96	1.01	1.07 ^a	-	-	-	-	1.00	1.00
08-ELF	1.00	0.84	0.90	1.03	1.00	-	1.18	0.97	0.95	0.94	0.96	1.00
08-RSA	1.00	0.88	0.91	1.01	1.02	-	1.15	0.95	0.91	0.87	0.98	1.00
16-ELF	1.00	-	-	-	-	-	-	-	-	-	0.95	1.00
16-RSA	1.00	-	-	-	-	-	-	-	-	-	0.95	1.00

Note: a. This is the value compared to the baseline model, not the modified model actually compared in variation v3.

7. Conclusions

A set of buildings designed using ASCE 7 and assessed using ASCE 41 were shown to be deficient (per ASCE 41) in previous investigations by Harris and Speicher [3-5]. The ASCE 41 assessment results appeared to be conservative for the nonlinear dynamic procedure relative to the linear procedures. To further vet the performance of these buildings and understand the differences between new building design and existing building assessment, this report presents an investigation of the collapse probability of six special moment frames using the FEMA P695 methodology and associated incremental dynamic analysis. The results demonstrate that the ASCE 7-designed frames meet the intent of the building code, which is having less than or equal to a 10 % probability of collapse given a maximum considered earthquake.

Meeting the intent of the building code is demonstrated through subjecting this set of buildings to a suite of far field ground motions specified in FEMA P695 and then calculating each building's collapse margin ratio. Assumptions consistent with both the previous NIST study and state-of-the-art modeling techniques for global-level assessment are implemented. The sensitivity to key modeling assumptions are explored, with the baseline model assumptions being found to be either conservative or only marginally unconservative. This report notes the high-level similarities and the differences in the results for the ASCE 41 assessment and the FEMA P695 methodology and suggest that implementing the ASCE 41 modeling parameters in a Perform-3D model may contribute to the conservative assessment outcome.

The results herein showing the set of buildings meeting the intent of ASCE 7 stands in contrasts to the previous assessment conducted on these buildings using ASCE 41 which suggested the buildings are not sufficiently designed. This indicates ASCE 41 may be overly-conservative in its assessment criteria. It is recommended that further study be done to confirm the conclusions presented herein and address the conservatism implied in these results. One potential approach is migrating ASCE 41 assessment criteria into a cumulative-based approach by using dissipated energy or equivalent as acceptance criteria.

Acknowledgments

The authors would like to thank the members of Earthquake Engineering Group at NIST for their support.

References

- [1] ASCE (2017) Minimum Design Loads for Buildings and Other Structures. in *ASCE/SEI 7-16* (American Society of Civil Engineers, Reston, VA).
- [2] ASCE (2017) Seismic Evaluation and Retrofit of Existing Buildings. in *ASCE/SEI 41-17* (American Society of Civil Engineers, Reston, VA).
- [3] Harris JL , Speicher MS (2015) Assessment of First Generation Performance-Based Seismic Design Methods for New Steel Buildings Volume 1: Special Moment Frames. (National Institute of Standards and Technology, Gaithersburg, MD), NIST Technical Note 1863-1. <https://doi.org/10.6028/NIST.TN.1863-1>
- [4] Harris JL , Speicher MS (2015) Assessment of First Generation Performance-Based Seismic Design Methods for New Steel Buildings Volume 2: Special Concentrically Braced Frames. (National Institute of Standards and Technology, Gaithersburg, MD), NIST Technical Note 1863-2. <https://doi.org/10.6028/NIST.TN.1863-2>
- [5] Harris JL , Speicher MS (2015) Assessment of First Generation Performance-Based Seismic Design Methods for New Steel Buildings Volume 3: Eccentrically Braced Frames. (National Institute of Standards and Technology, Gaithersburg, MD), NIST Technical Note 1868-3. <https://doi.org/10.6028/NIST.TN.1863-3>
- [6] ASCE (2006) Seismic Rehabilitation of Existing Buildings. in *ASCE/SEI 41-06* (American Society of Civil Engineers, Reston, VA).
- [7] ASCE (2010) Minimum Design Loads for Buildings and Other Structures. in *ASCE/SEI 7-10* (American Society of Civil Engineers, Reston, VA).
- [8] AISC (2010) Seismic Provisions for Structural Steel Buildings. in *ANSI/AISC 341-10* (American Institute of Steel Construction, Chicago, IL).
- [9] McKenna F , Fenves GL (2016) OpenSees command language manual. Version 2.5.0 (Pacific Earthquake Engineering Research Center, Berkeley, CA).
- [10] FEMA (2009) Quantification of Building Seismic Performance Factors. in *FEMA P695* (Federal Emergency Management Agency, Washington, D.C.).
- [11] NIST (2009) Research Required to Support Full Implementation of Performance-Based Seismic Design. (Prepared by the Building Seismic Safety Council for the National Institute of Standards and Technology, Gaithersburg, MD), NIST GCR 09-917-2.
- [12] NIST (2012) Tentative Framework for Development of Advanced Seismic Design Criteria for New Buildings. (Prepared by the NEHRP Consultants Joint Venture, a partnership of the Applied Technology Council and the Consortium of Universities for Research in Earthquake Engineering, for the National Institute of Standards and Technology, Gaithersburg, MD), NIST GCR 12-917-20.
- [13] Harris J , Speicher MS (2018) Assessment of Performance-Based Seismic Design Methods in ASCE 41 for New Steel Buildings: Special Moment Frames. *Earthquake Spectra* 34(3):977-999. <https://doi.org/10.1193/050117EQS079EP>
- [14] Speicher MS , Harris JL (2016) Collapse Prevention Seismic Performance Assessment of New Eccentrically Braced Frames using ASCE 41. *Engineering Structures* 117:344-357. <https://doi.org/10.1016/j.engstruct.2016.02.018>
- [15] Speicher MS , Harris JL (2016) Collapse prevention seismic performance assessment of new special concentrically braced frames using ASCE 41. *Engineering Structures* 126:652-666. <https://doi.org/10.1016/j.engstruct.2016.07.064>

- [16] Speicher MS , Harris JL (2018) Collapse Prevention seismic performance assessment of new buckling-restrained braced frames using ASCE 41. *Engineering Structures* 164:274-289. <https://doi.org/10.1016/j.engstruct.2018.01.067>
- [17] Uribe R, Sattar S, Speicher MS, Ibarra L (2017) Influence of Ground Motion Selection on the Assessment of a Steel Special Moment Frame. *16th World Conference on Earthquake Engineering*, (Santiago, Chile).
- [18] Maison BF , Speicher MS (2016) Loading Protocols for ASCE 41 Backbone Curves. *Earthquake Spectra* 32(4):1-20. <https://doi.org/10.1193/010816EQS007EP>
- [19] NIST (2017) Guidelines for Nonlinear Structural Analysis for Design of Buildings, Part IIa – Steel Moment Frames. (Gaithersburg, MD), NIST GCR 17-917-46v2. <https://doi.org/10.6028/NIST.GCR.17-917-46v2>
- [20] CSI (2013) Nonlinear Analysis and Performance Assessment for 3D Structures (Computers and Structures, Inc., Berkeley, CA), Version 5.0.
- [21] Ibarra LF, Medina RA, Krawinkler H (2005) Hysteretic models that incorporate strength and stiffness deterioration. *Earthquake Engineering and Structural Dynamics* 34(12):1489-1511.
- [22] Lignos DG , Krawinkler H (2011) Deterioration modeling of steel components in support of collapse prediction of steel moment frames under earthquake loading. *Journal of Structural Engineering* 137(11):1291-1302. [https://doi.org/10.1061/\(ASCE\)ST.1943-541X.0000376](https://doi.org/10.1061/(ASCE)ST.1943-541X.0000376)
- [23] Krawinkler H (1978) Shear in Beam-Column Joints in Seismic Design of Steel Frames. *Engineering Journal* 15(3):82-91.
- [24] Vamvatsikos D , Allin Cornell C (2002) Incremental Dynamic Analysis. *Earthquake Engineering and Structural Dynamics* 31(3):491-514. <https://doi.org/10.1002/eqe.141>
- [25] Hardyniec A , Charney F (2016) A Toolkit for Performing FEMA P-695 Evaluations. *Earthquake Spectra* 32(2):653-676. <https://doi.org/10.1193/040214eqs044>
- [26] Porter K, Kennedy R, Bachman R (2007) Creating fragility functions for performance-based earthquake engineering. *Earthquake Spectra* 23(2):471-489. <https://doi.org/10.1193/1.2720892>
- [27] Baker JW (2015) Efficient Analytical Fragility Function Fitting Using Dynamic Structural Analysis. *Earthquake Spectra* 31(1):579-599. <https://doi.org/10.1193/021113eqs025m>
- [28] Towns J, Cockerill T, Dahan M, Foster I, Gaither K, Grimshaw A, Hazlewood V, Lathrop S, Lifka D, Peterson GD, Roskies R, Scott JR, Wilkins-Diehr N (2014) XSEDE: Accelerating Scientific Discovery. *Computing in Science & Engineering* 16(5):62-74. <https://doi.org/10.1109/MCSE.2014.80>
- [29] Gilton CS , Uang CM (2002) Cyclic response and design recommendations of weak-axis reduced beam section moment connections. *J Struct Eng-Asce* 128(4):452-463. [https://doi.org/10.1061/\(Asce\)0733-9445\(2002\)128:4\(452\)](https://doi.org/10.1061/(Asce)0733-9445(2002)128:4(452))
- [30] Lignos DG , Krawinkler H (2007) A Database in Support of Modeling of Component Deterioration for Collapse Prediction of Steel Frame Structures. *Research Frontiers at Structures Congress 2007*, (Long Beach, California).
- [31] Lignos DG (2008) Sidesway Collapse of Deteriorating Structural Systems Under Seismic Excitations. (Stanford University).
- [32] CSI (2011) *PERFORM-3D User Guide* (Computers and Structures, Inc., Berkeley, CA).

- [33] Lignos DG, Krawinkler H, Whittaker AS (2011) Prediction and validation of sidesway collapse of two scale models of a 4-story steel moment frame. *Earthquake Engineering and Structural Dynamics* 40(7):807-825.
<https://doi.org/10.1002/eqe.1061>
- [34] Gupta A , Krawinkler H (1999) Seismic demands for performance evaluation of steel moment resisting frame structures. SAC Report No. 132, June 1999.
- [35] Ibarra L , Krawinkler H (2005) Global Collapse of Frame Structures under Seismic Excitations. (PEER Report, University of California, Berkeley, Berkeley, CA), September, 2005.

Appendix A Three-Dimensional Analysis vs. Two-Dimensional Analysis

Three-dimensional (3D) models were developed using Perform-3D to analyze the building performance and the results were documented in Harris and Speicher [3]. However, running 3D models is time-consuming, and it becomes infeasible for incremental dynamic analysis. Since these 3D models are symmetric, simplified two-dimensional (2D) models became the best alternative for the study. This appendix looks at the differences between the nonlinear response history of the 4-story ELF-designed frame modeled in 2D and 3D to verify the validity of this simplifying assumption.

A.1 Modeling of the 4-story ELF Frame in 2D

Reducing the Perform-3D symmetric 3D model to a 2D model is a straightforward process. By deleting all the nodes except for those connected to the 4-story ELF moment frame, all the associated members are automatically deleted. The end result is the entire 2D moment frame that resembles what is used in the 3D model, with all the beam, column, and panel zone elements and the corresponding nonlinear material properties appropriately defined. This is shown in Figure 21.

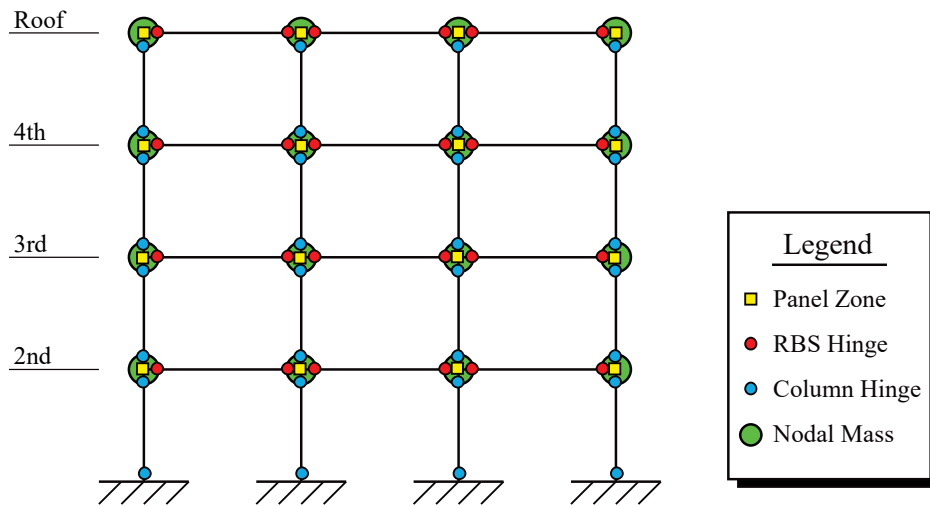


Figure 21. 2D model of the 4-story ELF moment frame.

The restraints at the base on the columns are then modeled as fixed along the 2D directions, which is the same as those in the 3D model. However, with the removal of the slabs from the 3D model, constraints need to be placed on each floor to ensure the 2D horizontal movement remains constant. This is done on each floor of the 2D frame.

The mass is taken as half the total mass of the building, distributed equally among each node as shown in Figure 21. The total mass of each floor of the 3D model and the corresponding mass on each node of the 2D model is shown in Table 9.

Table 9. Mass calculations for the 2D model of the 4-story ELF moment frame.

Floor	Floor Mass of Building - 3D (k-s ² /in)	Mass on Each Node - 2D (k-s ² /in)
2nd	3.569	0.446
3rd	3.522	0.440
4th	3.488	0.436
Roof	2.836	0.355

Finally, similar to the 3D model, the damping in the 2D baseline model is defined using 3 % modal damping in all modes with an additional stiffness proportional damping of 0.3 % at $0.2T_i$ for numerical stability.

A.2 Modeling of the Leaning Column

A leaning column is used in the 2D model to capture the geometric nonlinearity associated with the gravity loads acting on the gravity columns of the building. The leaning column considers all the properties associated with every gravity column in the 3D model. Figure 22 shows the leaning column with links attached to the 2D frame that was discussed in Section A.1. These links are used to show how the leaning column is attached to the frame but do not provide stiffness to the frame in the analysis, since the nodes on each floor of the leaning column are constrained horizontally to the corresponding floor of the 2D frame.

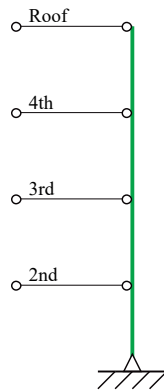


Figure 22. Leaning column of the 2D model.

All gravity columns and out-of-plane concentrically braced frame columns are modeled as pinned at the base in the 3D model. Therefore, the leaning column in the 2D model is also modeled with a pinned support. Altogether there are six gravity columns and four concentrically braced frame columns in the half-structure that need to be captured by the leaning column, and the properties of these columns are summarized in Table 10. The moment of inertia of the leaning column is then calculated by summing the moment of inertias shown in Table 10, and the results are shown in Table 11. Finally, a generic steel section is selected with dimensions calculated based on the required moment of inertias as shown in Table 11.

Table 10. Properties of the gravity columns in the 3D model.

Floor	6 Gravity Columns		4 Braced Frame Columns	
	Section	I_x (in ⁴)	Size	I_y (in ⁴)
Gr-2nd	W14×61	640	W14×132	548
2nd-3rd	W14×61	640	W14×132	548
3rd-4th	W14×38	385	W14×53	57.7
4th-Roof	W14×38	385	W14×53	57.7

Table 11. Properties of the leaning column in the 2D model.

Floor	Moment of Inertia (in ⁴)	Dimension (in × in)
Gr-2nd	6032	16.40 × 16.40
2nd-3rd	6032	16.40 × 16.40
3rd-4th	2541	13.21 × 13.21
4th-Roof	2541	13.21 × 13.21

Using the 2D model of the frame discussed in Section A.1 with the leaning column discussed in Section A.2, the periods are computed and shown in Table 12. In addition, the periods of the 3D model along the moment frame direction is also shown in Table 12 for comparison.

Table 12. Periods of vibration for the 2D and 3D models.

Mode	Period of 2D Model (s)	Period of 3D Model (s)
1	1.813	1.813
2	0.545	0.545
3	0.265	0.268
4	0.158	0.160

A.3 Modeling of the Gravity Loads

To maintain consistency between the 2D model and the 3D model, gravity loads are applied to the 2D model according to the following procedure:

1. Gravity load applied on the beams of the moment frame in the 3D model remains on the beams of the 2D model.
2. Gravity load tributary to the columns of the moment frame in the 3D model is applied directly onto the columns of the 2D model.
3. Gravity load tributary to the gravity columns and out-of-plane concentric braced frame in the 3D model is applied directly onto the leaning column of the 2D model.

The end result of the applied gravity loads is shown in Figure 23.

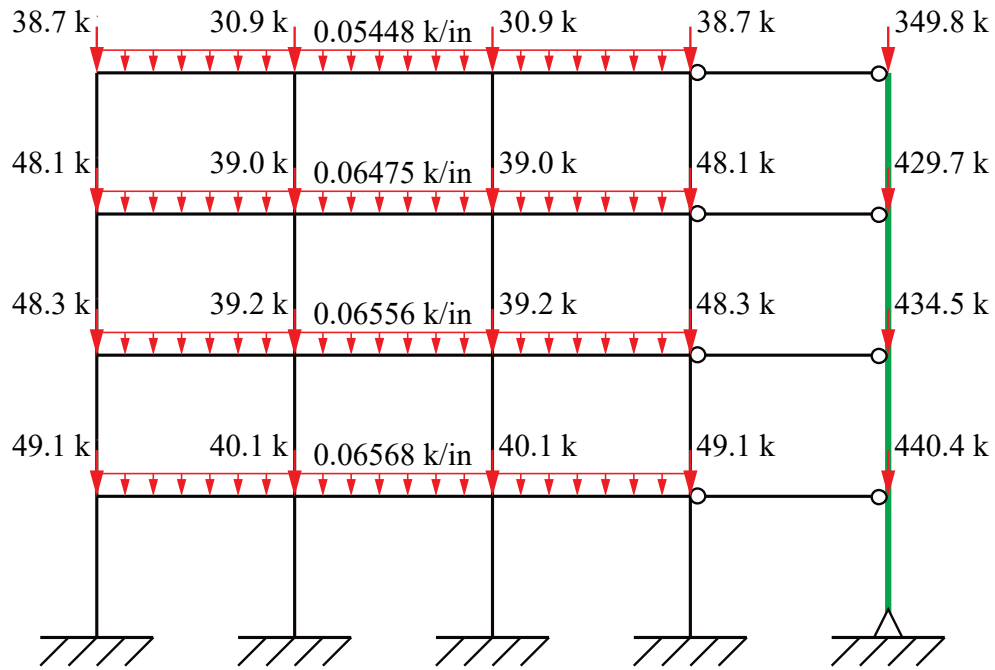


Figure 24. Gravity loads applied on the 2D model (where k = kip).

A.4 Response History Analysis

Response history analysis is performed to compare the displacement responses of the 2D model with those of the 3D model. After applying the gravity loads on the models, 16 earthquake ground motions are selected to perform the numerical simulation. Figures A4 to A20 summarize the displacement response comparisons of each floor. Results show that consistency of outputs is achieved when a symmetric 3D building is modeled in 2D, even for the case at collapse as shown in Figure A5.

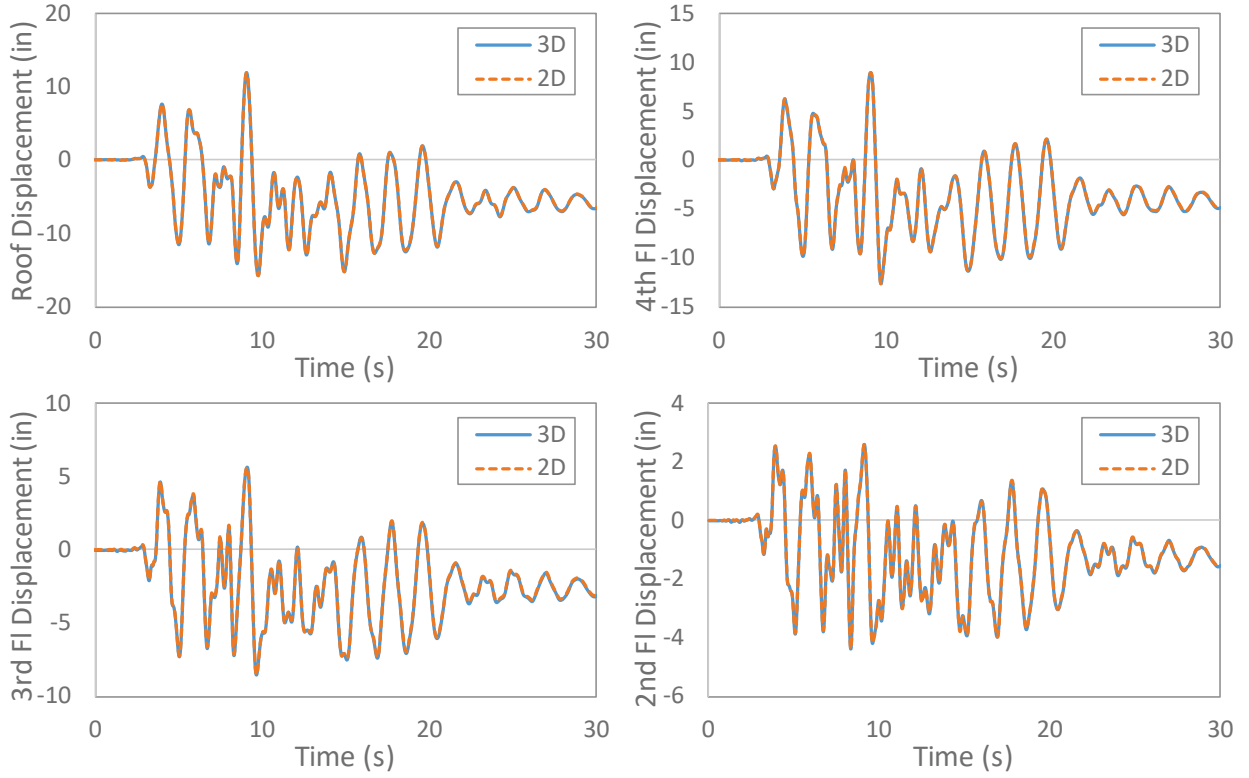


Figure 25. Responses due to 1994 Northridge EQ at Mulholland Drive station, comp 009.

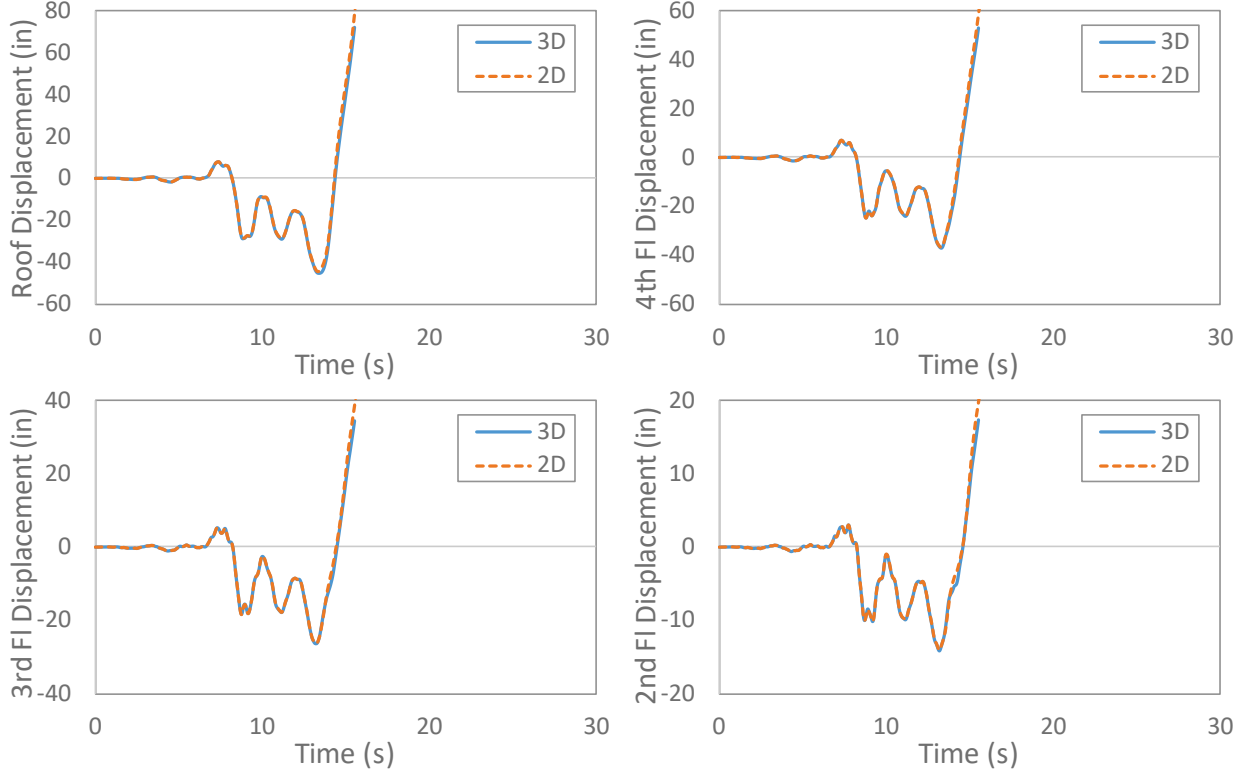


Figure 26. Responses due to 1999 Kocaeli, Turkey EQ at Duzce station, comp 180.

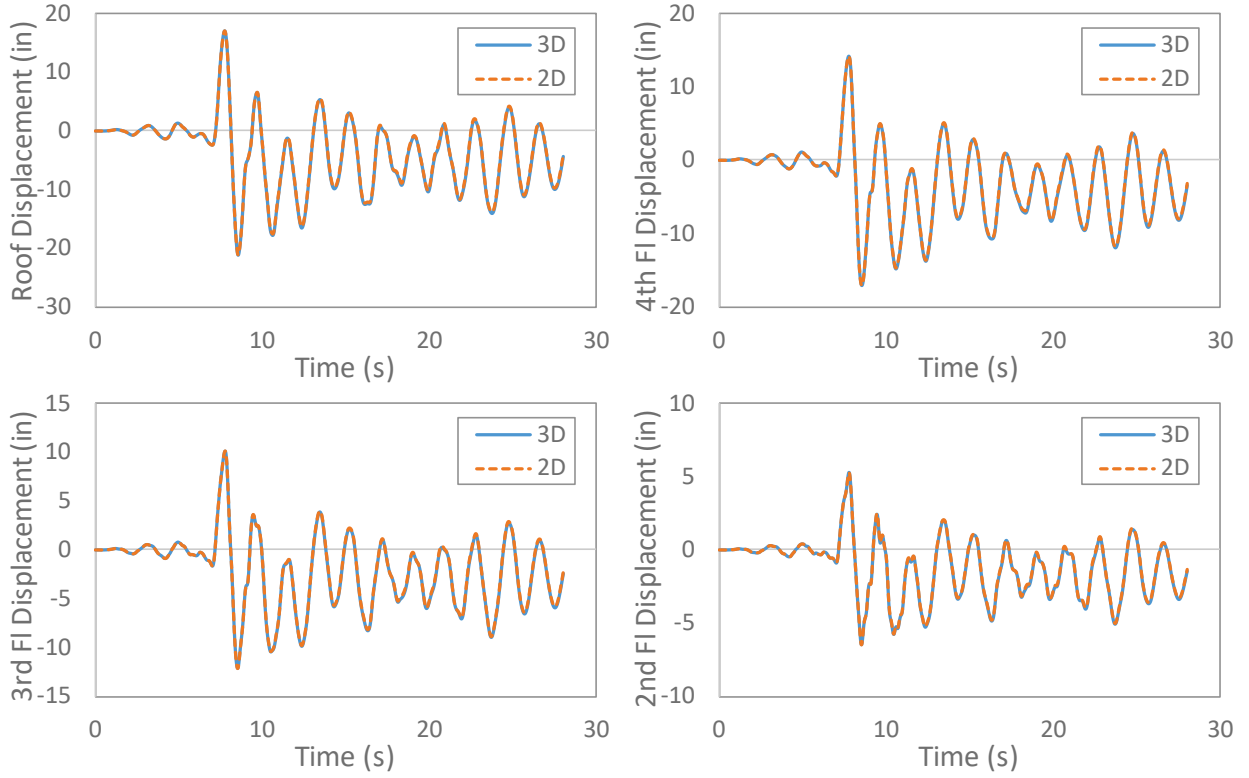


Figure 27. Responses due to 1999 Kocaeli, Turkey EQ at Duzce station, comp 270.

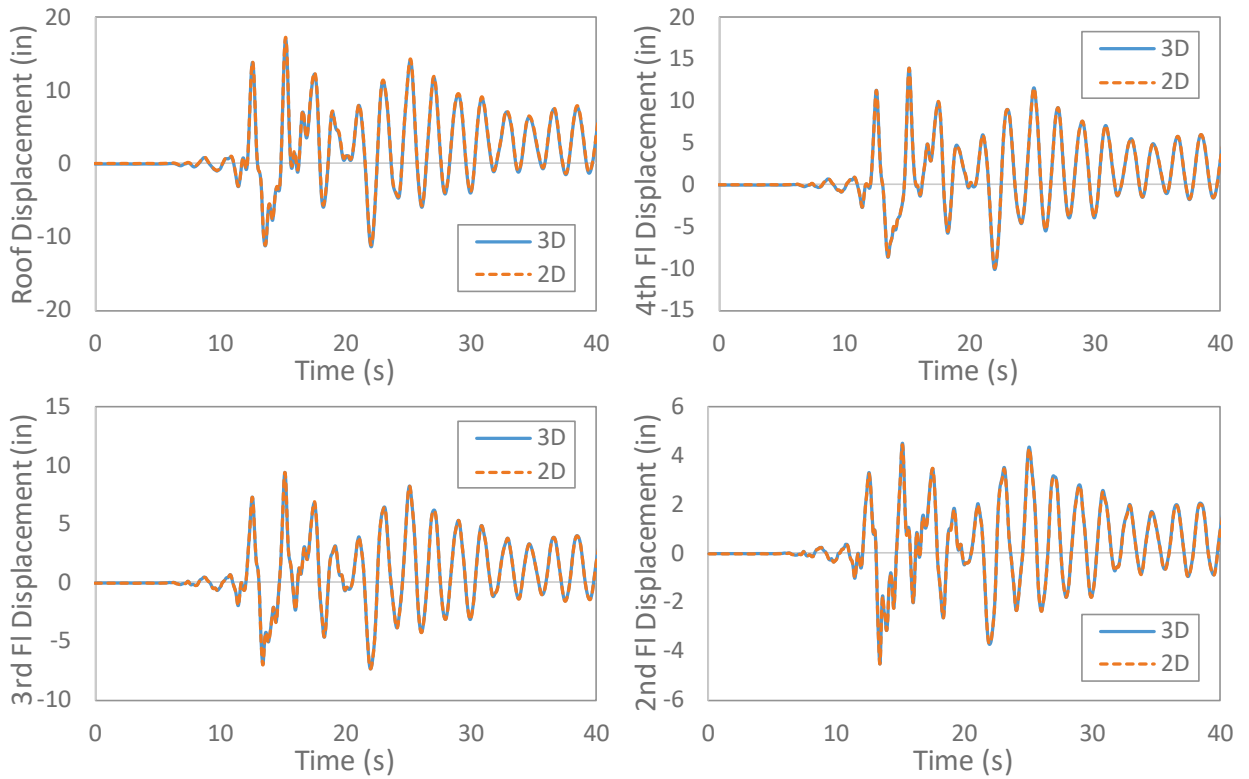


Figure 28. Responses due to 1995 Kobe, Japan EQ at Shin-Osaka station, comp 000.

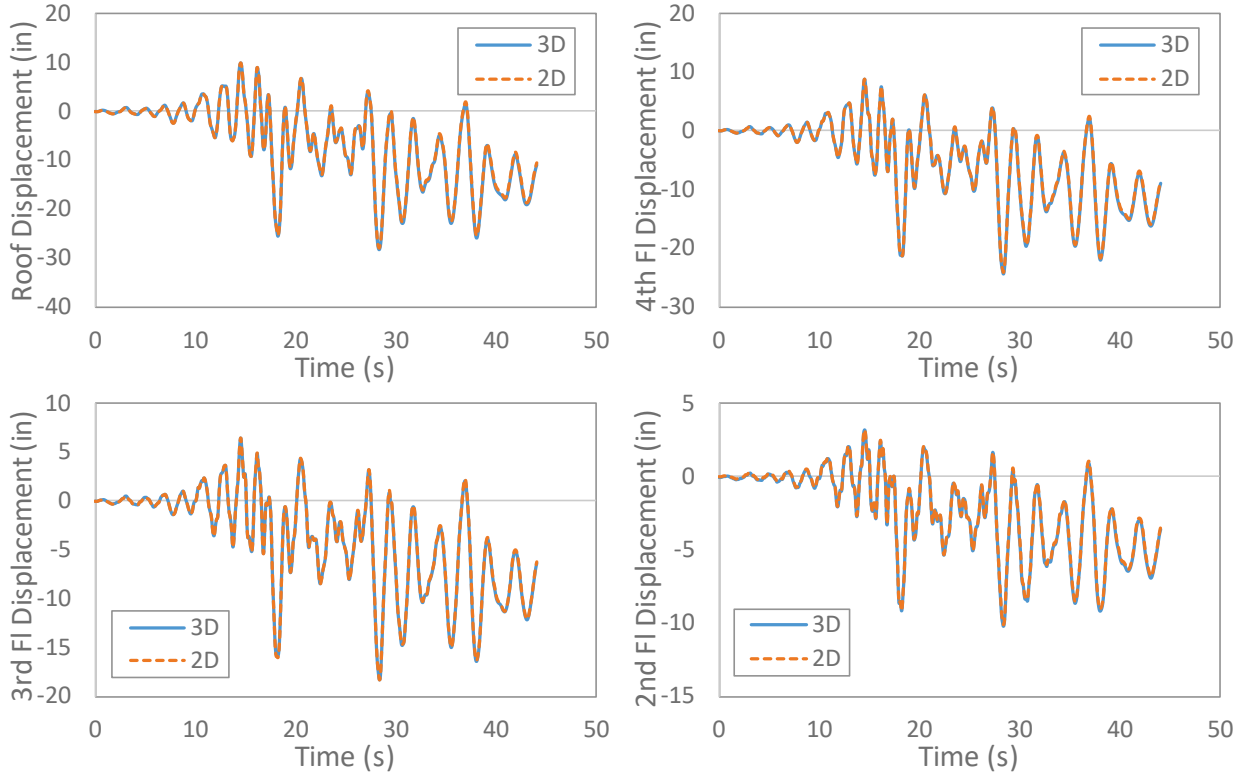


Figure 29. Responses due to 1992 Landers EQ at Yermo fire station, comp 360.

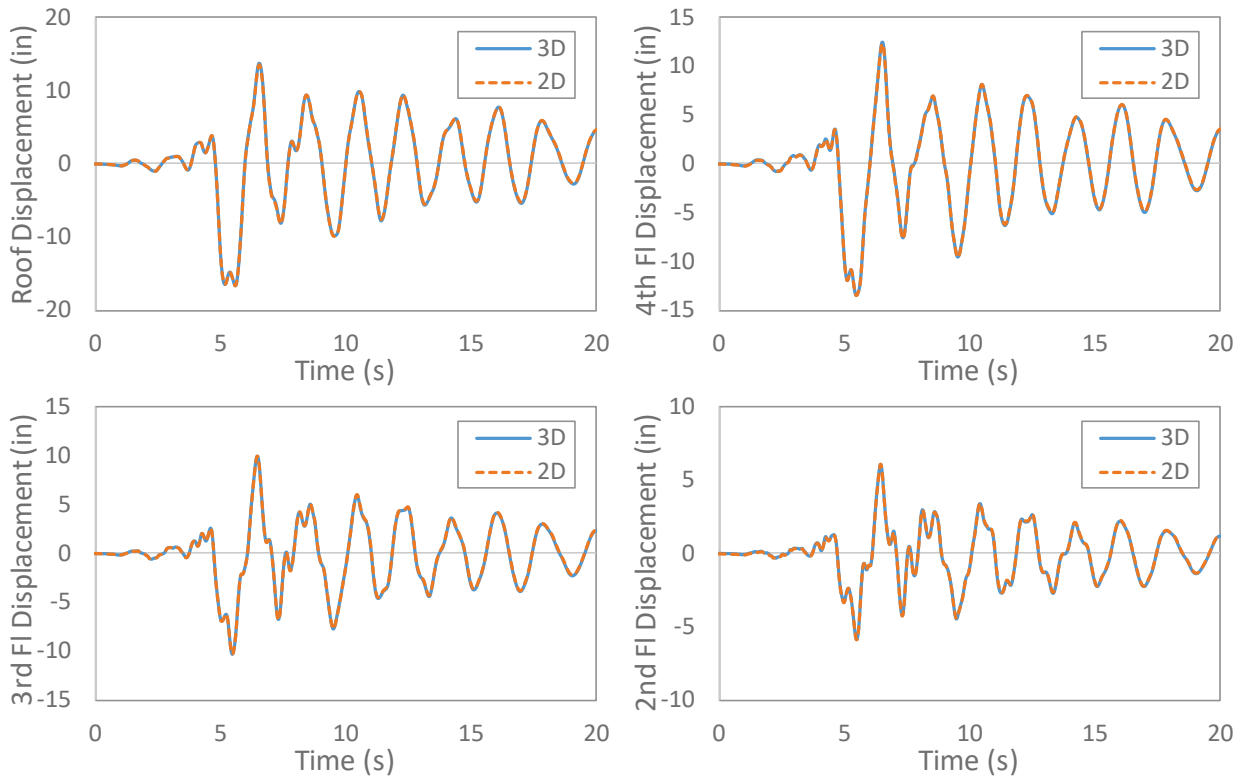


Figure 30. Responses due to 1994 Northridge EQ at Canyon Country station, comp 000.

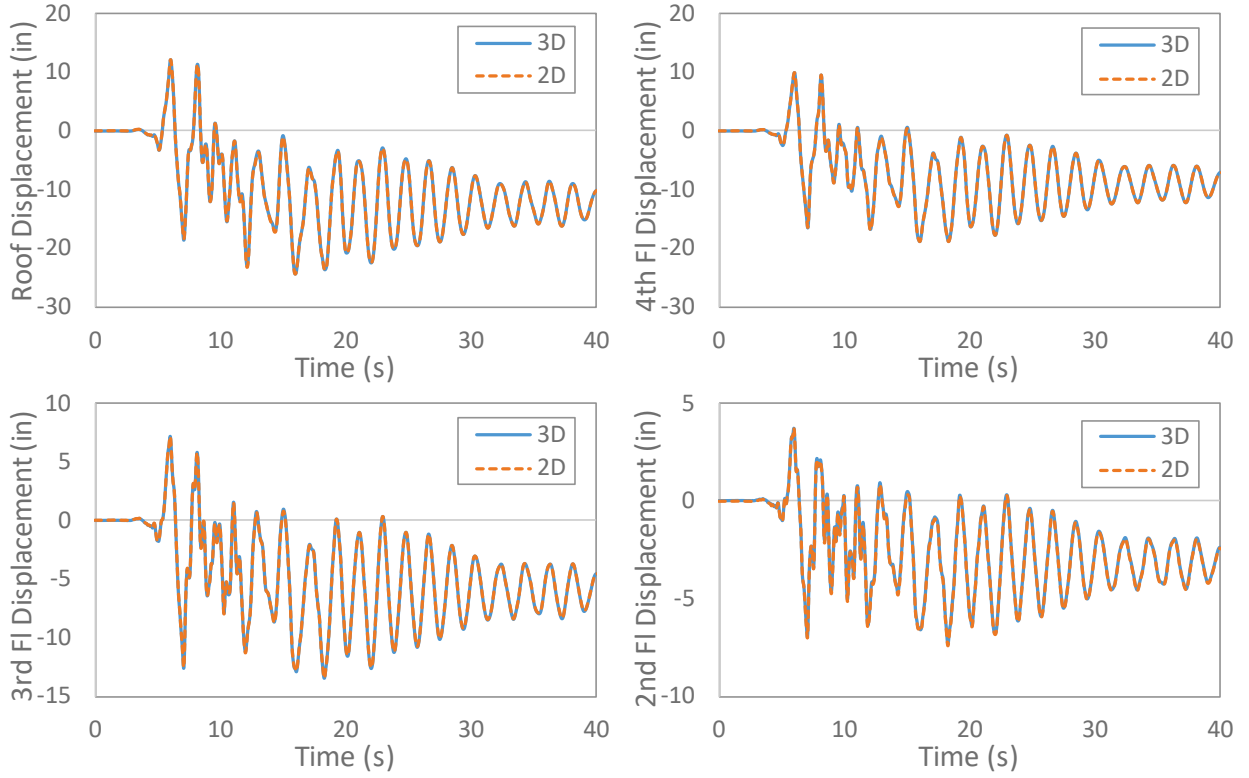


Figure 31. Responses due to 1995 Kobe, Japan EQ at Nishi-Akashi station, comp 090.

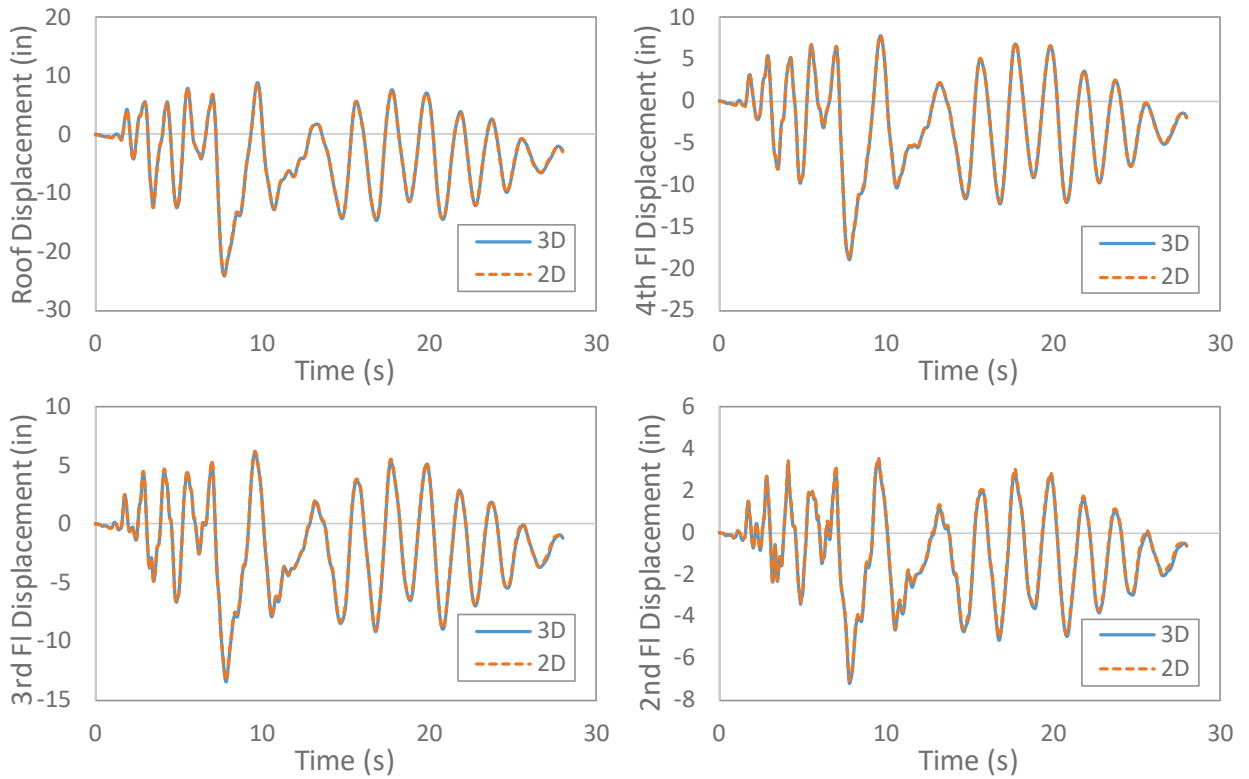


Figure 32. Responses due to 1971 San Fernando EQ at Hollywood station, comp 090.

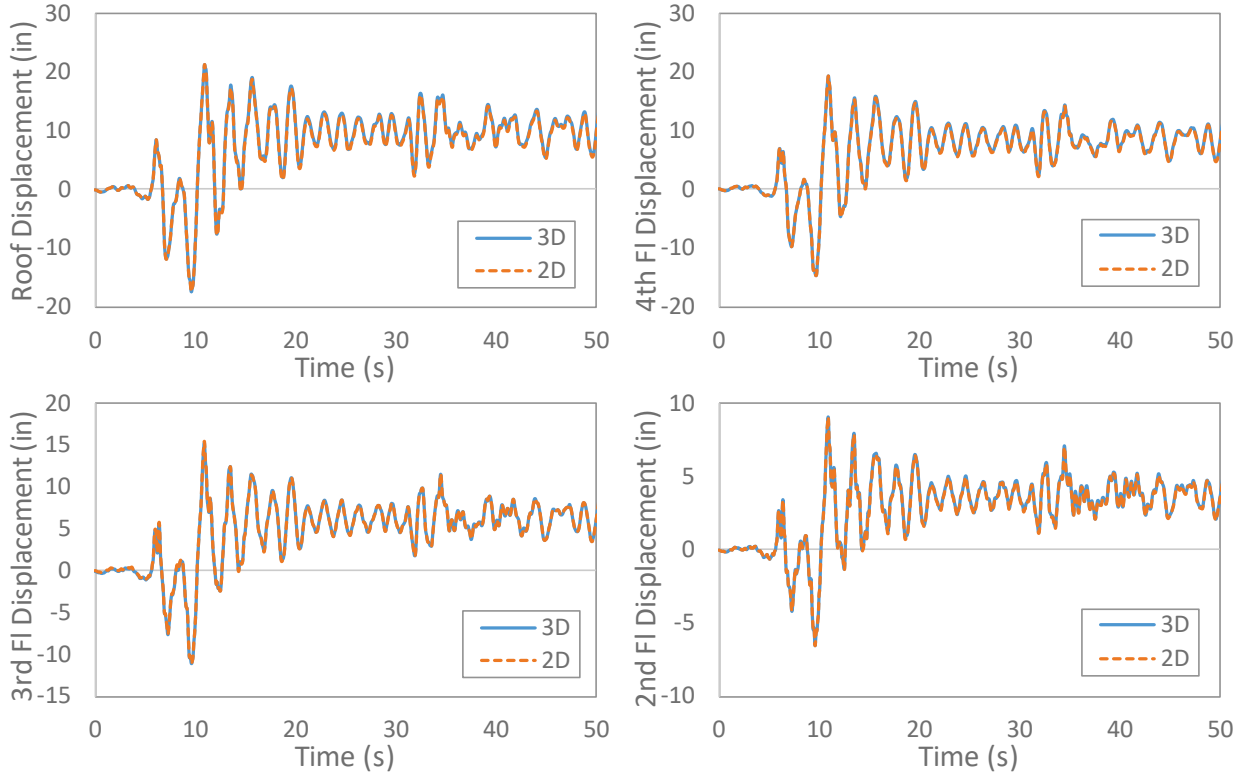


Figure 33. Responses due to 1990 Manjil, Iran EQ at Abbar station, longitudinal comp.

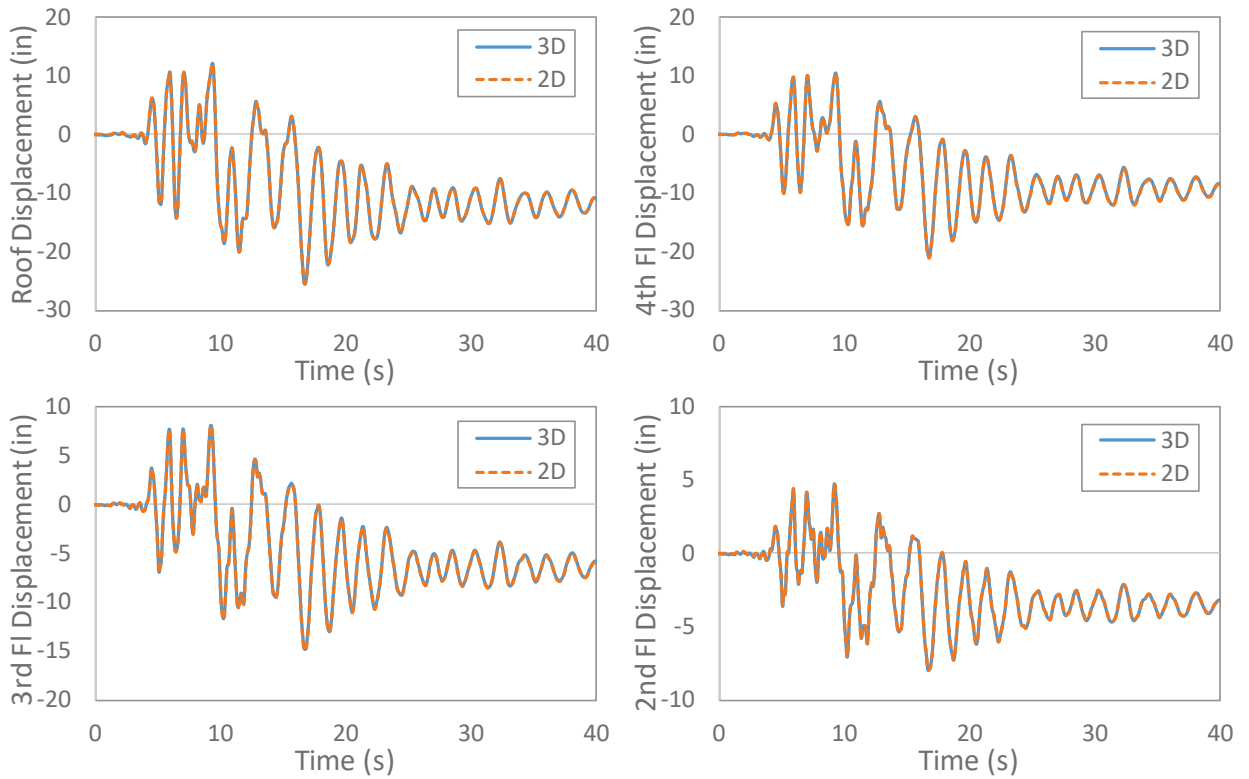


Figure 34. Responses due to 1999 Hector Mine EQ at Hector station, comp 000.

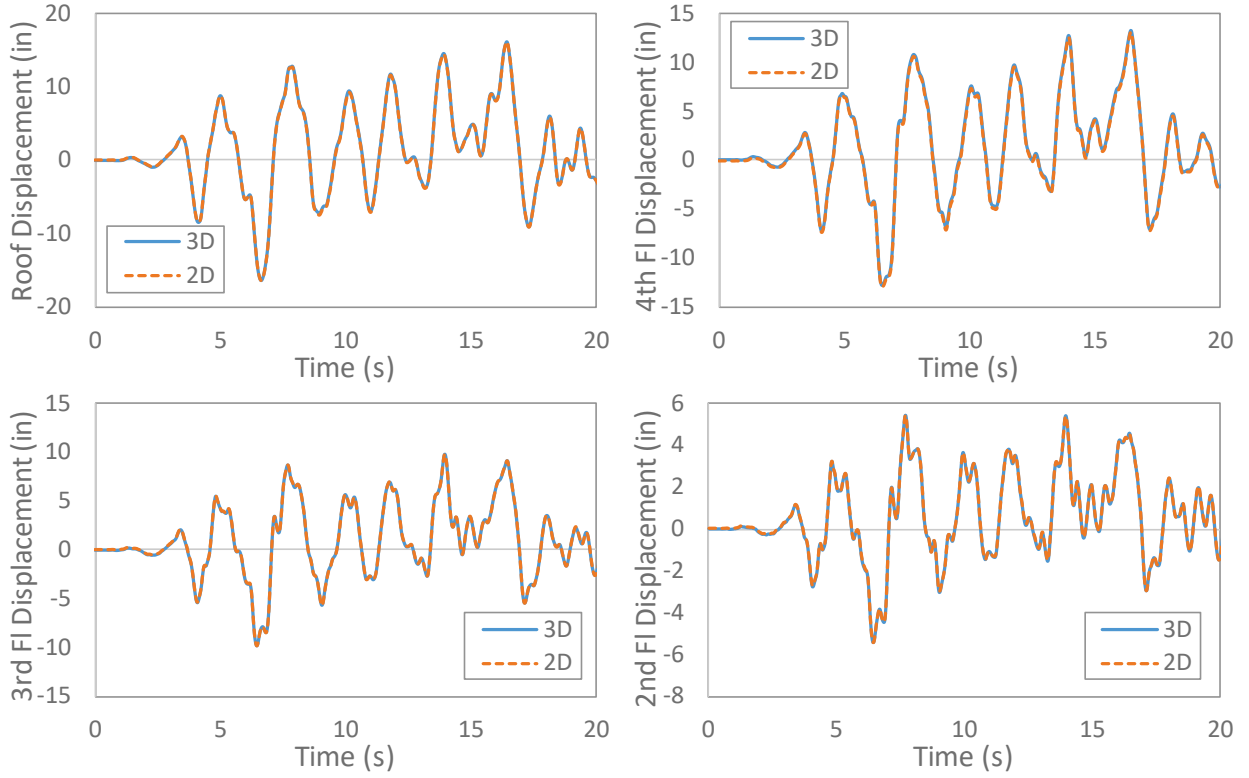


Figure 35. Responses due to 1987 Superstition Hills EQ at Poe Road station, comp 270.

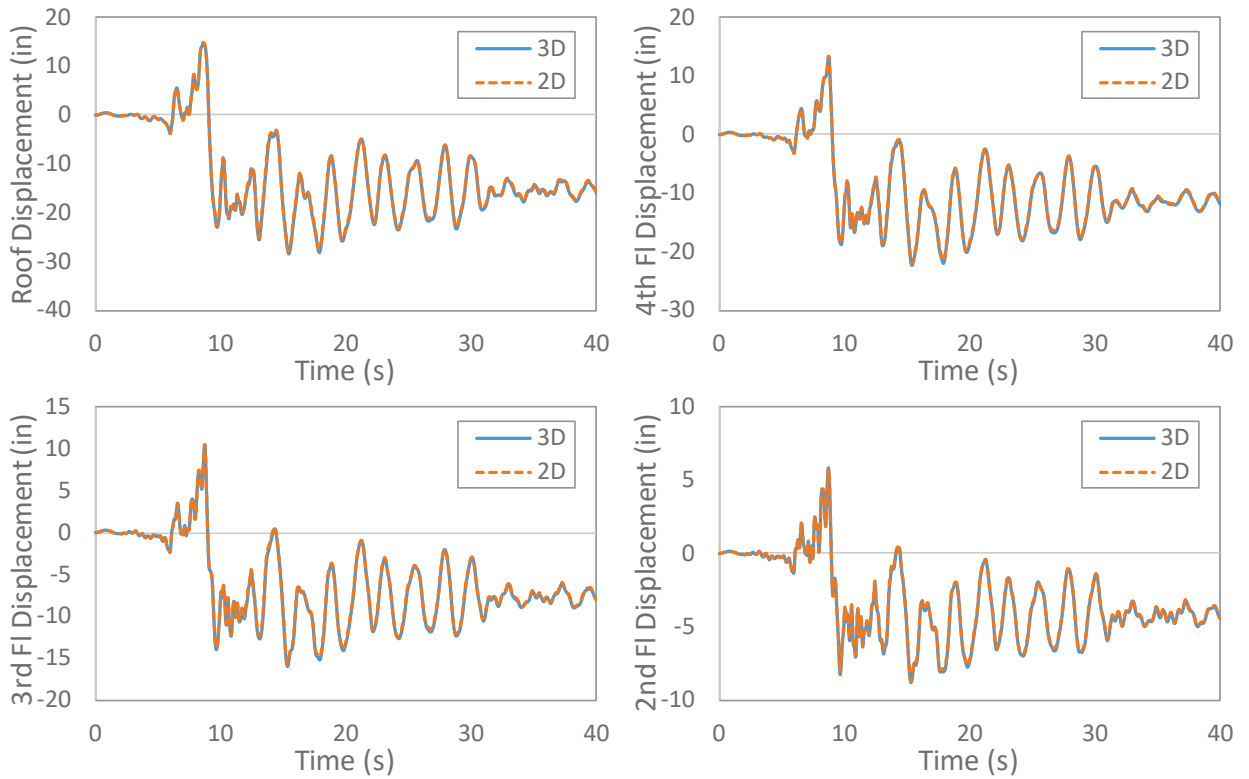


Figure 36. Responses due to 1979 Imperial Valley EQ at El Centro #11, comp 230.

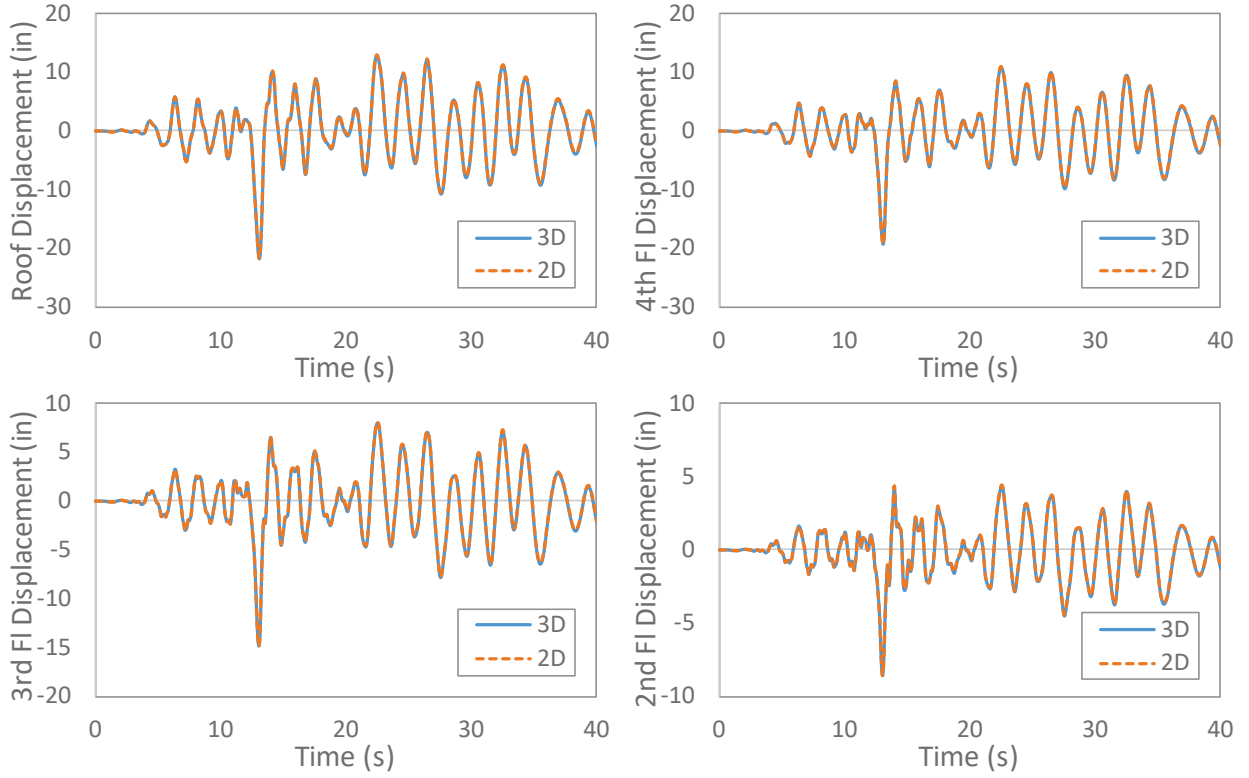


Figure 37. Responses due to 1987 Superstition Hills EQ at El Centro station, comp 000.

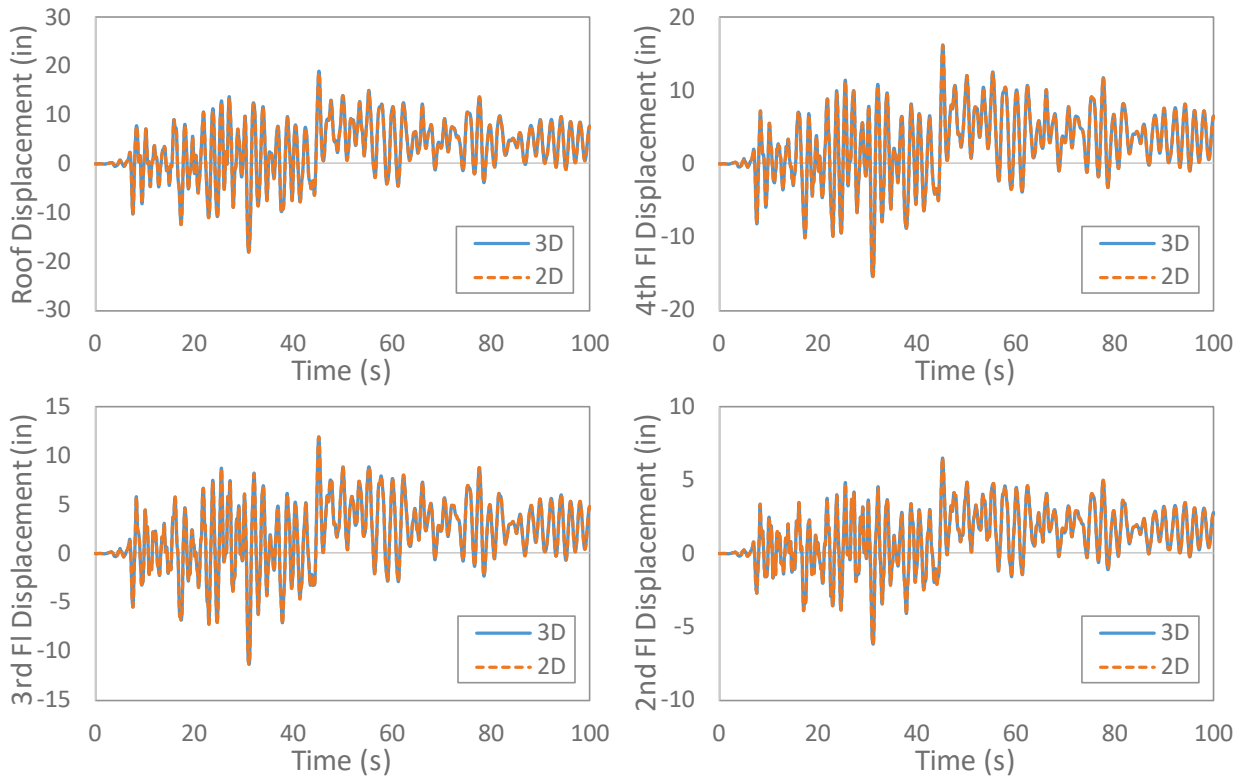


Figure 38. Responses due to 1979 Imperial Valley EQ at Delta station, comp 352.

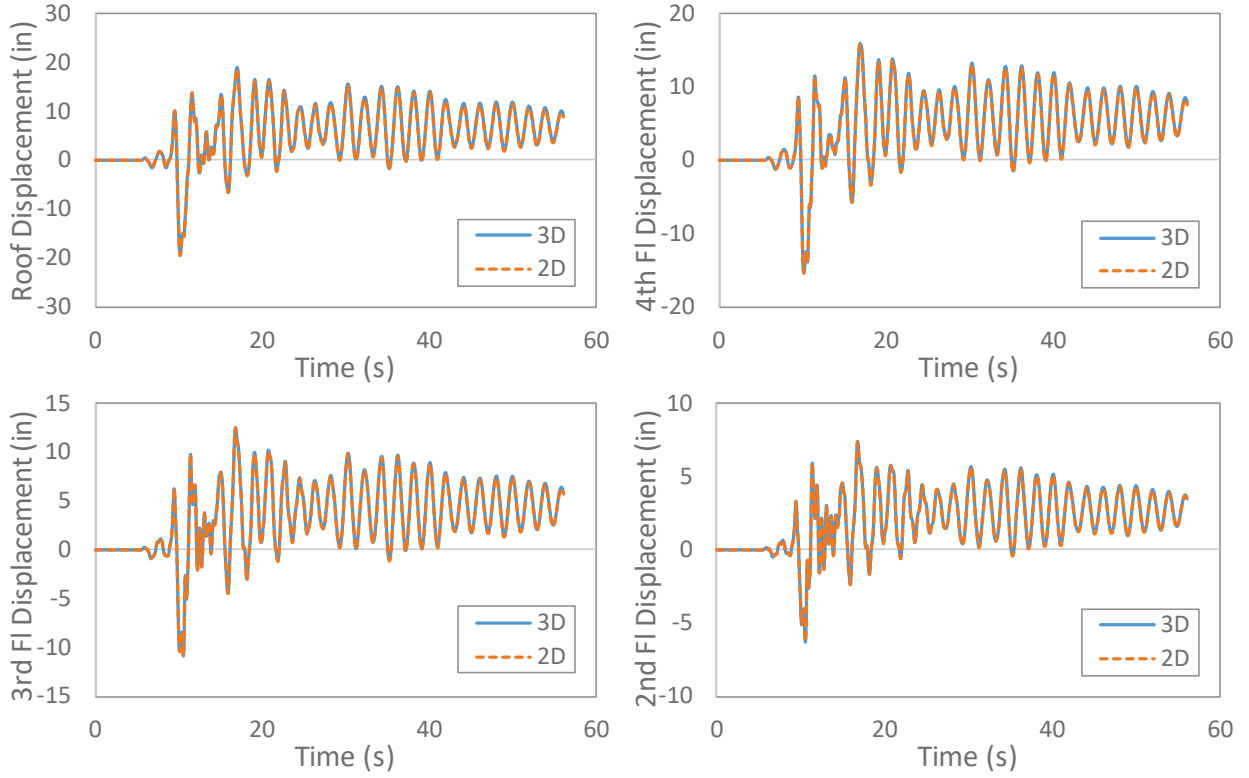


Figure 39. Responses due to 1999 Duzce, Turkey EQ at Bolu station, comp 000.

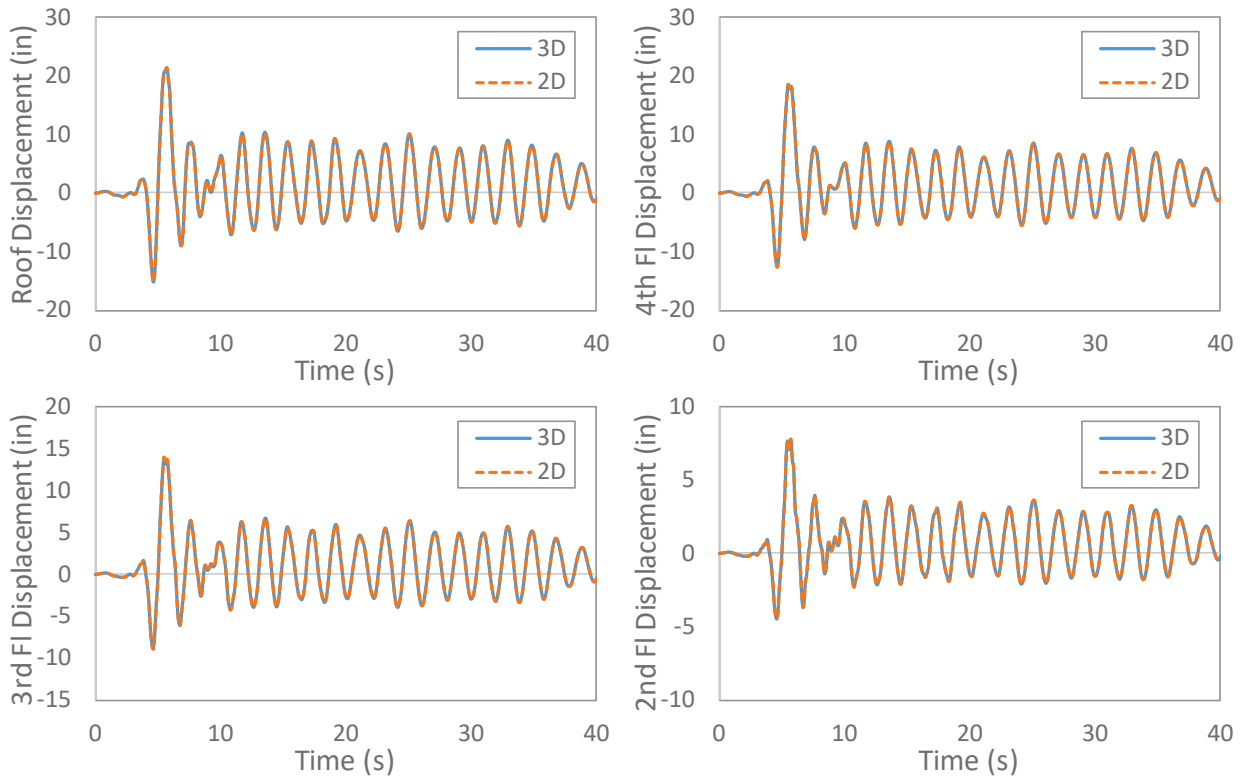


Figure 40. Responses due to 1989 Loma Prieta EQ at Gilroy Array #3, comp 090.

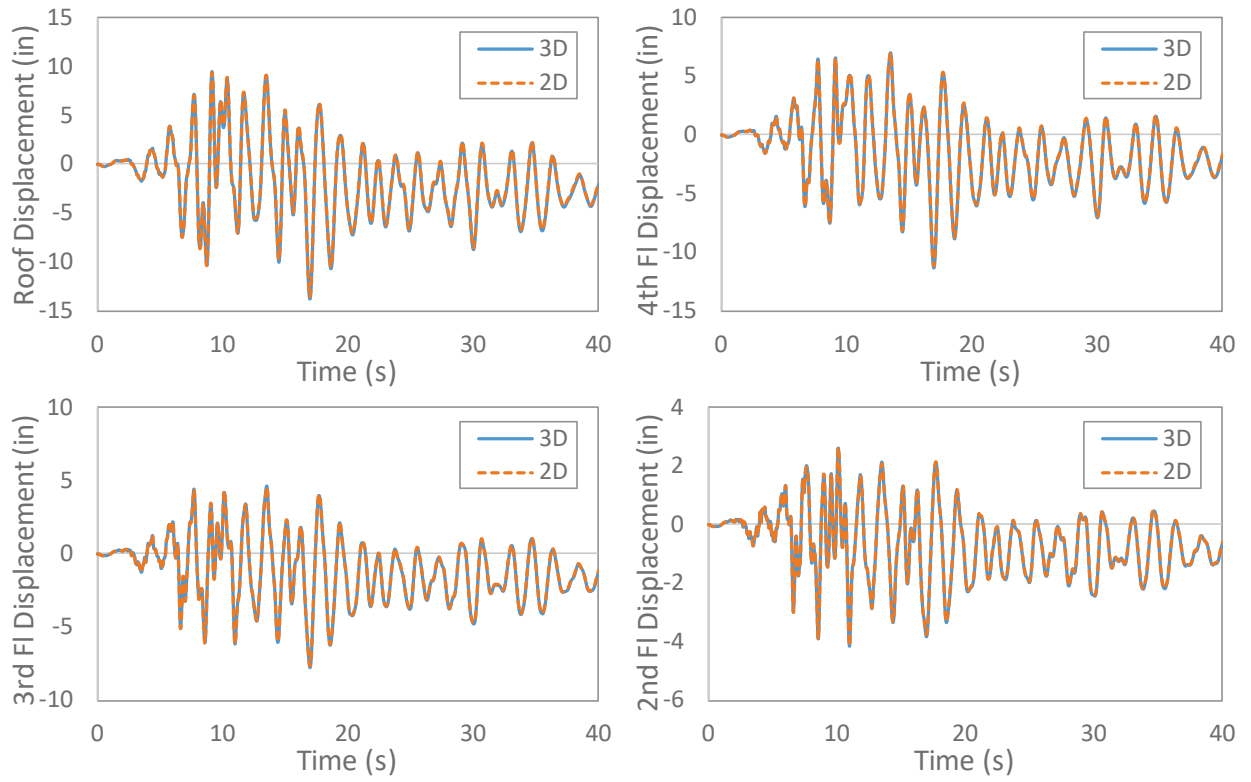


Figure 41. Responses due to 1989 Loma Prieta EQ at Capitola station, comp 090.

Appendix B Comparison of Perform-3D vs OpenSees Models

For the study conducted by Harris and Speicher [3], the Perform-3D software package was used to perform seismic assessment of the buildings. OpenSees is deemed better suited for the purposes of this study and new models were created to carry out the incremental dynamic analysis. To better understand how these models compare, this appendix looks at the differences between the seismic responses of the eight-story RSA-designed building computed based on a Perform-3D model in three-dimensions and an OpenSees model in two-dimensions.

B.1 Differences in Modeling Assumptions

The first difference between the Perform-3D model and the OpenSees model is that three-dimensional (3D) model is created in Perform-3D while two-dimensional (2D) model is created using OpenSees. However, as presented in Appendix A for symmetric buildings, very consistent results between 3D and 2D models can be obtained with careful consideration of the leaning column. Therefore, a similar leaning column is used in the OpenSees 2D model.

The second difference between the Perform-3D model and the OpenSees model is the selection of geometric nonlinearity. Perform-3D only considers of large $P-\Delta$ effect using $P-\Delta$ stiffness, while OpenSees allows for the consideration of both large $P-\Delta$ and small $P-\delta$ effects using corotational stiffness. OpenSees also gives the option to consider only large $P-\Delta$ effect using $P-\Delta$ stiffness. To more accurately capture the nonlinear behavior of the building, the corotational stiffness in OpenSees is selected.

The major difference between the Perform-3D model and the OpenSees model is the selection of the nonlinear behavior to the component hinges. To perform the ASCE 41 assessment, the ASCE 41 backbone curve was used in the Perform-3D model. However, for incremental dynamic analysis where structural collapse and large hinge deformations are expected, a more realistic backbone curve based on ATC 114 is used. As a result, difference is expected between the Perform-3D analysis and the OpenSees analysis after yielding takes place.

B.2 Subassembly Behavior

To illustrate the difference in force-deformation behavior between the OpenSees model (used in this study) and the Perform-3D model (used in [3]), a subassembly model was created in both platforms as shown in Figure 42. Doubly-symmetric bending was assumed for both the beams and columns, thus zero moment at the mid-spans. As shown in Figure 43, assuming the columns remain elastic, the (a) total drift can be broken down into the following actions: (b) elastic deformation of the beams and columns, (c) inelastic behavior of the beam hinges, and (b) joint panel zone deformation. The results of a displacement-controlled reversed cyclic simulation are shown in Figure 44. The member properties and RBS hinge properties are those of the 4-story ELF design at the second-floor interior column.

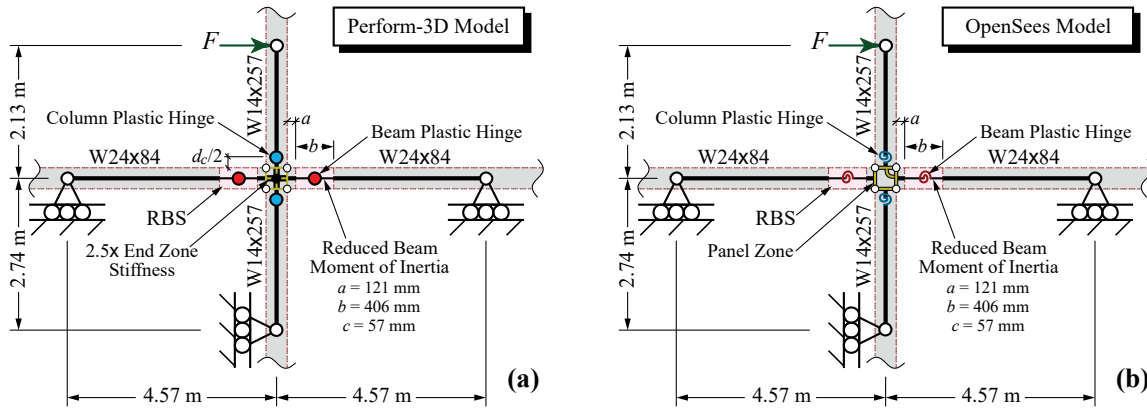


Figure 42. Subassembly models used to compare (a) Perform-3D and (b) OpenSees.

The force-displacement behavior reasonably matches for drift levels up to approximately 5 %. Beyond this level, the Perform-3D model loses all strength and the response travels along the zero-force level. The Perform-3D model's force-deformation curve was created using the default a , b and c parameters given in ASCE 41-06 Table 5-6 [6]. The endzone stiffness parameter used in Perform-3D was set to 2.5, which accounts for a portion the stiffness differences between the two models. Perform-3D also includes elastic shear deformations and the OpenSees model does not, which contributes to the stiffness difference.

Note that the Perform-3D force-displacement response at the top of the subassembly has a sudden post-capping strength decrease due to the RBS hinge (even though the RBS inelastic spring has a more gradual decrease). This can be explained by examining the drift contributions as conceptually illustrated in Figure 45. At step k , the force is shown reaching the capping (peak) level. Once the strength starts to drop on the subassembly, say at step $k+1$, the remaining elastic elements have a reduced contribution to the drift thus the effective drop is sudden. Note, displacement Δ_{k+1} is only assumed slightly larger than Δ_k , though Fig. 5 shows this exaggerated. Figure 44 shows the actual behavior for the Perform-3D model with the sudden drop.

In contrast, the OpenSees subassembly model has a gradual post-capping strength deterioration behavior. Lignos and Krawinkler [33] reported that the slope of this degradation is one of the most important parameters that influences the nonlinear response. The slope is established by θ_{pc} . This descending branch continues until the force-deformation reaches the residual strength or the ultimate rotation. For this paper, θ_u was taken as 0.20 radians for all

hinges. Lignos and Krawinkler [22] reported θ_u values of approximately 0.07 radians for fully-reversed cyclic tests, but monotonic tests may be up to 3 times larger. The residual strength factor, κ , was taken as 0.4, which is double the value given in ASCE 41 and used in Harris and Speicher [3]. Note, the values of θ_u and κ have been reported to be non-critical in studies where collapse capacities are being determined [22].

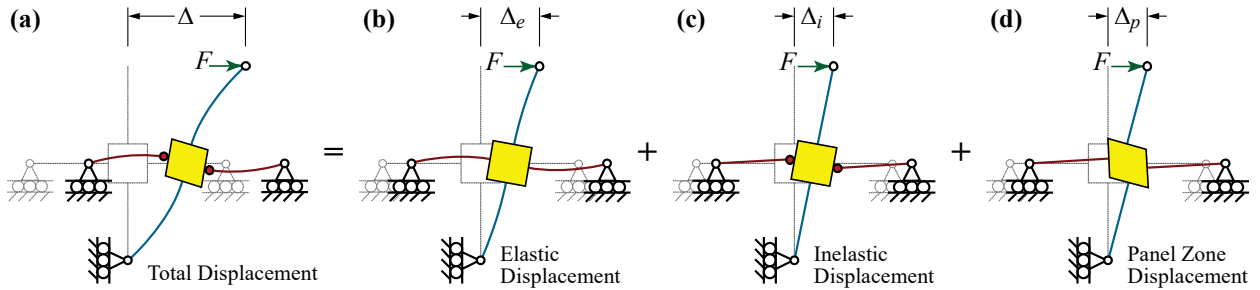


Figure 43. Drift contributions for a moment frame subassembly.

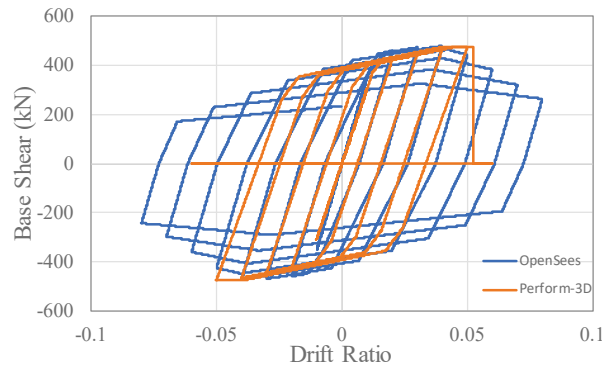


Figure 44. Comparison of the response of subassembly to cyclic loading for OpenSees and Perform-3D (model used in [3]).

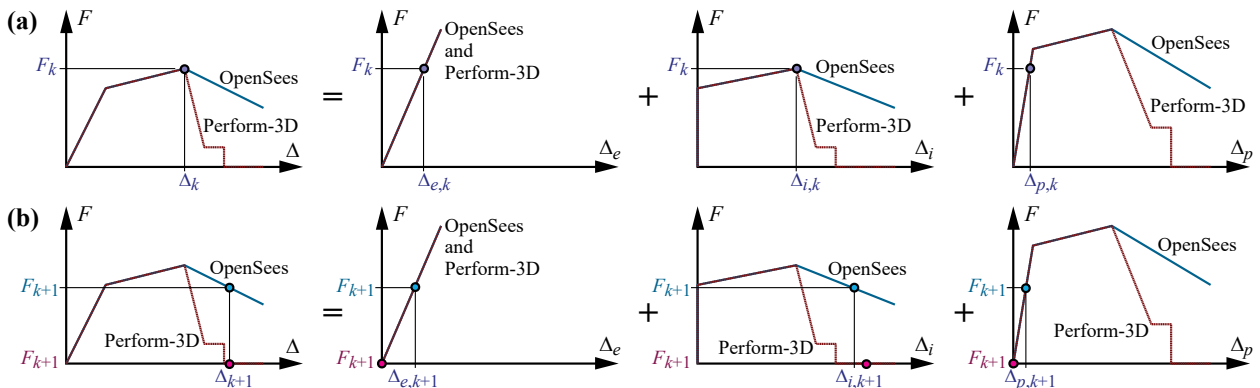


Figure 45. Explanation of drift between (a) some point, k , at the capping moment and (b) some point, $k+1$, just beyond the capping moment.

B.3 Comparison of Responses Using the 8-story RSA Frame

The OpenSees model of the 8-story RSA-designed building is developed in 2D with a leaning column and detailed modeling of the panel zones. This 2D OpenSees model, together with the 3D Perform-3D model, are subjected to the following two earthquake ground motion records:

- 1995 Kobe earthquake at Nishi-Akashi station, component 090, normalized and MCE-adjusted by an amplification factor of 3.0111.
- 1994 Northridge earthquake at Mulholland Drive station, component 009, normalized and MCE-adjusted by an amplification factor of 1.8998.

An additional scale factor is then applied to magnify each earthquake to cause the building to experience large displacement and collapse. Figure 46 to Figure 51 compare the displacement responses of each floor. In all figures in this section, P3D (solid blue line) denotes the results from Perform-3D and OPS (dashed orange line) denotes the results from OpenSees.

Figure 46, Figure 47, and Figure 48 compare the responses due to the 1995 Kobe earthquake with scale factors of 1.3, 1.4, and 1.5, respectively. The responses are initially consistent between the two models, indicating that the two models have the same elastic properties. However, the response deviate once the frame yields and nonlinear response occurs. As shown in Figure 46, there is a permanent offset between the responses of the models, which can be largely attributed to the difference in nonlinear hinge properties. Figure 47 shows that collapse occurs for the Perform-3D model at a scale factor of 1.4, but collapse does not occur in the OpenSees model until a scale factor of 1.5 as shown in Figure 48. If collapse is a concern, the Perform-3D model can be considered slightly more conservative in this case.

Similar observations are made from Figure 49, Figure 50, and Figure 51 due to the 1994 Northridge earthquake with scale factors of 1.5, 1.6, and 2.4, respectively. Again, consistent results are obtained during initial shaking between the two models, but the results begin to deviate once the frame yields. Figure 50 shows that for the Perform-3D model collapse occurs at a scale factor of 1.6. However, the OpenSees model does not collapse until a scale factor of 2.4, indicating that there can be significant differences in the scale factor to cause collapse when different nonlinear hinge models are used. These observations should be kept in mind when comparing the study by Harris and Speicher [3] to the results of a FEMA P695 assessment. Given the inherent uncertainties in nonlinear response history analysis, the general agreement of the responses is, none-the-less, considered reasonable.

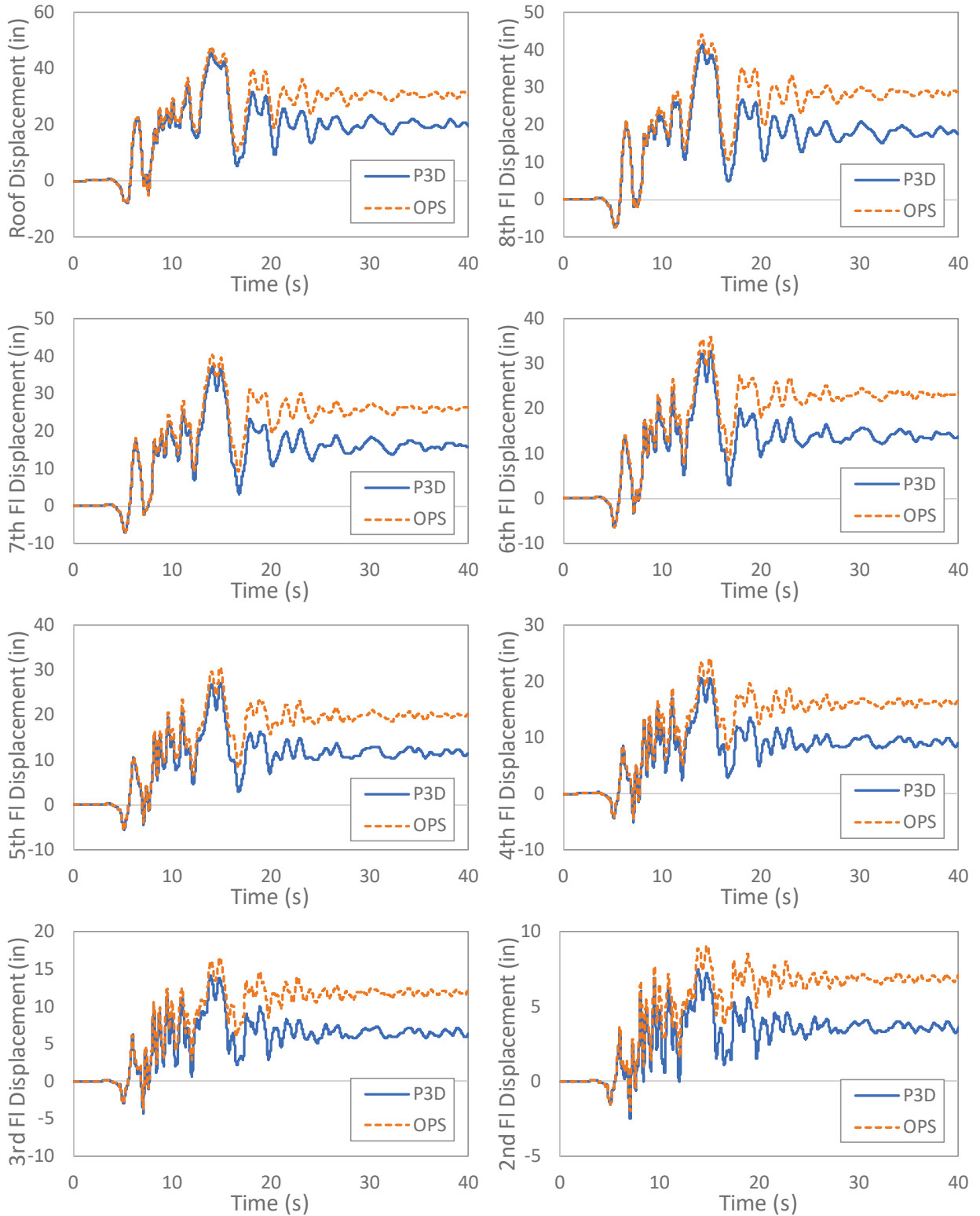


Figure 46. Comparison of floor displacement responses due to 1995 Kobe earthquake at Nishi-Akashi station, component 090, magnified by a scale factor of 1.3.

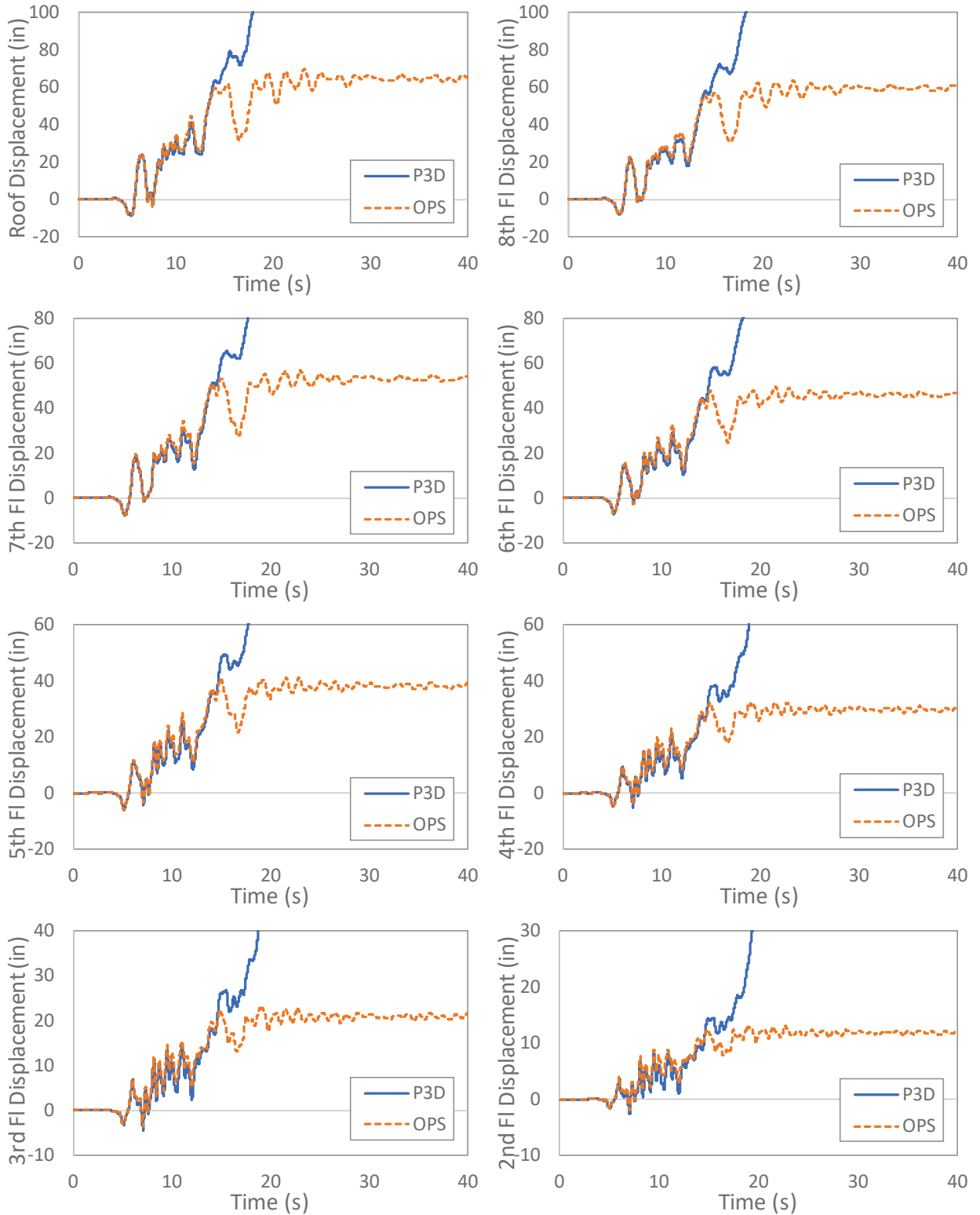


Figure 47. Comparison of floor displacement responses due to 1995 Kobe earthquake at Nishi-Akashi station, component 090, magnified by a scale factor of 1.4.

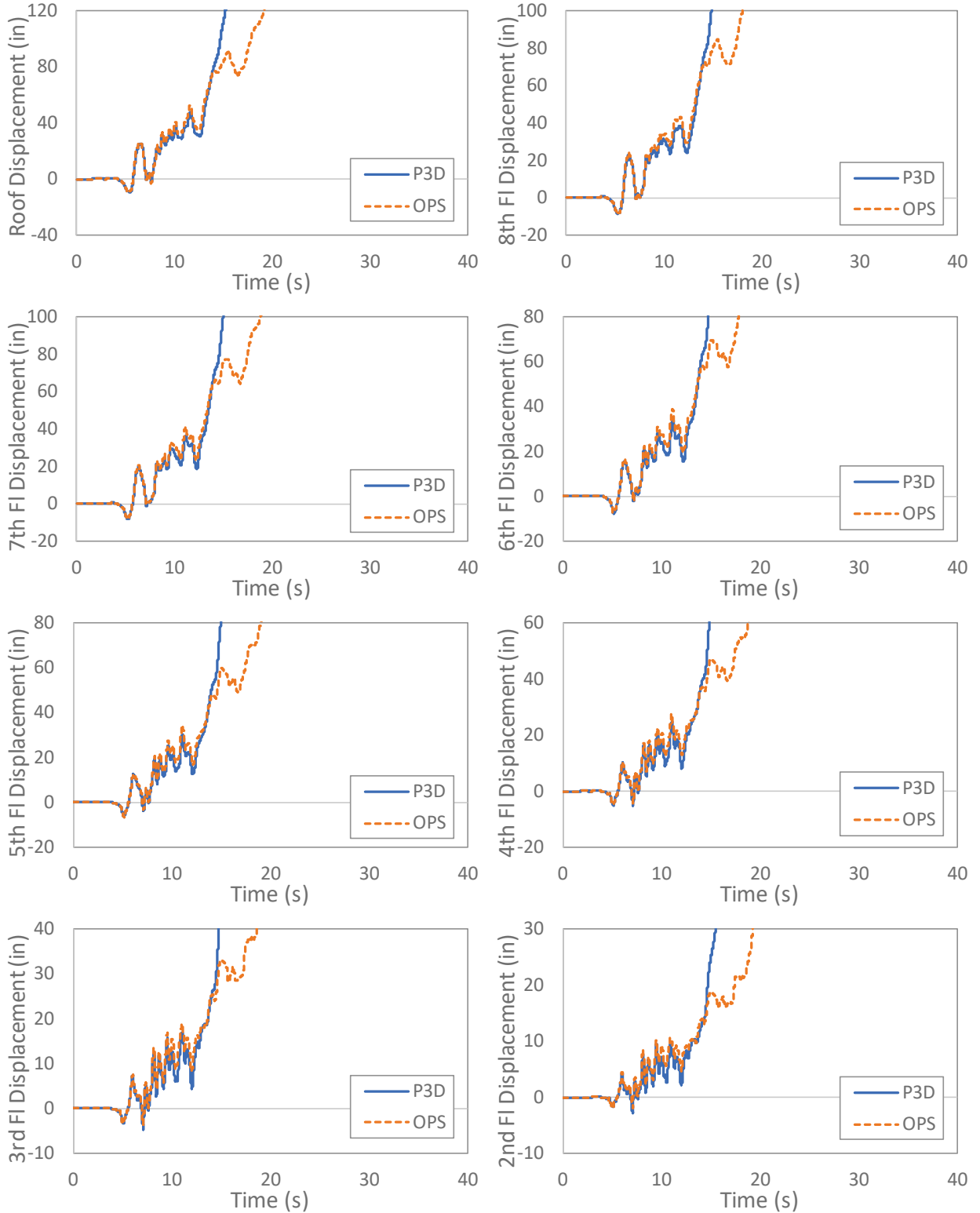


Figure 48. Comparison of floor displacement responses due to 1995 Kobe earthquake at Nishi-Akashi station, component 090, magnified by a scale factor of 1.5.

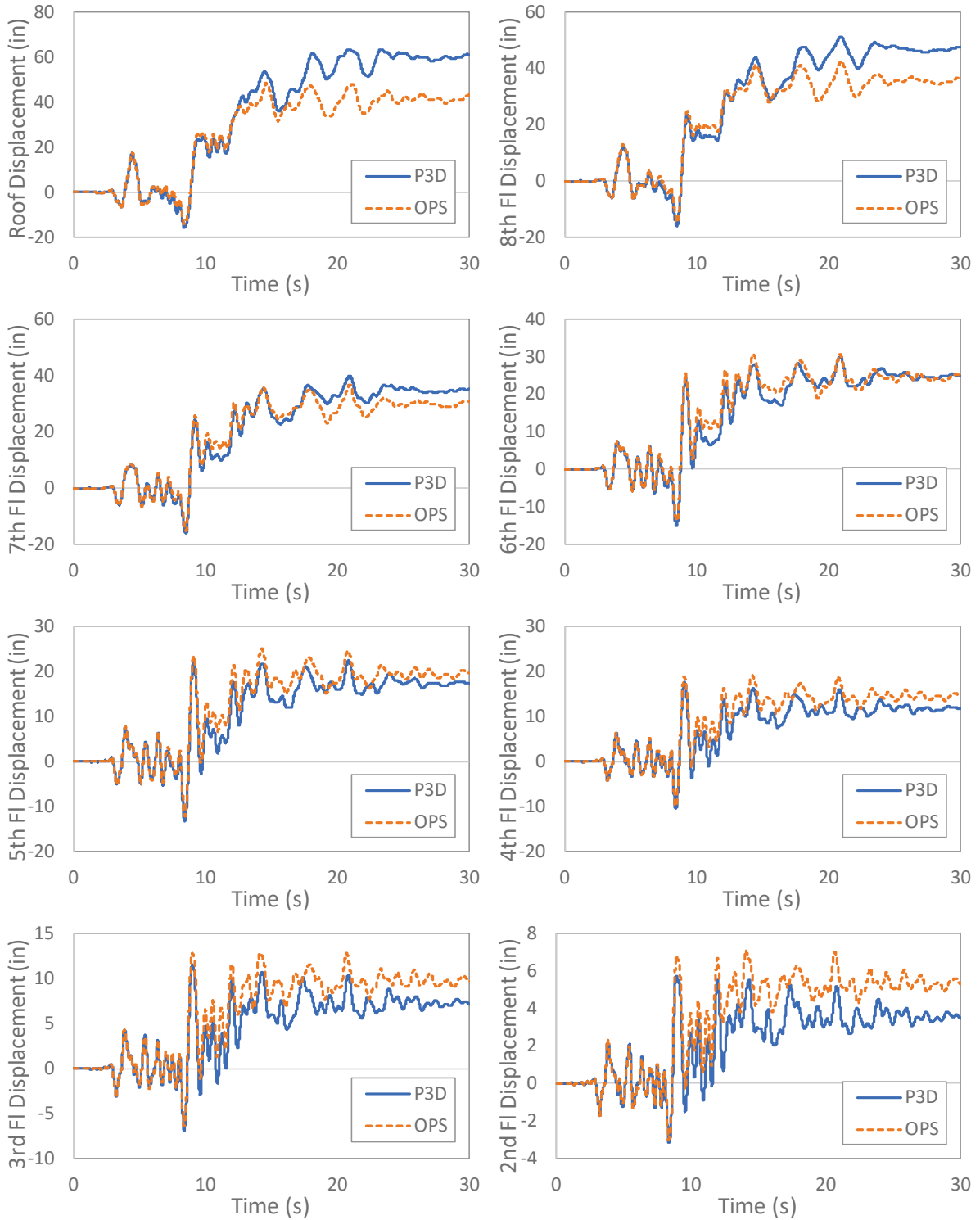


Figure 49. Comparison of floor displacement responses due to 1994 Northridge earthquake at Mulholland Drive station, component 009, magnified by a scale factor of 1.5.

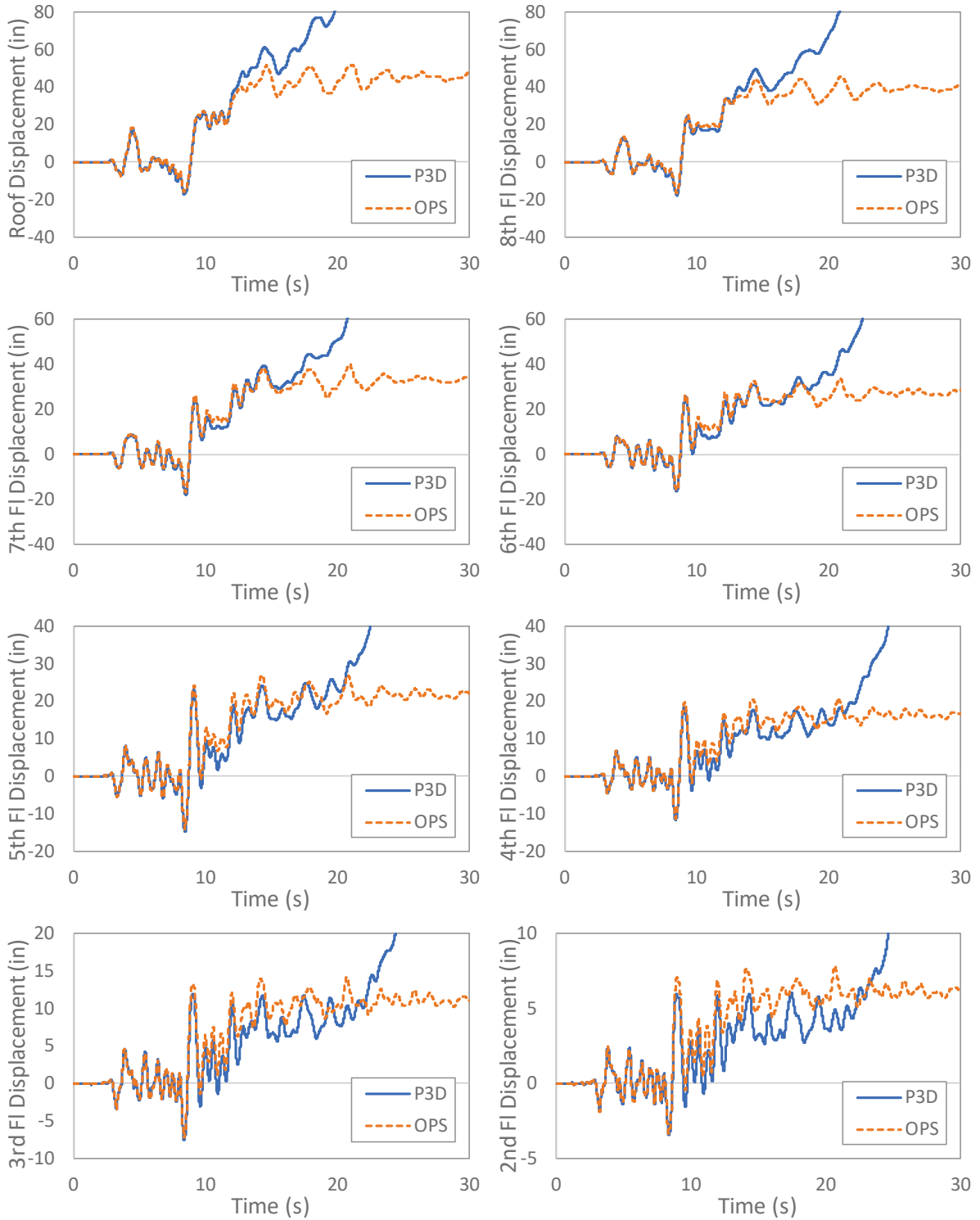


Figure 50. Comparison of floor displacement responses due to 1994 Northridge earthquake at Mulholland Drive station, component 009, magnified by a scale factor of 1.6.

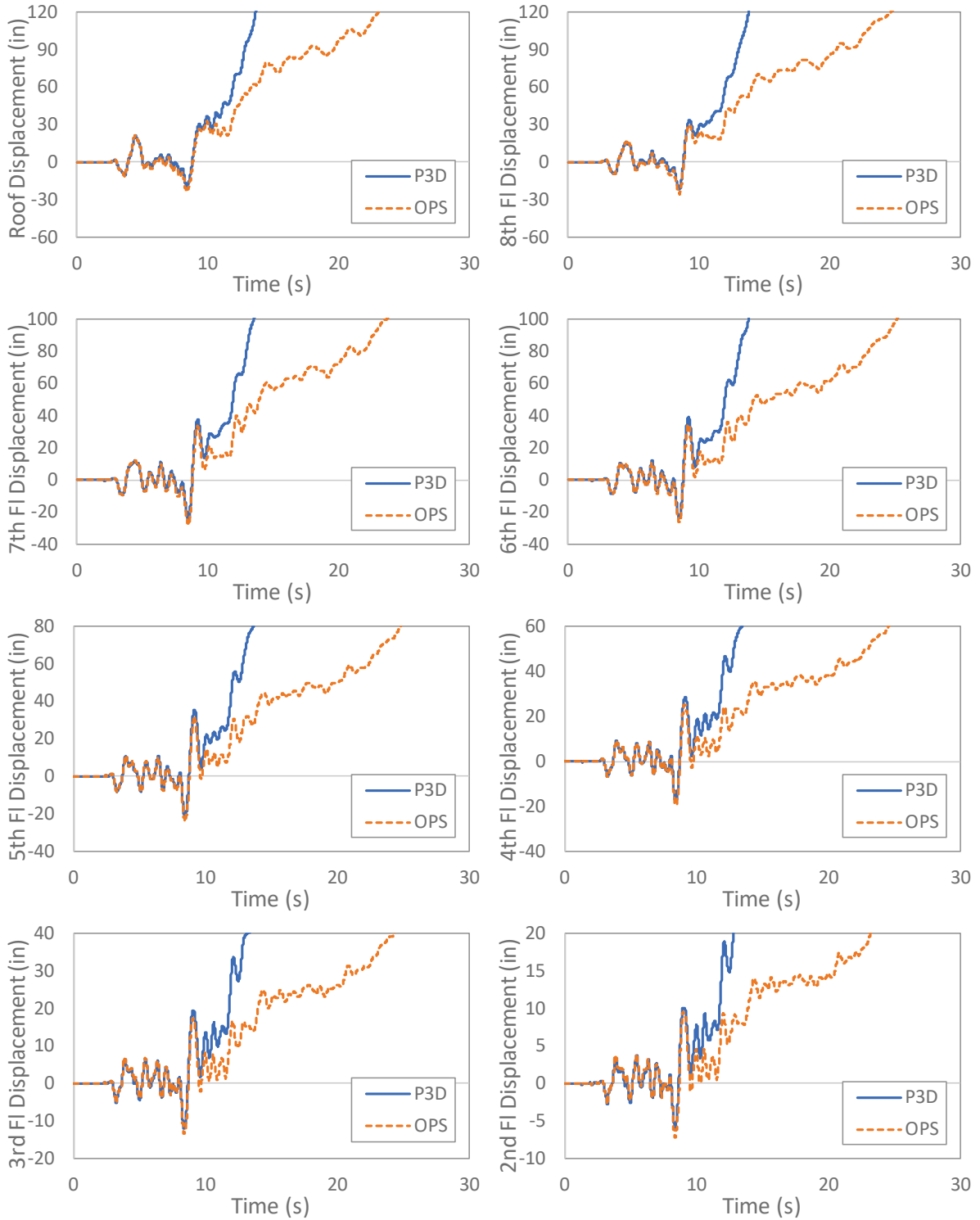


Figure 51. Comparison of floor displacement responses due to 1994 Northridge earthquake at Mulholland Drive station, component 009, magnified by a scale factor of 2.4.

Appendix C Nonlinear Hinge Modeling

This appendix gives the details of the modeling approach taken for each type of nonlinear hinge component. This appendix also includes a validation for each component to demonstrate the behavior.

C.1 General Modeling Approach

C.1.1 RBS Hinge

OpenSees can capture cyclic and in-cycle degradation using the modified Ibarra Medina Krawinkler (IMK) model with the Bilin material. The force-deformation parameters, defined below, for the RBS followed the recommendations made by Lignos and Krawinkler [22], which were derived using multivariate regression analysis of a suite of experimental results. These parameters include the plastic rotation capacity, θ_p , the post-capping rotation capacity, θ_{pc} , the yield strength, M_y , the capping strength, M_c , the ultimate rotation, θ_u , the residual strength ratio, κ , and the reference cumulative plastic rotation parameter, Λ . The parameters are shown graphically in Figure 52. For the strength parameters, the formulas are as follows:

$$M_y = 1.1(M_{pe}) = 1.1(ZR_y F_y) \quad (6)$$

$$M_c = 1.1(M_y) \quad (7)$$

where M_{pe} is the expected plastic moment, Z is the plastic section modulus, R_y is the material overstrength factor, and F_y is the expected yield strength. For the other parameters, the formulas are as follows:

$$\theta_p = 0.19 \left(\frac{h}{t_w} \right)^{-0.314} \left(\frac{b_f}{2 \cdot t_f} \right)^{-0.100} \left(\frac{L_b}{r_y} \right)^{-0.185} \left(\frac{L}{d} \right)^{0.113} \left(\frac{c_{unit}^1 \cdot d}{533} \right)^{-0.760} \left(\frac{c_{unit}^2 \cdot F_y}{355} \right)^{-0.070} \quad (8)$$

$$\theta_{pc} = 9.52 \left(\frac{h}{t_w} \right)^{-0.513} \left(\frac{b_f}{2t_f} \right)^{-0.863} \left(\frac{L_b}{r_y} \right)^{-0.108} \left(\frac{c_{unit}^2 F_y}{355} \right)^{-0.360} \quad (9)$$

$$\Lambda = \frac{E_t}{M_y} = 585 \left(\frac{h}{t_w} \right)^{-1.14} \left(\frac{b_f}{2t_f} \right)^{-0.632} \left(\frac{L_b}{r_y} \right)^{-0.205} \left(\frac{c_{unit}^2 F_y}{355} \right)^{-0.391} \quad (10)$$

where h/t_w is the web depth-to-thickness ratio, $b_f/2t_f$ is the flange width-to-thickness ratio, L/d is the clear span-to-depth ratio, and d is the section depth. Additionally, c_{unit}^1 and c_{unit}^2 are unit conversion coefficients equal to 1.0 if millimeters and newtons are used and 25.4 and 6.895 if inches and kips are used, respectively. The residual strength ratio, κ , is taken as 0.4. Note, these equations are very similar to the updated formulas given in the ATC 114 report [19] for monotonic backbone curves.

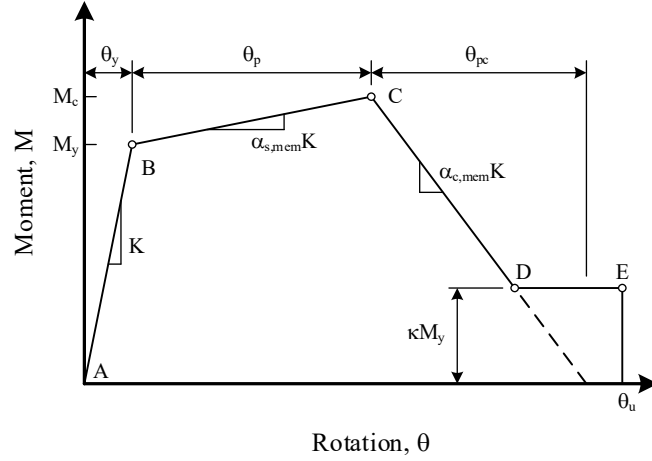


Figure 52. Generic member backbone curve with basic input parameters.

C.1.2 Column Hinge

Like the RBS hinges, the column hinges use the modified IMK model with Bilin material. In contrast to the RBS parameters, the predictive equations used for the column hinge parameters come from NIST [19]. Also, the column moment strengths are reduced based on the axial compressive load due to gravity, P_g , per NIST [19].

The formula for the yield moment strengths is as follows:

$$\text{If } \begin{cases} P_g / P_{ye} \leq 0.20 & M_y^* = 1.15ZR_yF_y(1 - P_g / P_{ye}) \\ P_g / P_{ye} > 0.20' & M_y^* = 1.15ZR_yF_y \left[9/8(1 - P_g / P_{ye}) \right] \end{cases} \quad (11)$$

where P_g is the axial compression force due to gravity loads, P_{ye} is the expected yield strength of the column, and all other terms have been defined previously. The 1.15 factor accounts for cyclic hardening. The formula for the peak flexural strength, M_p , is as follows:

$$M_p = aM_y^* \quad (12)$$

The coefficient a depends on previously defined parameters as follows:

$$a = 12.5 \left(\frac{h}{t_w} \right)^{-0.2} \left(\frac{L_b}{r_y} \right)^{-0.4} \left(1 - \frac{P_g}{P_{ye}} \right)^{1.6} \geq 1.0 \text{ and } \leq 1.3 \quad (13)$$

The residual strength, M_r , is also a function of the gravity load and can be calculated as follows:

$$M_r = \left(0.5 - 0.4 \frac{P_g}{P_{ye}} \right) M_y^* \quad (14)$$

Since degradation is captured in the IMK model, the monotonic backbone curve equations are chosen, and the associated deformation parameters are as follows:

$$\theta_p = 294 \left(\frac{h}{t_w} \right)^{-1.7} \left(\frac{L_b}{r_y} \right)^{-0.7} \left(1 - \frac{P_g}{P_{ye}} \right)^{1.6} \leq 0.20 \quad (15)$$

$$\theta_{pc} = 90 \left(\frac{h}{t_w} \right)^{-0.8} \left(\frac{L_b}{r_y} \right)^{-0.8} \left(1 - \frac{P_g}{P_{ye}} \right)^{2.5} \leq 0.30 \quad (16)$$

where h/t_w is the web depth-to-thickness ratio, L_b/r_y is the unbraced length divided by the radius of gyration about the y-axis of the cross-section, clear span-to-depth ratio, P_g/P_{ye} is the axial gravity load capacity divided by the expected axial yield load.

Since NIST [19] does not provide deterioration values, Λ , Lignos and Krawinkler (2011) is used for this value as is done in the RBS hinge calculations.

C.1.3 Panel Zone Hinge

The panel zones are modeled using four “rigid” elements connected by pins and a rotation spring as illustrated in Figure 54. This model is a monotonic shear force versus shear deformation relationship proposed by Krawinkler [23]. All panel zone elements are given an area of 1000 in² and moment of inertia of 100,000 in⁴. The panel zone spring strength and stiffness is calculated using equations given in Gupta and Krawinkler [34] as summarized below. First, the yield strength of the panel zone, V_y , is calculated as:

$$V_y = 0.95 d_c t_p \frac{F_y}{\sqrt{3}} \approx 0.55 F_y d_c t_p \quad (17)$$

where d_c is the column depth, t_p is the thickness of the panel zone, and F_y is the material yield stress. Next, the panel zone yield angle, γ_y , is given as:

$$\gamma_y = \frac{F_y}{G\sqrt{3}} \quad (18)$$

where the shear modulus, G , calculated as:

$$G = \frac{E}{2(1+0.3)} \quad (19)$$

The elastic shear stiffness, K_e , of the panel zone can then be taken as:

$$K_e = \frac{V_y}{\gamma_y} = 0.95 d_c t_p G \quad (20)$$

and post-yield stiffness, K_p , of the panel zone can be taken as:

$$K_p = 0.95 G b_{cf} t_{cf} 2/d_b \quad (21)$$

where b_{cf} is the depth column flange, t_{cf} is the width column flange, and d_b is the depth of the beam.

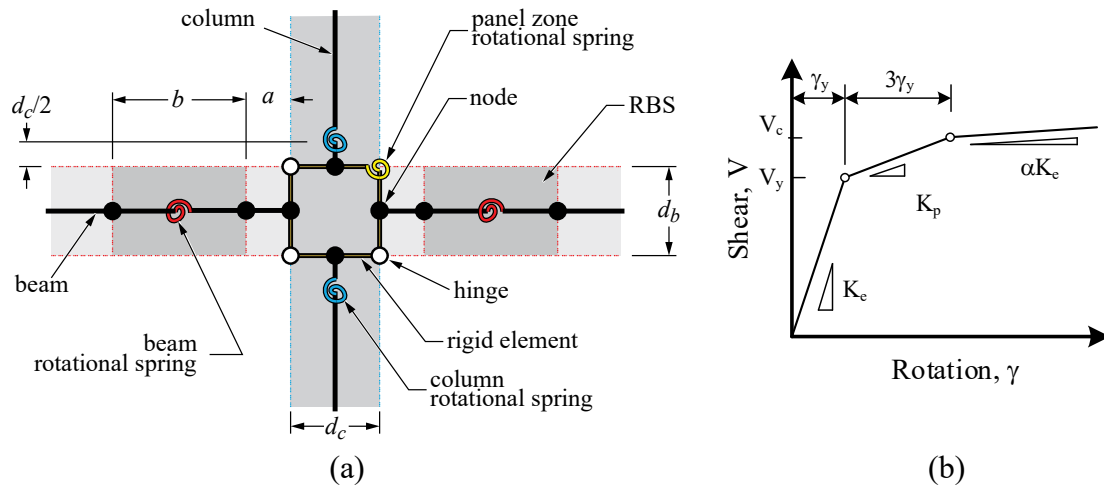


Figure 53. (a) Analytical model for the beam-to-column connection elements (panel zone, beam hinge, and column hinge) and (b) generic panel zone force-deformation backbone curve.

C.2 Model Validation

A model validation is presented to verify the output matches what is expected from the input and give the reader clear insight into the approach taken in this study. The parameters for the nonlinear beam and column hinges are calculated as shown previously. The backbone curves are based on the monotonic behavior because degradation is captured using the OpenSees Bilinear material model. A generic backbone curve is shown in Figure 52, where θ_p , θ_{pc} , θ_u , M_y , M_c , K , and κ completely define the behavior. This backbone curve is assumed to be that of the member (extending from plastic hinge to plastic hinge, but exclusive of these hinges). Therefore, to properly input into OpenSees, θ_p and θ_{pc} must be modified (θ_p is decreased and θ_{pc} is increased) because the hinge spring is given initial flexibility (i.e., $K_s = nK_{bc}$). This is done because if the hinge spring is made rigid, numerical issues arise in the solution algorithm. In this report, we set n equal to 10 as recommended by others (Ibarra, 2005).

C.2.1 RBS Hinge

Table 13 shows the parameters calculated using the predictive equations in the above (member) and the associated modified parameters due to the flexibility of the hinge spring. Table 14 shows the stiffness, K , the strain-hardening stiffness ratio, α_s , and the post-capping stiffness ratio, α_c , of the member, hinge, and beam-column. Note, the modified parameters converge to the initial parameters as n approached infinity (i.e., the hinge is rigid initially). Also, recall that the stiffness of the member is calculated by considering the hinge and the beam-column as springs in series. The stiffness of the beam member is calculated considering the reduced section placed over the length of the RBS by using the Moment-Area Method. See for Appendix B.3 detailed calculations.

The resulting backbone curves for the left hinge at each story of bay 2 in the 8-story RSA-designed building is plotted in Figure 54. Analysis results of EQ 1 with a scale factor of 2.0 (record first normalized and anchor scaled – see Appendix F) are plotted with the backbone curve to verify the behavior. For this example, beam hinge yielding happens at all floors, with maximum rotations of approximately 0.07 radians. The backbone curves and the analysis results correspond as expected.

Table 13. Nonlinear RBS hinge properties for bay 2 of the 8-story RSA-designed frame: strength and rotation.

Floor	Member				Hinge				
	M_y kip-ft	M_c kip-ft	θ_p rad $\times 10^3$	θ_{pc} rad $\times 10^3$	θ_p rad $\times 10^3$	θ_{pc} rad $\times 10^3$	θ_u rad $\times 10^3$	Λ	κ
9	320	352	27.9	149	27.1	158	150	0.82	0.4
8	274	302	27.8	149	27.2	157	150	0.82	0.4
7	411	452	25.1	154	24.4	161	150	0.83	0.4
6	411	452	25.1	154	24.4	161	150	0.83	0.4
5	650	715	27.5	177	26.9	184	150	1.05	0.4
4	650	715	27.5	177	26.9	184	150	1.05	0.4
3	722	794	28.3	203	27.7	210	150	1.22	0.4
2	722	794	28.3	203	27.7	210	150	1.22	0.4

Table 14. Nonlinear RBS properties for bay 2 of the 8-story RSA-designed frame: stiffness.

Floor	Member			Hinge			Beam-Column
	K kip-ft $\times 10^{-3}$ / rad	α_s $\times 10^3$	α_c $\times 10^3$	K kip-ft $\times 10^{-3}$ / rad	α_s $\times 10^3$	α_c $\times 10^3$	K kip-ft $\times 10^{-3}$ / rad
9	5,331	31.0	-63.7	58,643	2.90	-5.48	5,864
8	5,270	26.9	-55.2	57,967	2.51	-4.78	5,797
7	8,519	27.7	-49.6	93,714	2.59	-4.32	9,371
6	8,519	27.7	-49.6	93,714	2.59	-4.32	9,371
5	13,393	25.4	-43.6	147,318	2.36	-3.81	14,732
4	13,393	25.4	-43.6	147,318	2.36	-3.81	14,732
3	15,104	24.3	-37.3	166,146	2.26	-3.28	16,615
2	15,104	24.3	-37.3	166,146	2.26	-3.28	16,615

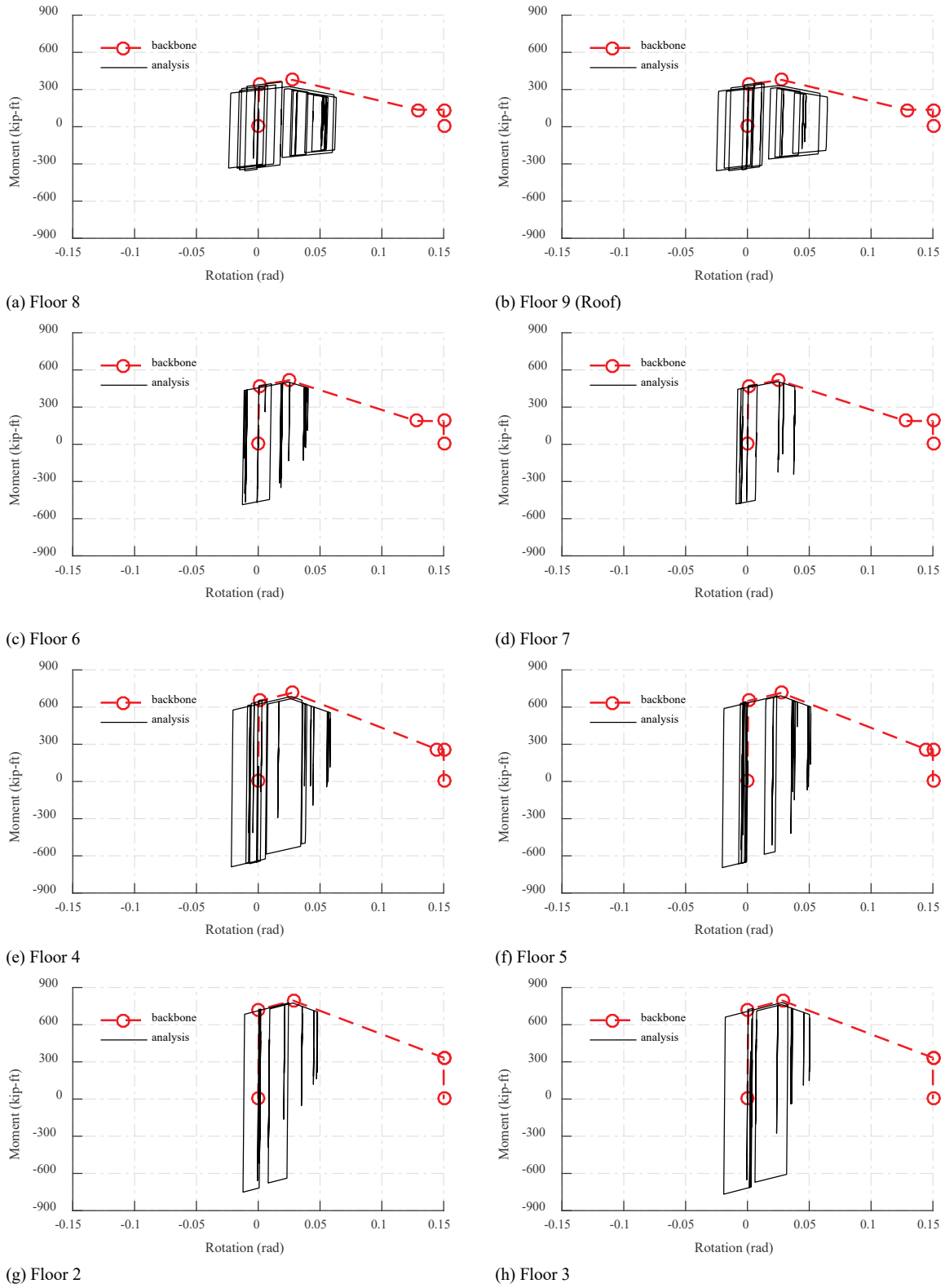


Figure 54. RBS hinge backbone curves and select analysis results for the left hinge in bay 2 of the 8-story RSA-designed building (EQ 1, $sf = 2.0$).

C.2.2 Column Hinge

Table 15 shows the parameters calculated using the predictive equations in NIST [19]. In contrast to the beam RBS moment strengths, the column moment strengths are reduced based on the axial compressive load due to gravity, P_g . Since NIST [19] does not provide deterioration values, Λ , Lignos and Krawinkler [22] is used for this value as is done in the beam calculations. Table 16 shows the stiffness, K , the strain-hardening stiffness ratio, α_s , and the post-capping stiffness ratio, α_c , of the member, hinge, and beam-column. The column is assumed to be in double curvature bending therefore the stiffness (rotational) from hinge-to-hinge is $6EI/L_{hh}$, where L_{hh} is the length from hinge-to-hinge.

The resulting backbone curves for the lower hinge at each story of pier 2 in the 8-story RSA-designed building is plotted in Figure 54. Analysis results of EQ 1 with a scale factor of 2.0 (record first normalized and anchor scaled – see Appendix F) are plotted with the backbone curve to verify the behavior. For this example, column hinge yielding happens only at the base and at story 7 – most of the yielding is found in the beam hinges and panel zones. The backbone curves and the analysis results match as expected.

Table 15. Nonlinear column properties for lower hinge of each story in pier 2 of the 8-story RSA-designed frame: strength and rotation.

Floor	Member					Hinge Spring				
	P_g/P_y	M_y^a kip-ft	M_c^b kip-ft	θ_p rad × 10 ³	θ_{pc} rad × 10 ³	θ_p rad × 10 ³	θ_{pc} rad × 10 ³	θ_u rad × 10 ³	Λ	κ^c
9	0.052	1348	1684	68.1	240	66.9	246	150	2.55	0.48
8	0.115	1308	1614	64.9	223	63.8	228	150	2.55	0.45
7	0.139	1581	1989	76.4	235	75.3	240	150	3.36	0.44
6	0.189	1539	1916	73.2	219	72.2	225	150	3.36	0.42
5	0.160	2124	2762	120.2	283	118.9	289	150	5.68	0.44
4	0.194	2081	2705	116.3	269	115.0	274	150	5.68	0.42
3	0.138	2037	2649	112.4	255	111.2	260	150	5.68	0.44
2	0.159	1993	2340	91.0	197	90.0	204	150	5.68	0.44

a. expected flexural strength reduced by the applied axial compression load calculate, b. calculated using GCR 17-917-46v2 Eq. 4-13, c. $0.5-0.4P_g/P_{yc}$

Table 16. Nonlinear column properties for lower hinge of each story in pier 2 of the 8-story RSA-designed frame: stiffness.

Floor	Member			Hinge Spring			Beam-Column
	K kip-ft $\times 10^{-3}$ / rad	α_s $\times 10^3$	α_c $\times 10^3$	K kip-ft $\times 10^{-3}$ / rad	α_s $\times 10^3$	α_c $\times 10^3$	K kip-ft $\times 10^{-3}$ / rad
9	35,641	19.9	-28.3	392,049	1.85	-2.51	39,205
8	36,048	18.9	-29.0	396,531	1.74	-2.57	39,653
7	45,973	16.7	-26.5	505,701	1.54	-2.36	50,570
6	46,028	16.1	-27.3	506,309	1.49	-2.42	50,631
5	65,324	11.7	-21.5	718,562	1.07	-1.92	71,856
4	65,377	11.8	-22.2	719,144	1.09	-1.97	71,914
3	65,430	12.0	-22.8	719,726	1.10	-2.03	71,973
2	44,024	12.5	-38.8	484,261	1.15	-3.40	48,426

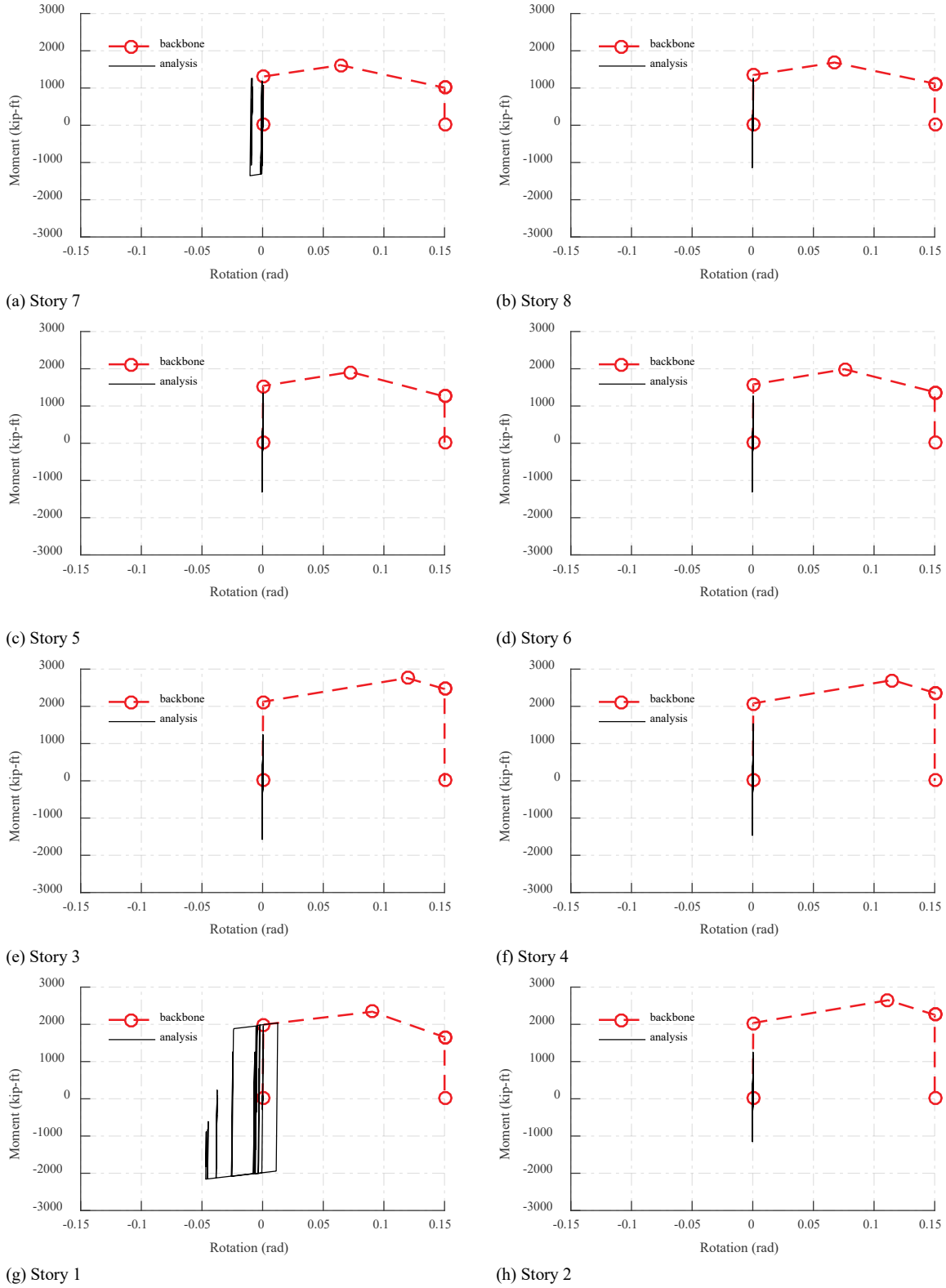


Figure 55. Column hinge backbone curves and select analysis results for lower hinge at each story in pier 2 of the 8-story RSA-designed building (EQ 1, $s_f = 2.0$).

C.2.3 Panel Zone Hinge

The panel zone properties are summarized in Table 17 for pier 2 of the 8-story RSA-designed frame. The resulting backbone curves for the panel zone hinge are plotted in Figure 56. The plots are in terms of moment-rotation, where the moment can be converted to shear force by dividing out the column depth. Analysis results of EQ 1 with a scale factor of 2.0 (record first normalized and anchor scaled – see Appendix F) are plotted with the backbone curve to verify the behavior. For this example, panel zone yielding occurs at each floor, with panel zone distortion as large as approximately 1.5 %. Given F_y is 50 ksi, γ_y equals 0.26 %. Therefore, the maximum values are approximately six times yield. The backbone curves and the analysis results match as expected.

Table 17. Nonlinear panel zone properties for each story in pier 2 of the 8-story RSA-designed frame.

Floor	General Panel Zone Properties						Hinge Spring
	V_y kip	M_y kip-ft	γ_y rad $\times 10^3$	θ_{pc} rad $\times 10^3$	K_e kip/rad $\times 10^3$	K_p kip/rad $\times 10^3$	K_s kip-in/rad $\times 10^3$
9	342	590	2.60	149	132	6.50	227
8	342	590	2.60	149	132	6.50	227
7	391	770	2.60	154	151	8.76	297
6	391	770	2.60	154	151	8.76	297
5	539	1073	2.60	177	208	15.6	413
4	539	1073	2.60	177	208	15.6	413
3	539	1082	2.60	203	208	15.5	417
2	539	1082	2.60	203	208	15.5	417

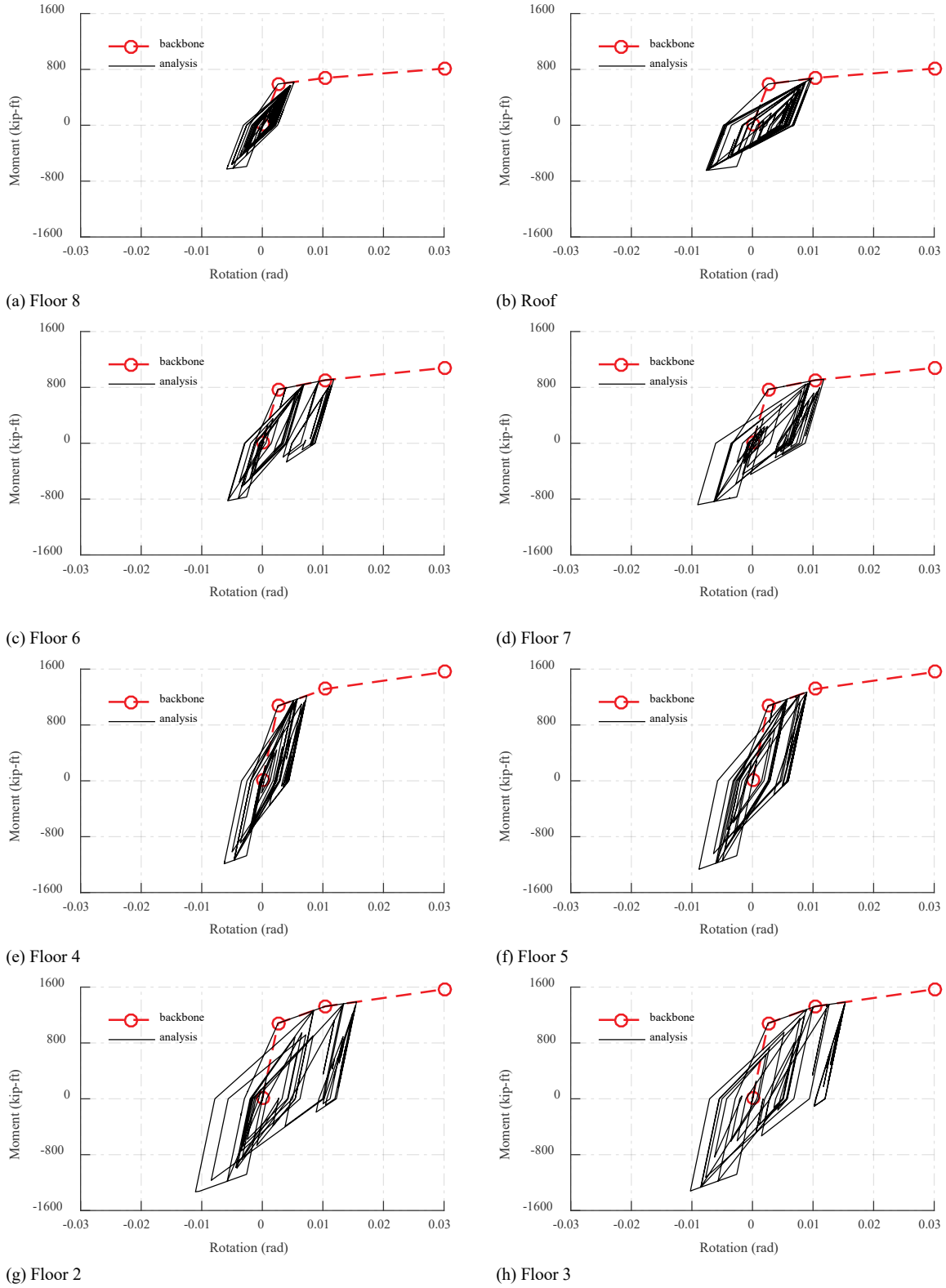


Figure 56. Panel zone hinge backbone curves and select analysis results for hinge at each story in pier 2 of the 8-story RSA-designed building (EQ 1, $sf = 2.0$).

Appendix D Implementation of Ibarra-Medina-Krawinkler Model

For a typical member with two plastic hinges as shown in Figure 57(a) subjected to symmetric loading of shear V and moment M at the two ends, the rotations at the hinges are shown in the figure. These rotations consist of the total rotation θ of the member with length L (sometimes referred to as chord rotation), the plastic rotation θ_s concentrated at the plastic hinge, and the elastic rotation θ_{bc} within the length L_{bc} of the beam-column. These rotations at the hinges can be expressed in equation form as:

$$\theta = \theta_{bc} + \theta_s \quad (22)$$

Corresponding to the plastic rotation at the plastic hinge is the moment m , and this hinge moment does not equal the member end moment M (i.e., $m \neq M$) when the hinges are offset from the member ends.

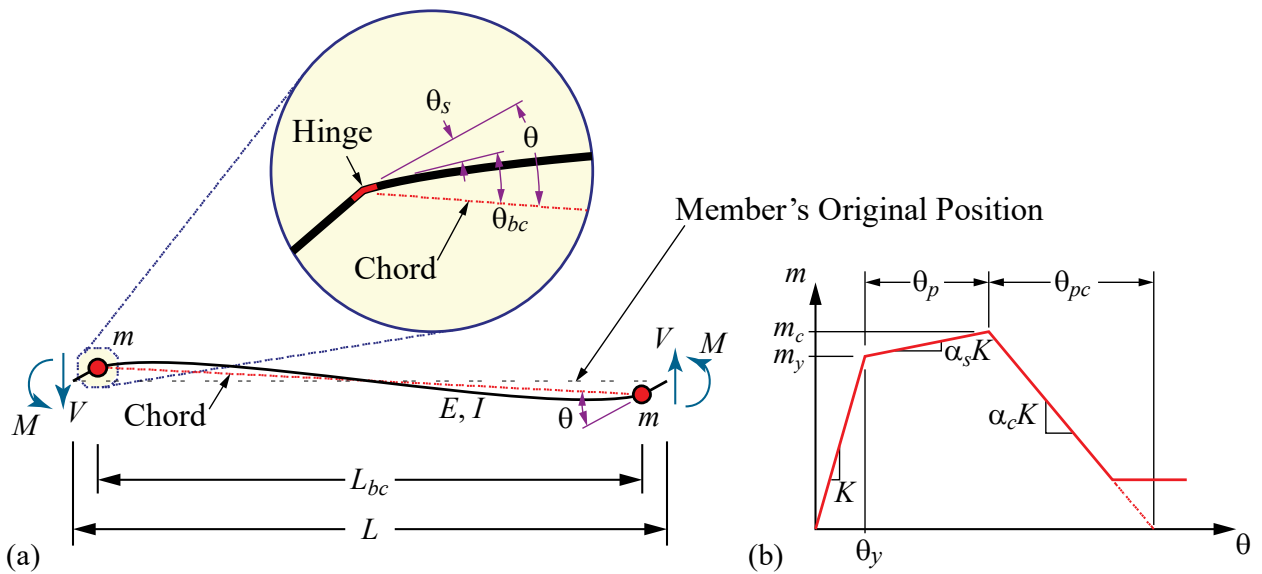


Figure 57. (a) Member subjected to symmetric loading and (b) The corresponding moment vs. rotation relationship at the hinge.

Backbone curves are often used to represent the behavior of the plastic hinges, and a commonly used backbone curve is implemented using the Ibarra-Medina-Krawinkler (IMK) model. A typical moment versus rotation curve based on the IMK model is shown in Figure 57(b), where the horizontal axis is the total rotation θ that includes both elastic rotation θ_{bc} and plastic rotation θ_s . Other parameters in the model include the yield rotation θ_y , yield moment m_y , moment capacity m_c , and the initial stiffness of the entire member K . This

initial stiffness K is sometimes referred to as K_{mem} (Ibarra 2005), and due to symmetric loading, this stiffness can be calculated by the formula:

$$K = \frac{m_y}{\theta_y} = \frac{6EI}{L_{bc}} \quad (23)$$

where E is the elastic modulus and I is the moment of inertia of the member. Finally, θ_p and θ_{pc} are the nonlinear properties of the member that are calibrated based on the properties of the member, and α_s and α_c can be calculated accordingly once m_y , m_c , θ_p , and θ_{pc} are known.

D.1 Implementation of IMK Model into General Software Packages

A challenge arises when the backbone curve as shown in Figure 58(b) is modeled using today's software packages. These software packages analyze the responses of the structure by separating the stiffness of the plastic hinge from the stiffness of the member, thereby allowing the flexibility of choosing one formulation over another in the modeling process. Once the formulation is chosen, the software package will then assemble the elastic stiffness according to the member definition and separately assemble the nonlinear stiffness according to the plastic hinge definition. Therefore, for any chord rotation θ in Eq. (23), the elastic rotation θ_{bc} of the member must be separated from the plastic rotation θ_s of the plastic hinge when constructing the appropriate computer model.

One simple solution to separate the elastic rotation from the plastic rotation is shown in Figure 58. As shown in Figure 58(b), the elastic rotation of member consists of a linear elastic stiffness K that does not yield, while the moment is capped by the amount of moment in the plastic hinge as shown in Figure 58(c). Also shown in Figure 58(c) is the initial stiffness being infinitely rigid after subtracting the elastic stiffness in Figure 58(b) from the total stiffness in Figure 58(a), and $\bar{\alpha}_s$, $\bar{\alpha}_c$, $\bar{\theta}_p$, and $\bar{\theta}_{pc}$ are the modified parameters for describing the backbone curve of the plastic hinge.

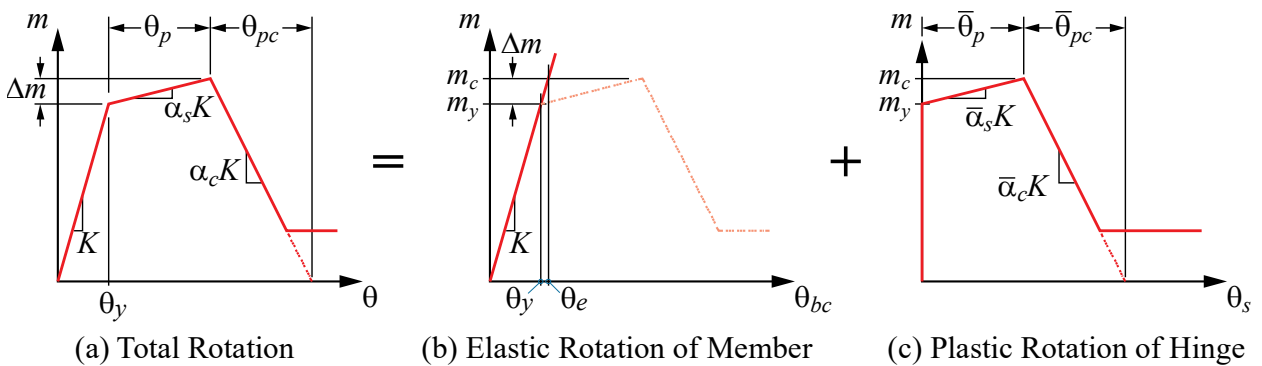


Figure 58. Separation of (a) total rotation into (b) elastic rotation of the member and (c) plastic rotation of the hinge.

Most software packages today have the capability of modeling the backbone curve for the plastic hinge as shown in Figure 58(c) to compute the structural responses. To satisfy the graphical equation presented in Figure 58, the parameters $\bar{\alpha}_s$, $\bar{\theta}_p$, and $\bar{\theta}_{pc}$ must be determined for use in the computer model. These parameters can be derived by first noting that the rotations corresponding to the moment capacity m_c in Figure 58 can be written as

$$\theta_y + \theta_p = \theta_e + \bar{\theta}_p \quad (24)$$

where $\theta_e = \theta_y + \Delta m/K$ from Figure 58(b). Substituting this equation into Eq. (24) and rearranging terms gives

$$\bar{\theta}_p = \theta_p - \Delta m/K \quad (25)$$

From Figure 58(a) and Figure 58(c) respectively, θ_p and $\bar{\theta}_p$ can be written as

$$\theta_p = \Delta m/\alpha_s K \quad , \quad \bar{\theta}_p = \Delta m/\bar{\alpha}_s K \quad (26)$$

Substituting Eq. (26) into Eq. (25) gives

$$\frac{\Delta m}{\bar{\alpha}_s K} = \frac{\Delta m}{\alpha_s K} - \frac{\Delta m}{K} \quad (27)$$

Therefore, solving for $\bar{\alpha}_s$ in Eq. (27) gives

$$\bar{\alpha}_s = \frac{\alpha_s}{1 - \alpha_s} \quad (28)$$

Then from Eq. (26),

$$\bar{\theta}_p = \frac{\Delta m}{\bar{\alpha}_s K} = \theta_p \frac{\alpha_s}{\bar{\alpha}_s} \quad (29)$$

substituting Eq. (28) into Eq. (29) gives

$$\bar{\theta}_p = (1 - \alpha_s)\theta_p \quad (30)$$

Similar equations can be derived for the relationships between $(\bar{\alpha}_c, \bar{\theta}_{pc})$ and (α_c, θ_{pc}) while noting that $\alpha_c < 0$ and $\bar{\alpha}_c < 0$. Consider the rotation corresponding to the zero moment after strength degradation as shown in Figure 58:

$$(\theta_y + \theta_p + \theta_{pc}) = 0 + (\bar{\theta}_p + \bar{\theta}_{pc}) \quad (31)$$

Substituting Eq. (24) into Eq. (31) and rearranging terms gives

$$\theta_e + \theta_{pc} = \bar{\theta}_{pc} \quad (32)$$

where $\theta_e = m_c/K$ from Figure 58(b). Substituting this equation into Eq. (32) and rearranging terms gives

$$\bar{\theta}_{pc} = \theta_{pc} + m_c/K \quad (33)$$

From Figure 58(a) and Figure 58(c) respectively, θ_{pc} and $\bar{\theta}_{pc}$ can be written as

$$\theta_{pc} = -m_c/\alpha_c K \quad , \quad \bar{\theta}_{pc} = -m_c/\bar{\alpha}_c K \quad (34)$$

Substituting Eq. (34) into Eq. (33) gives

$$-\frac{m_c}{\bar{\alpha}_c K} = -\frac{m_c}{\alpha_c K} + \frac{m_c}{K} \quad (35)$$

Therefore, solving for $\bar{\alpha}_c$ in Eq. (35) gives

$$\bar{\alpha}_c = \frac{\alpha_c}{1 - \alpha_c} \quad (36)$$

Then from Eq. (34),

$$\bar{\theta}_{pc} = -\frac{m_c}{\bar{\alpha}_c K} = \theta_{pc} \frac{\alpha_c}{\bar{\alpha}_c} \quad (37)$$

substituting Eq. (36) into Eq. (37) gives

$$\bar{\theta}_{pc} = (1 - \alpha_c)\theta_{pc} \quad (38)$$

D.2 Implementation of IMK Model into OpenSees Using the Bilin Uniaxial Material

Some software packages are capable of defining the backbone curves for plastic hinges in the model by specifying the parameters based on Eqs. (28), (30), and (38). However, difficulties occur when the backbone curve in Figure 58(c) is modeled using OpenSees, where hinge spring and the beam-column spring must be combined in series. The BILIN uniaxial material is used to capture such backbone curve. BILIN can capture in-cycle and cyclic degradation behavior, but use of this approach (i.e., springs in series) requires the initial stiffness be a finite number rather than infinity. Therefore, Figure 58 must be modified to reflect a large but finite initial stiffness that is needed to model the plastic hinges. This modification is shown in Figure 59, where the initial stiffness of the member K is separated into the linear elastic stiffness of the beam-column K_{bc} and the initial stiffness of the plastic hinge K_s . To achieve a relatively large but finite initial stiffness for the plastic hinge, let

$$K_s = nK_{bc} \quad (39)$$

where n is a large number. Doing so sets the stiffness of the plastic hinge to be n times the stiffness of the member. Note that when $n \rightarrow \infty$, Figure 59 becomes Figure 58. A choice of $n = 10$ is recommended for providing a sufficiently large stiffness while avoiding numerical instability [35].

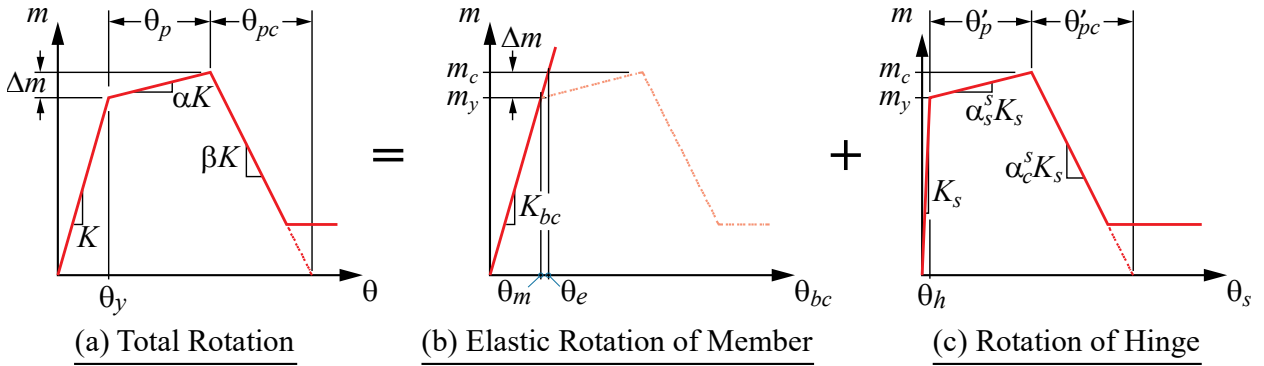


Figure 59. Separation of (a) total rotation into (b) elastic rotation of the member and (c) rotation of the plastic hinge for implementation using BILIN in OpenSees.

The objective now is to determine the parameters K_{bc} , K_s , α_s^s , θ'_p , and θ'_{pc} . Consider first the rotations corresponding to the yield moment m_y as shown in Figure 59:

$$\theta_y = \theta_m + \theta_h \quad (40)$$

where $\theta_y = m_y/K$, $\theta_m = m_y/K_{bc}$, and $\theta_h = m_y/K_s$ according to Figure 59. Substituting these equations into Eq. (40) gives

$$\frac{m_y}{K} = \frac{m_y}{K_{bc}} + \frac{m_y}{K_s} \quad (41)$$

Now dropping the common term m_y in Eq. (41) and substituting Eq. (39) into Eq. (41) gives

$$\frac{1}{K} = \frac{1}{K_{bc}} + \frac{1}{nK_{bc}} \quad (42)$$

and solving for K_{bc} in Eq. (42) gives

$$K_{bc} = \frac{n+1}{n} K \quad (43)$$

Then substituting Eq. (43) into Eq. (39) gives

$$K_s = (n+1)K \quad (44)$$

Note that as $n \rightarrow \infty$, $K_{bc} \rightarrow K$ in Eq. (43) and $K_s \rightarrow \infty$ in Eq. (44).

Equation (43) shows that the elastic stiffness of the member over the length L_{bc} should be magnified by a factor of $(n+1)/n$ to compensate for the reduction in initial stiffness of the plastic hinge from infinitely rigid to a finite number. This magnification of elastic stiffness over the member length L_{bc} can often be done by increasing the moment of inertia I in Eq. (23) by the factor of $(n+1)/n$.

Now consider the rotations corresponding to the moment capacity m_c . From Figure 59,

$$(\theta_y + \theta_p) = \theta_e + (\theta_h + \theta'_p) \quad (45)$$

Substituting Eq. (40) into Eq. (45) and rearranging terms gives

$$\theta_p = \theta_e - \theta_m + \theta'_p \quad (46)$$

where according to Figure 59,

$$\theta_p = \Delta m / \alpha K \quad , \quad \theta_e - \theta_m = \Delta m / K_{bc} \quad , \quad \theta'_p = \Delta m / \alpha_s^s K_s \quad (47)$$

Now substituting Eq. (47) into Eq. (46) gives

$$\frac{\Delta m}{\alpha K} = \frac{\Delta m}{K_{bc}} + \frac{\Delta m}{\alpha_s^s K_s} \quad (48)$$

Substituting Eqs. (43) and (44) into Eq. (48) and dropping the common term $\Delta m / K$ gives

$$\frac{1}{\alpha} = \frac{n}{n+1} + \frac{1}{\alpha_s^s (n+1)} \quad (49)$$

Therefore, solving for α_s^s in Eq. (49), it follows that

$$\alpha_s^s = \frac{\alpha_s}{n+1 - n\alpha_s} \quad (50)$$

Then from the first and third equations of Eq. (47),

$$\theta'_p = \frac{\Delta m}{\alpha_s^s K_s} = \theta_p \frac{\alpha_s K}{\alpha_s^s K_s} \quad (51)$$

substituting Eqs. (44) and (50) into Eq. (51) gives

$$\theta'_p = \frac{n+1 - n\alpha_s}{n+1} \theta_p \quad (52)$$

Note in Eq. (52) that as $n \rightarrow \infty$, $\theta'_p \rightarrow (1 - \alpha_s)\theta_p$, which is the same as Eq. (30) for the case of having infinitely rigid initial stiffness for modeling the plastic hinges.

Similar equations can be derived for the relationships between $(\alpha_c^s, \theta'_{pc})$ and (α_c, θ_{pc}) while noting that $\alpha_c < 0$ and $\alpha_c^s < 0$. Consider the rotations corresponding to the zero moment after strength degradation as shown in Figure 59:

$$(\theta_y + \theta_p + \theta_{pc}) = 0 + (\theta_h + \theta'_p + \theta'_{pc}) \quad (53)$$

Substituting Eq. (45) into Eq. (53) and rearranging terms gives

$$\theta_{pc} + \theta_e = \theta'_{pc} \quad (54)$$

where according to Figure 59,

$$\theta_{pc} = -m_c/\alpha_c K \quad , \quad \theta_e = m_c/K_{bc} \quad , \quad \theta'_{pc} = -m_c/\alpha_c^s K_s \quad (55)$$

Now substituting Eq. (55) into Eq. (54) gives

$$-\frac{m_c}{\alpha_c K} + \frac{m_c}{K_{bc}} = -\frac{m_c}{\alpha_c^s K_s} \quad (56)$$

Substituting Eqs. (43) and (44) into Eq. (56) and dropping the common term m_c/K gives

$$-\frac{1}{\alpha_c} + \frac{n}{n+1} = -\frac{1}{\alpha_c^s(n+1)} \quad (57)$$

Therefore, solving for α_c^s in Eq. (57), it follows that

$$\alpha_c^s = \frac{\alpha_c}{n+1-n\alpha_c} \quad (58)$$

Then from the first and third equations of Eq. (55),

$$\theta'_{pc} = -\frac{m_c}{\alpha_c^s K_s} = \theta_{pc} \frac{\alpha_c K}{\alpha_c^s K_s} \quad (59)$$

substituting Eqs. (44) and (58) into Eq. (59) gives

$$\theta'_{pc} = \frac{n+1-n\alpha_c}{n+1} \theta_{pc} \quad (60)$$

Again, note in Eq. (60) that as $n \rightarrow \infty$, $\theta'_{pc} \rightarrow (1 - \alpha_c)\theta_{pc}$, which is the same as Eq. (38) for the case of having infinitely rigid initial stiffness for modeling the plastic hinges.

In summary, the parameters calculated using Eqs. (43), (44), (50), (52), and (60) can be used as inputs to the BILIN uniaxial material model in OpenSees to capture the same behavior of the plastic hinges as the one shown in Figure 57(b).

D.3 Stiffness Calculation for Members with Reduced Beam Sections

Reduced beam sections (RBS) are used in all the beam members of the frames to limit all nonlinear behaviors to these sections. However, reducing the sizes in certain sections in the beam (see Figure 60(a)) results in having an initial stiffness K_{bc} of the member that is smaller than the one computed using Eq. (43). To evaluate the reduced initial stiffness K_{bc} , approximation to the RBS is first performed using the same approach taken in the Perform-3D models used in Harris and Speicher [3]. The approximated model is shown in Figure 60(b), where the reduced flange width b_r is taken to be the width corresponding to the location $b/3$ away from the center of the RBS as illustrated in Figure 60(a) and assumed to be constant over the entire RBS length b . Doing so, the moment of inertia of the RBS, I_r , can be calculated accordingly.

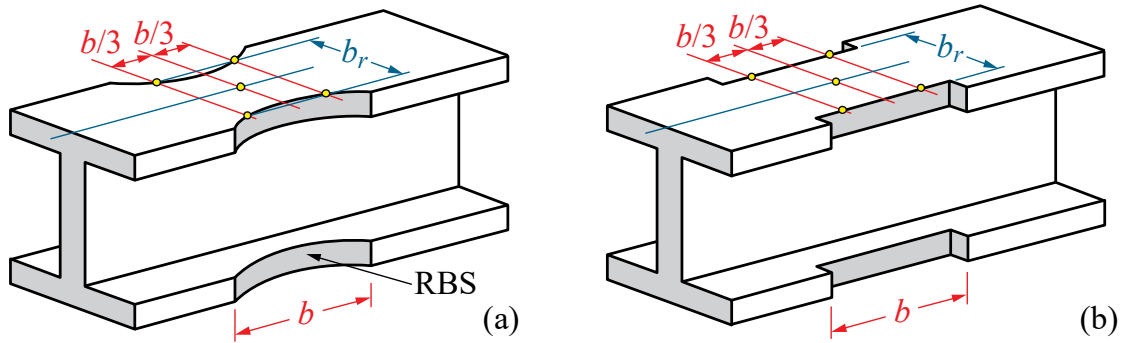


Figure 60. (a) Reduced beam section and (b) approximate computer model.

To calculate the initial stiffness of the beam K_{bc} from center of the left RBS to center of the right RBS over the length L_{bc} as shown in Figure 61(a), the reduced sections having the reduced moment of inertia I_r should be accounted for. This can be done using the Moment-Area Method. First, the moment diagram for the beam with length L_{bc} is shown in Figure 61(b), where m is the moment at the two ends of the beam. The objective here is to compute the chord rotation θ as shown in Figure 61(a). Doing so, the initial stiffness can then be computed as:

$$K_{bc} = m/\theta \quad (61)$$

Next, the M/EI -diagram is constructed as shown in Figure 61(c) by dividing the moment diagram in Figure 61(b) by the elastic modulus E and the corresponding moment of inertia I or reduced moment of inertia I_r . By using the Moment-Area Method, the tangential deviation at the midspan of the beam relative to the left end, denoted here as Δ_m as shown in Figure 61(a), is computed by subtracting the moment of the smaller triangle from the moment of the larger triangle, i.e.,

$$\Delta_m = \left(\frac{1}{2} \times \frac{L_{bc}}{2} \times \frac{m}{EI_r} \right) \left(\frac{2}{3} \times \frac{L_{bc}}{2} \right) - \left(\frac{1}{2} \times \frac{L_{bc}-b}{2} \times \frac{L_{bc}-b}{L_{bc}} \left(\frac{m}{EI_r} - \frac{m}{EI} \right) \right) \left(\frac{2}{3} \times \frac{L_{bc}-b}{2} \right) \quad (62)$$

or simplifying the equation gives:

$$\Delta_m = \frac{m}{12E} \left(\frac{L_{bc}^2}{I_r} - \frac{(L_{bc}-b)^3}{L_{bc}I_r} + \frac{(L_{bc}-b)^3}{L_{bc}I} \right) \quad (63)$$

Then the chord rotation θ can be calculated as:

$$\theta = \frac{\Delta_m}{L_{bc}/2} = \frac{m}{6E} \left(\frac{L_{bc}}{I_r} - \frac{(L_{bc}-b)^3}{L_{bc}^2 I_r} + \frac{(L_{bc}-b)^3}{L_{bc}^2 I} \right) \quad (64)$$

Finally, substituting Eq. (64) into Eq. (61) gives:

$$K_{bc} = \frac{6E}{\frac{L_{bc}}{I_r} - \frac{(L_{bc}-b)^3}{L_{bc}^2 I_r} + \frac{(L_{bc}-b)^3}{L_{bc}^2 I}} \quad (65)$$

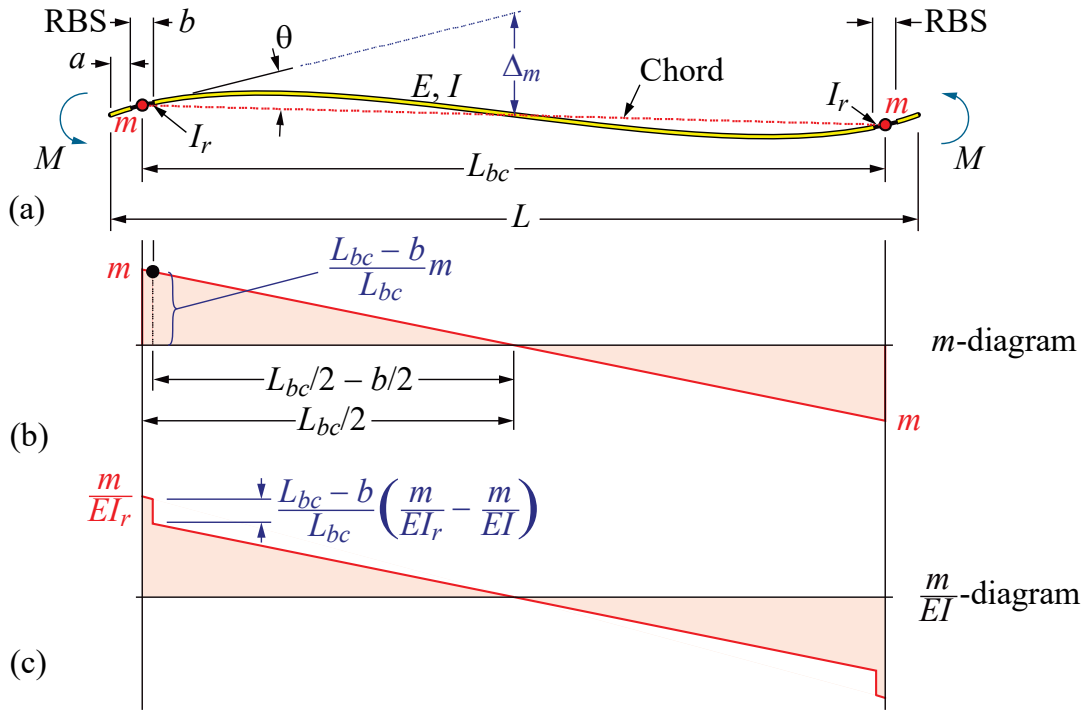


Figure 61. Computation of the initial stiffness for (a) beam with RBS and (b) the corresponding moment diagram and (c) the corresponding m/EI diagram.

Note that if no RBS is used, then $I_r = I$ and Eq. (65) reduces to Eq. (23), which is $6EI/L_{bc}$. By using RBS in the moment frames of this study, the reduced stiffness computed using Eq. (65) is generally around 95% of those values computed using Eq. (23).

Appendix E Supplemental Calculations for FEMA P695

FEMA P695 requires a period-based ductility factor, μ_T , to calculate the spectral shape factor, SSF . The μ_T is calculated by conducting a pushover analysis as follows:

1. Apply gravity loads of $1.05D + 0.25L$ where D is the nominal dead load and superimposed deadload, and L is the nominal live load.
2. Define a vertical distribution of the lateral force, F_x , at each story level x . The vertical distribution is proportional to the mass times the fundamental mode shape:

$$F_x \propto m_x \phi_{1,x} \quad [\text{FEMA P695 equation (6-4)}] \quad (66)$$

where m_x is the mass at level x and $\phi_{1,x}$ is the ordinate of mode 1 at level x .

3. Apply lateral force defined above monotonically until a 20 % loss of the base shear capacity is achieved.

The resulting pushover plots for each of the baseline models is shown in Figure 62 through Figure 64. Note, the base shear shown in these plots are from the OpenSees model which represents *half* the building.

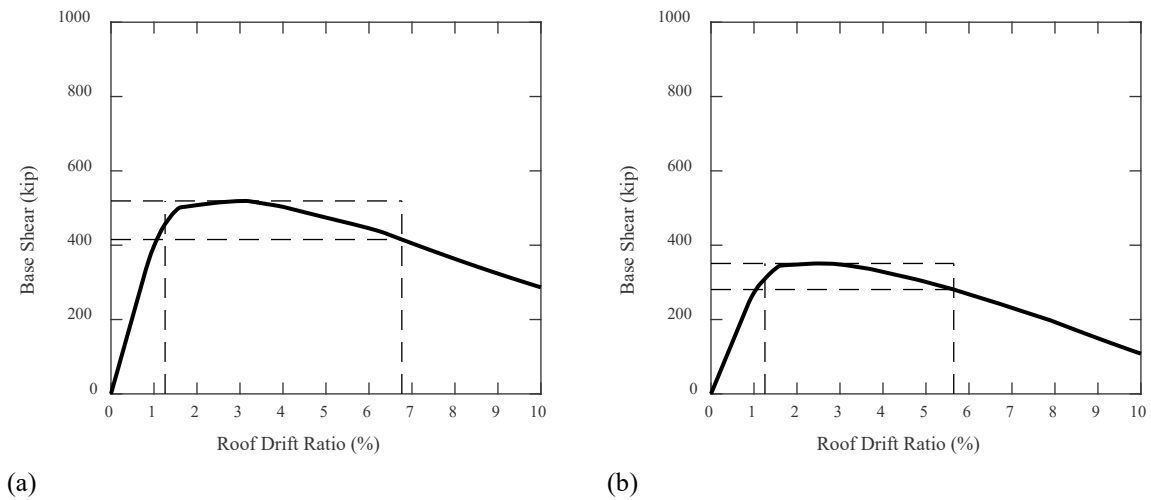


Figure 62. Nonlinear static pushover curves for the 4-story (a) ELF and (b) RSA designs.

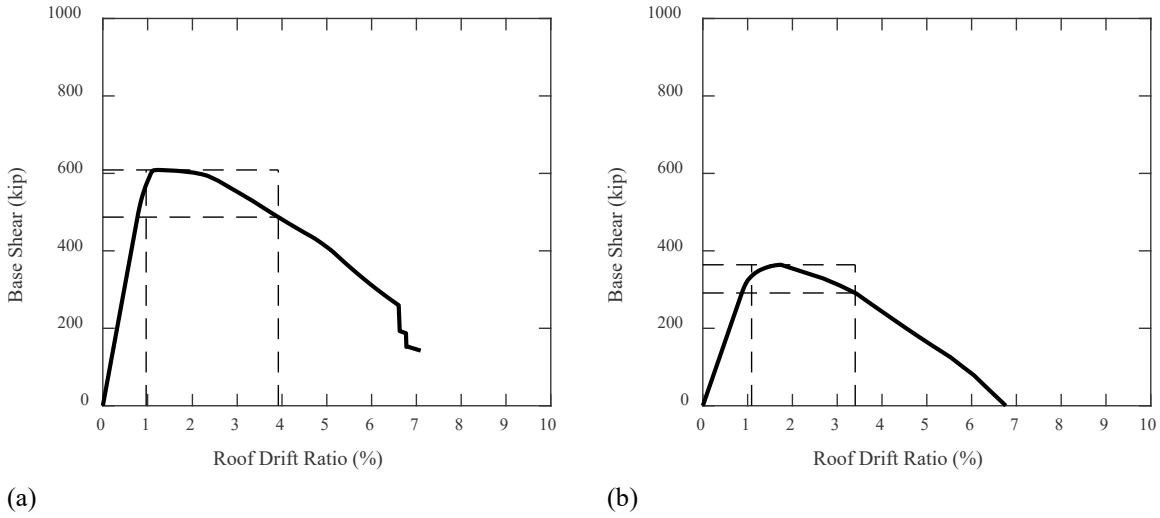


Figure 63. Nonlinear static pushover curves for the 8-story (a) ELF and (b) RSA designs.

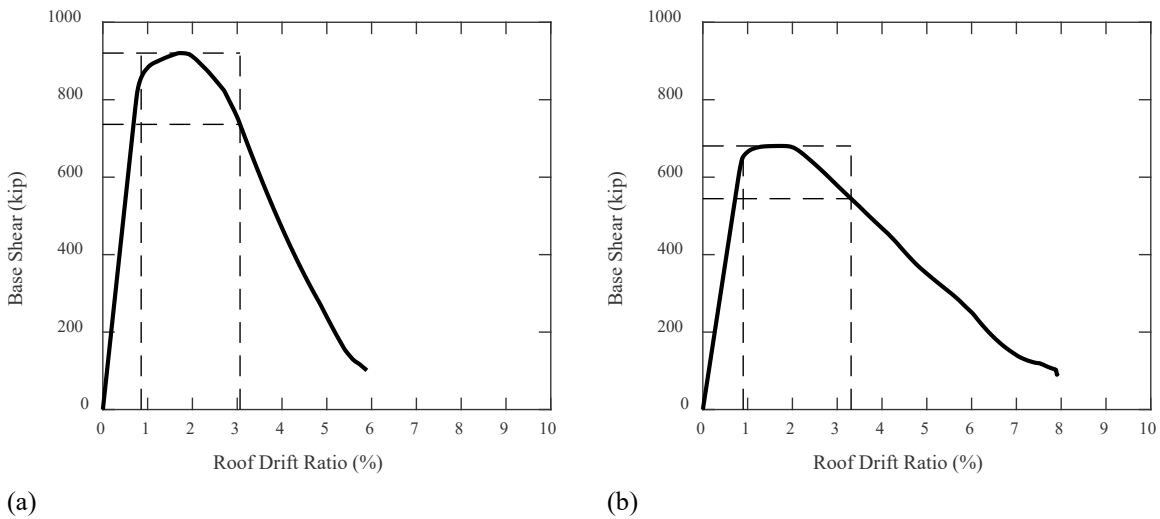


Figure 64. Nonlinear static pushover curves for the 16-story (a) ELF and (b) RSA designs.

The period-based ductility factor μ_T can be calculated by the formula:

$$\mu_T = \frac{\delta_u}{\delta_{y,eff}} \tag{67}$$

where δ_u is the roof displacement when the base shear hits 0.8 of the peak base shear on the descending branch and $\delta_{y,eff}$ is the effective yield roof displacement. Both values are shown in Figure 65. Note that $\delta_{y,eff}$ is defined as the displacement corresponding to the

maximum base shear divided by the initial stiffness K . FEMA P695 presents an equation to calculate $\delta_{y,eff}$:

$$\delta_{y,eff} = \phi_{1,r} \Gamma_1 \frac{V_{max}}{W} \left[\frac{g}{4\pi^2} \right] (\max(T, T_1))^2 \quad (68)$$

where $\phi_{1,r}$ is the value of the first mode shape at the roof and Γ_1 modal participation factor of the first mode computed as:

$$\Gamma_1 = \frac{\sum_{x=1}^N m_x \phi_{1,x}}{\sum_{x=1}^N m_x \phi_{1,x}^2} \quad (69)$$

and V_{max} is the maximum base shear as illustrated in Figure 65. However, based on Eq. (68), $\delta_{y,eff}$ does not fall within the initial stiffness K as presented in Figure 65.

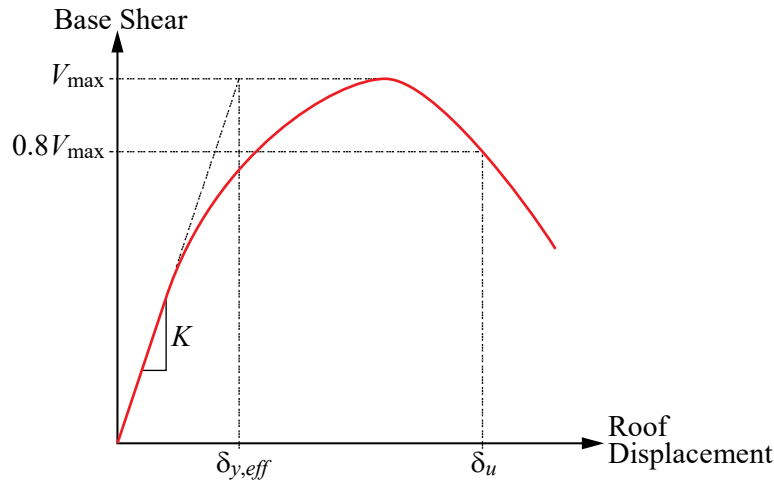


Figure 65. Typical nonlinear pushover curve.

It was observed that the calculation of $\delta_{y,eff}$ gave a smaller value than would be realized by fitting a line to the initial stiffness of the pushover curve. Figure 66 illustrates this issue for the 4-story ELF design with the red line representing the initial stiffness and the blue line representing the value as calculated in FEMA P695. Therefore, the calculation of $\delta_{y,eff}$ needs to be re-derived.

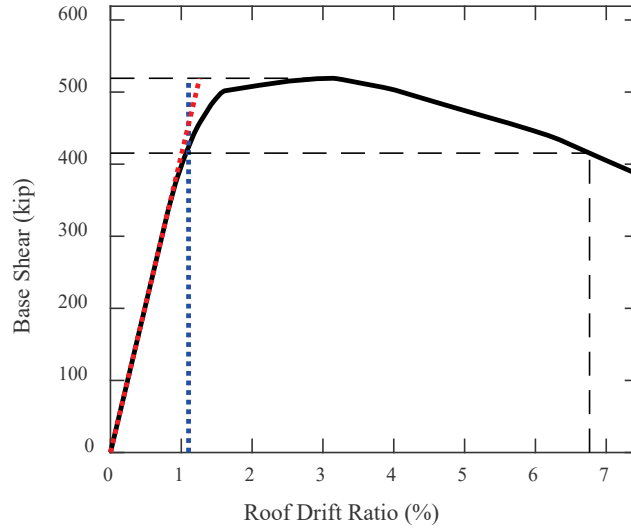


Figure 66. Nonlinear Pushover curve for 4-story ELF design

Consider the transformations between the structure's coordinates and the modal coordinates for the roof displacement and base shear:

$$\delta_{roof} = \phi_{1,r}D_1 + \phi_{2,r}D_2 + \dots + \phi_{N,r}D_N \quad (70)$$

$$V = \Gamma_1V_1 + \Gamma_2V_2 + \dots + \Gamma_NV_N \quad (71)$$

where D_i is the modal displacement of the i^{th} mode and V_i is the base shear of the i^{th} mode. Note that Eqs. (70) and (71) are correct only when the structure is responding in the elastic range. Since the applied force is proportional to the mass multiplied by the first mode shape as shown in Eq. (66), the displacement response will only follow the first mode shape and all other modes will not be contributing to the response. This gives $D_2 = D_3 = \dots = D_N = 0$ and $V_2 = V_3 = \dots = V_N = 0$. Substituting this result into Eqs. (70) and (71) gives:

$$\delta_{roof} = \phi_{1,r}D_1 \quad (72)$$

$$V = \Gamma_1V_1 \quad (73)$$

At the same time, the displacement of the first mode D_1 is related to the base shear of the first mode V_1 by the formula:

$$V_1 = k_1D_1 \quad (74)$$

where k_1 is the modal stiffness of the first mode, typically computed through the normalization of the stiffness matrix or the normalization of the mass matrix, i.e.,

$$k_1 = \phi_1^T \mathbf{K} \phi_1 = \omega_1^2 m_1 = \omega_1^2 \phi_1^T \mathbf{M} \phi_1 = \omega_1^2 \sum_{x=1}^N m_x \phi_{1,x}^2 \quad (75)$$

Substituting Eq. (74) into Eq. (75) and solving for D_1 gives:

$$D_1 = \frac{V}{\Gamma_1 k_1} \quad (76)$$

Now substituting Eq. (75) into Eq. (76) and substituting the resulting equation in Eq. (72) gives:

$$\delta_{roof} = \phi_{1,r} \frac{V}{\Gamma_1 \omega_1^2 m_1} \quad (77)$$

Since $\omega_1 = 2\pi/T_1$, substituting this equation into Eq. (12) and rearranging terms gives:

$$\delta_{roof} = \phi_{1,r} \frac{V}{\Gamma_1 m_1} \left(\frac{1}{4\pi^2} \right) T_1^2 \quad (78)$$

Finally, setting the base shear V in Eq. (13) to V_{\max} in Figure 4, the corresponding δ_{roof} in Eq. (13) becomes $\delta_{y,eff}$, i.e.,

$$\delta_{y,eff} = \phi_{1,r} \frac{V_{\max}}{\Gamma_1 m_1} \left(\frac{1}{4\pi^2} \right) T_1^2 \quad (79)$$

The corresponding results are summarized in Table 18. Once the μ_T is known and given the suite of buildings are SDC D_{\max} , the spectral shape factor (SSF) can be obtained from FEMA P695 Table 7-1b. For this building suite, the SSF ranges from 1.35 to 1.48.

Table 18. Pushover analysis response quantities.

Building	V_{design} (kip)	V_{\max} (kip)	Static Ω	$\delta_{y,eff}$ (in)	δ_u (in)	μ_T	T_1 (s)	SSF
04ELF	374	1038	2.78	9.1	48.7	5.4	1.76	1.48
04RSA	316	702	2.22	9.0	40.7	4.5	2.15	1.43
08ELF	467	1218	2.61	13.5	54.5	4.1	2.69	1.40
08RSA	394	728	1.85	15.2	47.4	3.1	3.59	1.35
16ELF	958	1841	1.92	23.4	83.8	3.6	3.89	1.38
16RSA	810	1361	1.68	24.7	90.6	3.7	4.48	1.38

Example calculations leading to the *SSF* are now given for the 4-story ELF building model. The mode shape for the 4-story ELF model is given in Figure 67, and in Table 19 along with the mass values at each floor.

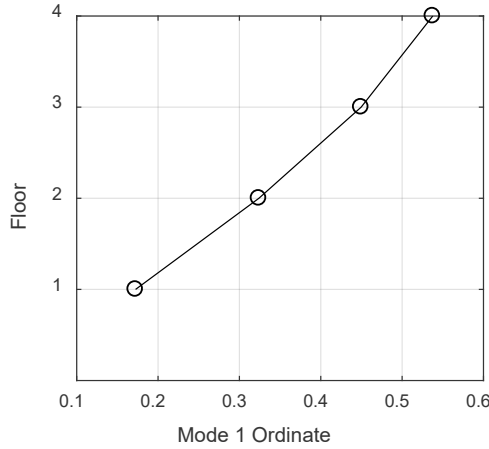


Figure 67. Mode shape of 4-ELF-designed frame.

Table 19. Mode shape and Mass at each floor of 4-ELF design

Floor	1 st Mode Shape Ordinate	Mass (kip/g)
1	0.17	1.78
2	0.32	1.76
3	0.45	1.74
4(roof)	0.54	1.42

From these values, the modal participation factor and the $\delta_{y,eff}$ value can be calculated.

From the pushover curve, we found the ultimate delta. With that value, the period-based ductility is calculated in Eq. (82).

$$\Gamma_1 = \frac{\sum_{x=1}^N m_x \phi_{1,x}}{\sum_{x=1}^N m_x \phi_{1,x}^2} \quad (80)$$

$$\Gamma_1 = \frac{(1.78)(0.17) + (1.76)(0.32) + (1.74)(0.45) + (1.42)(0.54)}{1.78(0.17)^2 + 1.76(0.32)^2 + 1.74(0.45)^2 + 1.42(0.54)^2} = 2.42$$

$$\delta_{y,eff} = \phi_{1,r} \frac{V_{max}}{\Gamma_1 m_1} \left(\frac{1}{4\pi^2} \right) T_1^2 = 0.54 \times \frac{519}{2.42 \times 1.00} \left(\frac{1}{4\pi^2} \right) (1.76)^2 = 9.1 \quad (81)$$

$$\mu_T = \frac{\delta_u}{\delta_{y,eff}} = \frac{48.7}{9.1} = 5.35 \quad (82)$$

The *SSF* is found by referencing Table 7-1b in FEMA P695 and interpolating between values. Table 20 shows a portion of the P695 table and Eq. (83) shows the linear interpolation used to arrive at the final value. The *SSF* can then be used to determine the adjusted collapse margin ratio summarized in the discussion section of this report.

Table 20. Spectral shape factor, *SSF*, for archetypes designed using SDC D_{max} (abbreviated from Table 7-1b of FEMA P695).

T (s.)	Period-Based Ductility, μ_T			
	3	4	6	≥ 8
≥ 1.5	1.32	1.4	1.51	1.61

$$y = SSF = 0.055 \times \mu_T + 1.18 = 1.48 \quad (83)$$

Appendix F Ground Motion Suite Characteristics

FEMA P695 methodology details two sets of ground motion records to be used for the nonlinear analyses prescribed in the method: Far field ground motion record set, and Near field ground motion record set. The Far Field set includes 22 component pairs of ground motion records that were at sites at least 10 km from the fault rupture. The Near Field set includes 28 component pairs of records that were recorded at sites less than 10 km from the fault rupture. The Far Field set was chosen for this project because the buildings were design to the SDC D criteria, indicating a structure located away from active faults. This appendix describes the Far Field ground motion set, the scaling used for each building, and the ground motion spectra for each record.

The FEMA P695 method requires that all records in the set be normalized so that 50 % of the ground motions collapse the analysis model. The normalization scale factors were specific to each ground motion record pair. Table 21 lists each ground motion name, the number data points and time step for the record, and the normalization factor used for this study.

Table 21. FEMA P695 far field ground motion set.

EQ order	Component Name	Filename	npts	dt	Normalization Factor
1	Northridge-BH	MUL009.AT2	2999	0.01	0.651
2	Northridge-BH	MUL279.AT2	2999	0.01	0.651
3	Northridge-CC	LOS000.AT2	1999	0.01	0.8283
4	Northridge-CC	LOS270.AT2	1999	0.01	0.8283
5	Duzce-Bolu	BOL000.AT2	5590	0.01	0.629
6	Duzce-Bolu	BOL090.AT2	5590	0.01	0.629
7	Hector-Hector	HEC000.AT2	4531	0.01	1.0908
8	Hector-Hector	HEC090.AT2	4531	0.01	1.0908
9	Imperial Valley-Delta	H-DLT262.AT2	9992	0.01	1.3119
10	Imperial Valley-Delta	H-DLT352.AT2	9992	0.01	1.3119
11	Imperial Valley-EC	H-E11140.AT2	7807	0.005	1.0144
12	Imperial Valley-EC	H-E11230.AT2	7807	0.005	1.0144
13	Kobe-Nishi Akashi	NIS000.AT2	4096	0.01	1.0318
14	Kobe-Nishi Akashi	NIS090.AT2	4096	0.01	1.0318
15	Kobe-Shin Osaka	SHI000.AT2	4096	0.01	1.0989
16	Kobe-Shin Osaka	SHI090.AT2	4096	0.01	1.0989
17	Kocaeli-Duzce	DZC180.AT2	5437	0.005	0.6896
18	Kocaeli-Duzce	DZC270.AT2	5437	0.005	0.6896
19	Kocaeli-Arcelik	ARC000.AT2	6000	0.005	1.3673
20	Koaceli-Arcelik	ARC090.AT2	6000	0.005	1.3673
21	Landers-Yermo	YER270.AT2	2200	0.02	0.986
22	Landers-Yermo	YER360.AT2	2200	0.02	0.986
23	Landers-Coolwater	CLW-LN.AT2	11186	0.0025	1.1483
24	Landers-Coolwater	CLW-TR.AT2	11186	0.0025	1.1483
25	Loma Prieta-Capitola	CAP000.AT2	7991	0.005	1.0923
26	Loma Prieta-Capitola	CAP090.AT2	7991	0.005	1.0923
27	Loma Prieta-Gilroy	G03000.AT2	7989	0.005	0.8803
28	Loma Prieta-Gilroy	G03090.AT2	7989	0.005	0.8803

29	Manjil-Abbar	ABBAR--L.AT2	2676	0.02	0.7705
30	Manjil-Abbar	ABBAR--T.AT2	2676	0.02	0.7705
31	Superstition Hills-EC	B-ICC000.AT2	8000	0.005	0.8701
32	Superstition Hills-EC	B-ICC090.AT2	8000	0.005	0.8701
33	Superstition Hills-Poe	B-POE270.AT2	2230	0.01	1.1729
34	Superstition Hills-Poe	B-POE360.AT2	2230	0.01	1.1729
35	Cape Mendocino-Rio Dell	RIO270.AT2	1800	0.02	0.8186
36	Cape Mendocino-Rio Dell	RIO360.AT2	1800	0.02	0.8186
37	Chi Chi-CHY	CHY101-E.AT2	18000	0.005	0.4119
38	Chi Chi-CHY	CHY101-N.AT2	18000	0.005	0.4119
39	Chi Chi-TCU	TCU045-E.AT2	18000	0.005	0.9606
40	Chi Chi-TCU	TCU045-N.AT2	18000	0.005	0.9606
41	San Fernando-LA	PEL180.AT2	2800	0.01	2.1003
42	San Fernando-LA	PEL090.AT2	2800	0.01	2.1003
43	Friuli-Tolmezzo	A-TMZ000.AT2	7269	0.005	1.4393
44	Friuli-Tolmezzo	A-TMZ270.AT2	7269	0.005	1.4393

Each ground motion in the set was then scaled to the MCE spectral acceleration using anchoring scale factors. These factors can be found using Table A-3 in FEMA P695, and are based on the fundamental period of each building using $C_u T_a$. The anchor scale factor for each building type is described in the Table 22.

Table 22. Scale factors to anchor median spectral value to MCE spectrum at $C_u T_a$.

Height	Design	Anchor Scale Factor
4-story	RSA	2.6022
	ELF	2.6022
8-story	RSA	2.9183
	ELF	2.9183
16-story	RSA	3.7476
	ELF	3.7476

Figure 68 and Figure 69 show the unscaled and normalized spectra for the ground motion record set. The median value of the entire set is indicated in the dark gray line. Individual plots of the normalized spectra for each ground motion record are also shown.

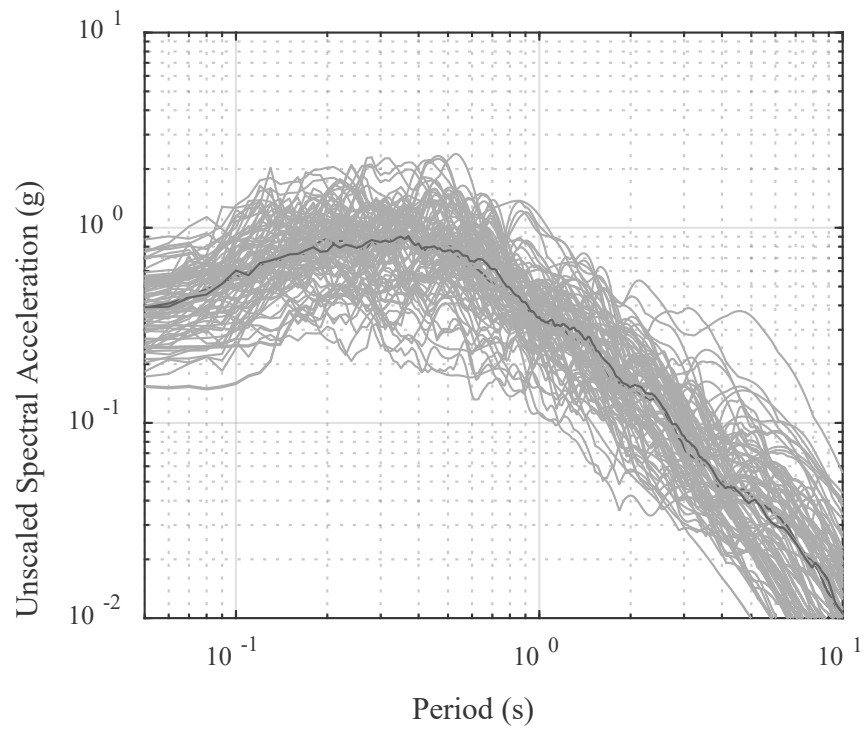


Figure 68. Unscaled ground motion response spectra.

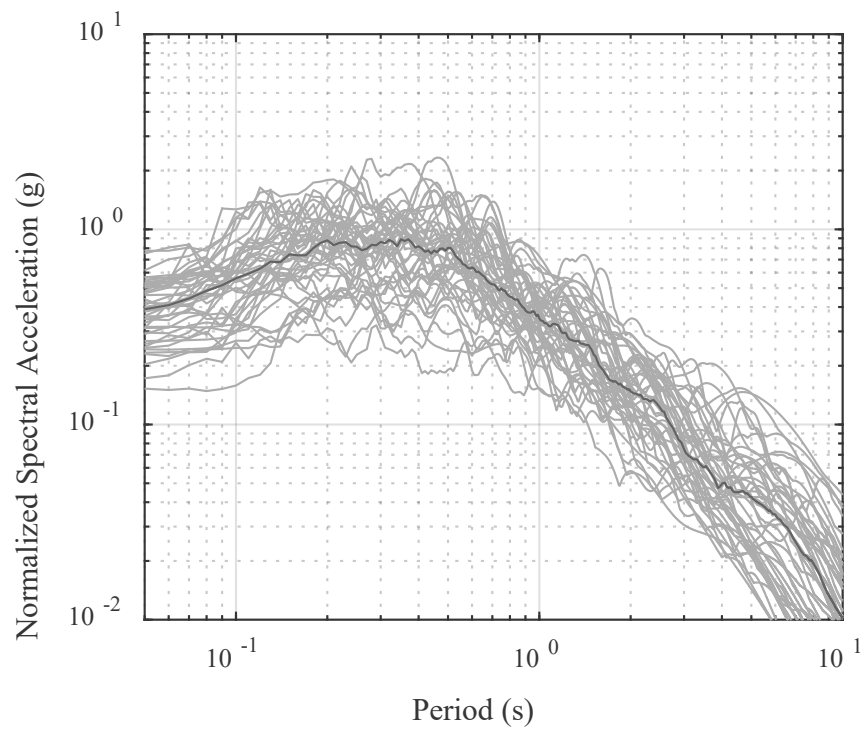


Figure 69. Normalized ground motion response spectra.